



Universiteit
Leiden

The Netherlands

Superfluid helium-3 in cylindrical restricted geometries : a study with low-frequency NMR

Benningshof, O.W.B.

Citation

Benningshof, O. W. B. (2011, March 30). *Superfluid helium-3 in cylindrical restricted geometries : a study with low-frequency NMR*. Retrieved from <https://hdl.handle.net/1887/16677>

Version: Corrected Publisher's Version

License: [Licence agreement concerning inclusion of doctoral thesis in the Institutional Repository of the University of Leiden](#)

Downloaded from: <https://hdl.handle.net/1887/16677>

Note: To cite this publication please use the final published version (if applicable).

Superfluid Helium-3 in Cylindrical Restricted Geometries

A Study with Low-Frequency NMR

PROEFSCHRIFT

ter verkrijging van
de graad van doctor aan de Universiteit Leiden,
op gezag van rector magnificus prof. mr. P.F. van der Heijden,
volgens besluit van het College voor Promoties
te verdedigen op woensdag 30 maart 2011
klokke 15:00 uur

door

Olaf Willem Boudewijn Benningshof

geboren te Capelle aan den IJssel
in 1979

Promotiecommissie:

Promotor:	Prof. dr. G. Frossati	Universiteit Leiden
Co-promotor:	Dr. R. Jochemsen	Universiteit Leiden
Leden:	Prof. dr. J. van den Brink	IFW Dresden
	Dr. H.B. Brom	Universiteit Leiden
	Prof. dr. P.H. Kes	Universiteit Leiden
	Prof. dr. J.M. van Ruitenbeek	Universiteit Leiden
	Prof. dr. A.T.A.M. de Waele	Technische Universiteit Eindhoven

Dit werk is uitgevoerd binnen de onderzoeksgroep Quantum Physics and Applications at Low Temperatures (QPALT) van het Leids Instituut voor Onderzoek in de Natuurkunde (LION). Dit instituut is een onderdeel van de Faculteit voor Wiskunde en Natuurwetenschappen van de Universiteit Leiden. Het onderzoek maakt deel uit van het onderzoeksprogramma van de Stichting voor Fundamenteel Onderzoek der Materie (FOM), die financieel wordt gesteund door de Nederlandse Organisatie voor Wetenschappelijk Onderzoek (NWO).

Cover: The pictures on the cover show the homebuilt cell and magnet used for the experiments described in this thesis.

Contents

Overview	vii
1 Theory	1
1.1 Normal Fermi liquid	1
1.2 Superfluidity in bulk helium-3	2
1.3 Ginzburg-Landau theory	4
1.4 Free energy density of the superfluid phases	5
1.5 B-phase	8
1.6 B ₂ -phase	8
1.7 Dipole energy	9
1.8 Coherence lengths	12
1.8.1 Coherence lengths of different interactions	12
2 Cell and read-out	15
2.1 Introduction	15
2.2 Cell	15
2.3 Overview of used NMR techniques at helium-3 superfluids	19
2.4 Read-out system	22
2.4.1 The decoupling capacitor	24
2.4.2 Measuring over the parasitic capacitance	25
2.4.3 Mutual inductance	28
2.4.4 Copper wiring to room temperature	31
2.4.5 Considerations	33
2.5 Experimental Magnet	33
2.6 Tank Coil	38
2.6.1 Pick-up Coil	40
2.7 Baseline and Feedback system	41
2.8 Noise	48
2.9 Conclusion	51

3	Spin waves in cylinder of 1 mm in diameter	53
3.1	Spin waves	53
3.2	Transverse NMR in $^3\text{He-B}$	56
3.3	Orientation of the \hat{n} -vector due to bulk and surface effects	58
3.4	Orientation of the \hat{n} -vector in cylindrical samples	61
3.5	Spin dynamics in a non-uniform texture	65
3.5.1	Cylindrical geometry	66
3.6	The magnetic healing length of $^3\text{He-B}$	67
3.7	NMR absorption in cylinder of 1 mm diameter	67
3.8	Metastable texture	71
3.9	Textural transition	77
3.10	Discussion	80
3.11	Conclusion	81
4	Helium-3 in nanosized cylinders	83
4.1	Introduction	83
4.2	Polar state	84
4.2.1	Polar state in cylinders	85
4.3	Photonic crystal fibers	90
4.3.1	Roughness	95
4.4	Expected NMR 'fingerprint' in narrow cylinders	104
4.4.1	A-phase	104
4.4.2	Polar-phase	105
4.4.3	Axial state	106
4.4.4	B-phase	108
4.5	NMR results of the channels	110
4.5.1	Normal state	110
4.5.2	Channels cooled down to the lowest temperatures	110
4.5.3	Discussion	116
4.5.4	NMR shifts influenced by the adsorbed helium-3 at the wall	119
4.6	Conclusion	128
5	Cold valve	131
5.1	A high performance normally-closed solenoid-actuated cold valve	131
5.2	Description of the design	131
5.3	Operating principles	133
5.3.1	Actuation	133
5.3.2	Closure: Seat and Ruby	134
5.3.3	Teflon spacer	134
5.3.4	Thermal contact	136
5.4	Valve performance	136

A Appendix	139
A.1 Pressure dependent quantities and constants of helium-3	139
A.2 Gap function	140
A.3 Susceptibility of the B-phase of helium-3	141
A.4 Transmission Line	143
Bibliography	147
Samenvatting	155
Curriculum vitae	159
Publicatielijst	161
Dankwoord	163

CONTENTS

Overview

A fascinating effect in liquid helium-3 is that two atoms can form a Cooper pair, which (as this happens for a macroscopic fraction) changes the liquid into a superfluid. This is in analogy with superconductivity, where the Cooper pairs are formed by two electrons. In case of type I superconductors there exists only one 'kind' of superconductivity, which is a consequence of the fact that only one symmetry (gauge symmetry) can break and is broken. The total symmetry in liquid helium-3 is much richer, and can be broken in many different ways, which all correspond to a *different* superfluid order parameter. The superfluids distinguish themselves by their difference in the (relative) orientation of the orbital and spin angular momentum.

In bulk helium-3 without magnetic field there exist two different superfluid phases, namely the A- and B-phase. If one includes a magnetic field, which induces a preferred orientation for the spin angular momentum (additional symmetry breaking), three more phases are found. An alternative way to influence the orientation in the superfluid is obtained by changing from bulk to restricted geometries. The walls of the container will locally change the preferred orientation of the orbital angular momentum. If the dimension of the container is reduced to the size of the Cooper pairs (coherence length), the existence of a superfluid is suppressed in that direction, coinciding with additional symmetry breaking for which a new superfluid phase can be expected.

This thesis concerns the symmetry, phase, and order parameter of the superfluid in restricted geometries in combination with a magnetic field. Two cylindrical containers are constructed, for which the axis is aligned with the magnetic field. The first cell has a diameter (540 nm) of only a few times the size of the Cooper pairs, designed to find a new superfluid phase, namely the polar phase. The second container has a diameter of 1 mm, which is the ideal size to create a potential (in the B-phase) for spin waves.

To probe any superfluid phase or spin waves, we used Nuclear Magnetic Resonance (NMR) techniques. As the superfluids have an anisotropic susceptibility, it is an excellent tool to distinguish the different phases. However, as our samples are relatively small in volume, and the experiment needs to be performed in low magnetic field to prevent additional symmetry breaking, a very sensitive read-out magnetic resonance detection system needed to be developed.

Outline of thesis

Chapter 1 gives a general introduction of the properties of liquid helium-3 and superfluidity. In particular the properties of the superfluid B-phase (and B₂-phase: the B-phase in magnetic field) are considered. Here their preferred orientations are described including the corresponding bending lengths. This background is necessary to understand, explain and fit the experimentally obtained data, presented in chapter 3 and 4.

Chapter 2 This chapter describes the experimental cell and the detection set-up. The experimental cell was carefully designed to perform experiments in both the 1 mm container and the 540 nm channels, simultaneously. This cell was positioned in a solenoid magnet, which acts as the static magnetic field for the NMR. Important for helium-3 experiments is to have a very homogenous magnetic field, so within our boundary conditions (available space) we designed and produced a magnet with a magnetic field as homogeneous as possible.

As the experiments are performed at low magnetic field and the total amount of helium-3 atoms is very small (less than one μmole), we needed to build a very sensitive probe (read-out system). This was accomplished by creating an LC-circuit which maintains an ultra-high quality factor as it is combined with a weakly coupled transformer, of which the results and simulations are described in detail in this chapter. Also the description and simulations of the feedback loop can be found here, which was necessary to ensure that the system was performing at highest sensitivity at all times.

Chapter 3 Here the experiments are described, which are performed in the cylindrical container of 1 mm in diameter. Characteristic for this dimension is that the preferred orientation in the B-phase will be locally varying, resulting in a curved configuration into the cell. Exclusive in our case, as it is performed at low pressures and low magnetic fields, we could make a texture (a certain configuration in which the preferred orientation of the superfluid is bent over the sample), which was metastable and unchanged for the whole pressure and temperature ranges. As this texture can be considered as a potential to sustain spin waves, we had the unique opportunity to study them for several pressures in (nearly) the same texture. A positive effect is that this potential (texture) is close to a quadratic one, creating a two-dimensional system, in which the intensities of all spin wave modes should be equal. This provides us with the perfect condition to observe the increase of the number of spin wave modes growing in our cell by increasing the pressure.

Finally we were able to make a textural transition to the expected (on energetic arguments) texture, from which we conclude that the metastable texture could be realized if the growing speed is sufficiently slow.

Chapter 4 This chapter concentrates on the measurements performed with a NMR coil around a bundle of photonic crystal fibers. These fibers contain channels, which

are very cylindrical and have an average diameter of 540 nm. Initially the possible superfluid phases in such geometry are described. Also the behavior (frequency shifts) in the NMR spectrum for these expected phases is considered.

As the roughness of the wall of such a channel will determine the boundary conditions for the superfluid, and thus the stability of the expected phases, we performed roughness measurements on the inside of the 540 nm channels. Special techniques were invented to open the fiber in the axial direction, for which we believe to have the scoop to perform atomic force microscopy AFM in the inside of such channels.

In the rest of this chapter the NMR experiments performed at the bundle are discussed. The first part is about the obtained NMR signals from liquid helium-3 inside these channels. However, from the results it cannot be excluded if any superfluid state is formed inside these channels. The difficulty is that, by the lack of the observation of the (distorted) B-phase, a natural fixed point is missing. While certain minimum values (for this particular geometry) could be determined, this part ends with the discussion on how the configuration of the cell should be changed in order to be able to measure any of the expected phases, especially the polar phase.

The second part describes the extra absorption lines in the NMR spectrum. Interesting is that in these geometries the total magnetization of the solid (adsorbed helium-3 at the wall) and the liquid are comparable, resulting in an influence of the NMR resonance lines on each other. A model, normally used to deal with these effects in highly porous samples (e.g. aerogel), is used to explain the NMR shifts concerning our volumes. This model, constructed in the limit that there is a rapid exchange between the helium-3 atoms of the solid and liquid, worked well in porous samples and explained the observation of only one NMR peak.

Chapter 5 Finally a high performance normally-closed solenoid-actuated cold valve is presented. This is an electromagnetically driven normally-closed valve for liquid helium, which is meant to regulate the input flow to a 1K pot. Here a new feature is presented which prevents seat deformation at room temperature and provides comfort and durability for intensive use.

One additional remark concerning the system of units is in order. The expressions in this thesis are formulated in the international system (SI) or centimeter-gram-second (CGS) unit system. As we in principle would prefer to express everything in SI units, there are some reasons to express the equations into the CGS system. First of all some equations are clearer with CGS units. Secondly, and more important is that the most influential papers in this field are all expressed in CGS units. Consequently, (modern) literature about this topic is also mainly expressed in the CGS system. As a form of respect, and not to get confused with the usual expressions in literature, we have expressed a great deal of the equations in the CGS system as well. In practice, concerning this thesis, it often involves only a difference by the factor $\mu_0/4\pi$ (or the square root of it), where μ_0 is the permeability of vacuum.

Chapter 1

Theory

1.1 Normal Fermi liquid

The ${}^3\text{He}$ nuclei consist of two protons and one neutron, and has a total spin $\mathbf{S} = 1/2$. Half quantum numbers makes the particle a fermion, and an ensemble of spin $1/2$ particles should (for low enough temperatures) behave as formulated by the Fermi-Dirac statistics. At atmospheric pressure, ${}^3\text{He}$ becomes liquid at a temperature of 3.2 K, which is relatively close to the Fermi temperature T_F (~ 1 K). It is for this reason that at the moment ${}^3\text{He}$ is liquefied, it lets itself be described by the Fermi Liquid Theory FLT. This section will not derive any of the quantum properties of a Fermi system, for which there are good text books [1], [2], [3]. Here only the relevant FLT relations for this thesis are summarized.

In the ground state of a Fermi system the energy fills up till the Fermi energy ε_F . The energies can be expressed in k -space, where ε_F corresponds to the Fermi wave vector k_F . Concerning N particles in a cubic box one can solve the Schrödinger equation for the ground state, from here the relation k_F is obtained as:

$$k_F = \sqrt[3]{3\pi^2 n}, \quad (1.1)$$

where n is the particle density per unit volume.

The ${}^3\text{He}$ atoms/particles have, because of its extensiveness, hard core repulsion between each other. One can say: It creates a kind of 'screening cloud' for the other atoms. To include this interaction the mass m of the ${}^3\text{He}$ atoms should be replaced by an effective mass m^* . This changes the ${}^3\text{He}$ particles into 'quasi-particles', which is still described with the FLT, but with an effective mass m^* . The ratio between the effective mass m^* and the mass m is given by:

$$\frac{m^*}{m} = 1 + \frac{1}{3}F_1^s, \quad (1.2)$$

where F_1^s is a Landau parameter, which is pressure dependent and listed in the appendix A.1.

The Fermi energy for (quasi)-particles is expressed as,

$$\varepsilon_F = \frac{\hbar^2 k_F^2}{2m^*} = \frac{p_F^2}{2m^*} = \frac{m^* v_F^2}{2} = k_B T_F, \quad (1.3)$$

where $p_F = \hbar k_F$ is the Fermi momentum, $v_F = p_F/m^*$ the Fermi velocity and T_F the Fermi temperature.

The density of states for both spin components per unit volume per unit energy is given by:

$$N_F = 2N(0) = \frac{m^* k_F}{\pi^2 \hbar^2} = \frac{p_F^2}{\pi^2 \hbar^3 v_F} = \frac{3n}{p_F v_F} = \frac{3nm^*}{p_F^2}, \quad (1.4)$$

where $N(0)$ is the density of states for one spin component at the Fermi energy.

As shown empirically by experiments, see for example [4], the spin susceptibility χ of ^3He is hardly dependent on temperature when $T \ll T_F$. The Pauli paramagnetic spin susceptibility for normal liquid ^3He is then

$$\chi_N = \chi_N^0 / (1 + F_0^a), \quad (1.5)$$

where F_0^a is a Landau parameter, see appendix A.1, and χ_N^0 the Pauli spin susceptibility for (quasi)-particles with an effective mass m^* .

$$\chi_N^0 = \mu_0^2 N_F = \frac{1}{4} \gamma^2 \hbar^2 N_F, \quad (1.6)$$

where μ_0 is the magnetic moment and γ the gyromagnetic ratio of the ^3He nucleus. The gyromagnetic ratio γ for ^3He is $-20.3801587 \cdot 10^7$ rad Hz T $^{-1}$.

1.2 Superfluidity in bulk helium-3

The first understanding of pair correlations in an interacting Fermi system was described by Bardeen, Cooper and Schrieffer [6]. They constructed a microscopic theory, which could explain the phenomena of superconductivity. As liquid ^3He is a Fermi system, one can expect the same phenomena. However, the ratio between the critical temperature T_c compared to the Fermi temperature T_F is typically $T_c/T_F \sim 10^{-3}$. While the T_F of electrons is rather high, about 10.000 K, for ^3He it is approximately 1 K. The low T_c (~ 1 mK) could only be reached after the invention of dilution fridges including a nuclear stage or Pomeranchuk cell. It is due to this technical difficulty that there is more than 60 years difference between the first observations of superconductivity in 1911 by Kamerling Onnes [7] and the superfluidity in liquid ^3He by Osheroff, Richardson and Lee [8].

Superfluidity itself was already discovered in 1930 for the isotope ^4He [9], however here the phenomena is based on a different principle. For ^4He , which is a boson, the fluid condenses into a Bose-Einstein condensate. While a lot of the phenomena are the same, the superfluid phase diagram of ^3He is much richer. In both, superconductivity

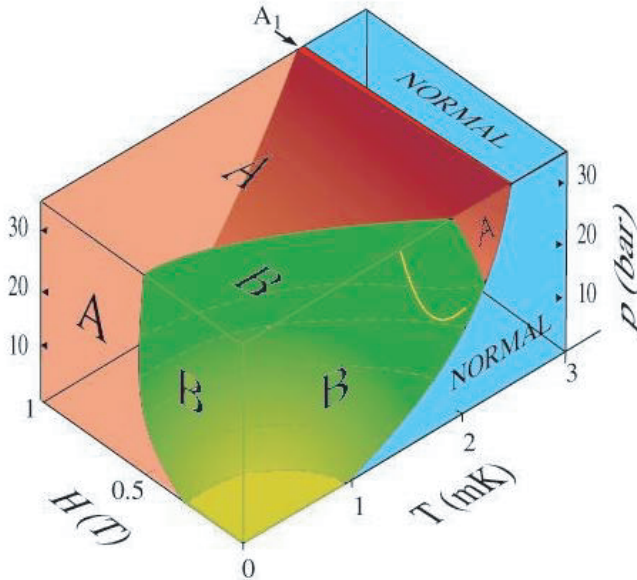


Figure 1.1: Phase diagram of bulk liquid ^3He , as function of temperature, pressure and magnetic field. The bulk shows the normal liquid helium-3 phase and 5 different superfluid phases. Figure is taken from [5].

in type I superconductors and superfluidity in ^4He , there exist 'one kind' of superconductivity/superfluidity, while in ^3He there exist 'more kinds' of superfluidity. The difference is due to higher symmetry in the liquid, which will be discussed in more detail in the next sessions.

The variety of superfluid phases can already be seen in the bulk properties of ^3He , see phase diagram in figure 1.1. In zero magnetic field two stable phases exist, named the A- and B-phase. They were observed for the first time in 1971¹, when accurate measurements at the melting curve of ^3He were done. In magnetic field a third phase was discovered, the A₁-phase. Future studies pointed out that the A- and B-phases do break symmetry when they are put in a magnetic field and are in fact different phases. These phases are referred as the A₂- and B₂-phase. The richness of different phases performs themselves already in the bulk properties (including magnetic fields) of ^3He . Even more phases are predicted as one changes the geometric dimensionality of the system.

All phases let themselves describe by a different order parameter. The difference in isotropic (or better anisotropic) properties results in a preferable orientation of

¹Initially it was thought that it was a transition in the solid [10].

the order parameter. A powerful technique to distinguish the different phases (order parameter) is with the help of nuclear magnetic resonance NMR. The line shape of the NMR spectrum gives good identification ('fingerprint') of each phase. The applied NMR techniques to obtain the data of this thesis and predicted NMR spectra of certain phases can be found in the chapters 3 and 4, respectively.

1.3 Ginzburg-Landau theory

In order to investigate the possibility of a possible new superfluid phase of liquid ^3He in restricted geometry (Dimensions), we discuss shortly the Ginzburg-Landau theory. Landau's theory of second order phase transitions was together with Ginzburg [11] extended to be able to describe the phenomena of superconductors and superfluids. It is a macroscopic theory, in which the order parameter of the superconductor is described with a wave function ψ . The order parameter has spatial properties and is complex. The free energy density difference between the normal state F_n (ground state of a Fermi system) and the superfluid state F_s is expanded into a power series of the order parameter. In the case we neglect the spatial variation (homogenous or bulk case) of the order parameter, we can write the free energy density as:

$$F_n - F_s = \alpha\psi^2 + \frac{\beta}{2}\psi^4. \quad (1.7)$$

The most simple temperature dependence for this model is when $\alpha(T) = -\alpha_0(1 - T/T_c)$ and β is constant, which is a good description for temperatures near the transition temperature T_c . Here the coefficients have the correct limits, and minimizing the free energy with respect to the order parameter gives:

$$\psi = \pm \sqrt{\frac{\alpha_0}{\beta}} \sqrt{1 - T/T_c}. \quad (1.8)$$

At zero temperature, the free energy density is maximally lowered. No more Cooper pairs can then be formed. The average gap energy $^2 \Delta(T)$ is then maximal and the free energy density, or total condensation energy, can be simplified as:

$$F_n - F_s = \frac{1}{2}N(0)\Delta(0)^2. \quad (1.9)$$

(Here $N(0)$ is the density of states for one spin component.) The product of $1/2 N(0)\Delta(0)$ corresponds with the total amount of formed Cooper pairs and every Cooper pair lowers the free energy density with $\Delta(0)$.

If one wants to include the variation of the order parameter $\psi(\mathbf{r})$, a gradient term (or kinetic energy term) in the free energy density should be included.

²The average gap energy $\Delta(T)$ corresponds with ψ , but is the more general form for the order parameter. Strictly spoken ψ of equation (1.8), only valid near T_c , may not be extrapolated to zero temperature. To express the maximum condensation energy, equation (1.9), one should express it in terms of the average gap energy.

$$F_n - F_s = \alpha |\psi(\mathbf{r})|^2 + \frac{\beta}{2} |\psi(\mathbf{r})|^4 + k |\nabla \psi(\mathbf{r})|^2, \quad (1.10)$$

where k is determined by the normalization of $\psi(\mathbf{r})$. The gradient term prevents $\psi(\mathbf{r})$ to change 'quickly', which 'costs' too much energy. Instead it smoothes the order parameter over a typical size ξ , which we call the coherence length. Coherence lengths are temperature dependent. In the case of superconductors they have the form of $\xi(T) = (k/\alpha)^{1/2}$, which is proportional with $(1 - T/T_c)^{-1/2}$ near T_c .

1.4 Free energy density of the superfluid phases

The Landau-Ginzburg theory, as described in the previous section, explains phenomenologically the behavior of superconductors near the transition. A Cooper pair formed by 2 electrons, which is an s -wave pair, is a relative simple system. Here both, the angular momentum \mathbf{L} and spin quantum number \mathbf{S} of the Cooper pairs are 0. In such systems only one symmetry is and can be broken, namely the Gauge symmetry $U(1)_\phi$. Consequently there can only exist one kind of superconducting state. As shown in the previous section, it is described by a complex order parameter $\psi(\mathbf{r}) = \psi_0(\mathbf{r})e^{i\phi}$, where ψ_0 is the amplitude and ϕ the phase.

Like an electron, ^3He is a spin 1/2 particle. The most important difference is not the weight (the atom is ~ 5500 times heavier than the electron) but its spatial extensiveness. The hard core repulsion between the atoms prevents the wave functions to overlap. As a consequence the Cooper pairs prefer to form in p -wave pairs, instead of s -wave pairs. For p -waves pairing the angular moment and spin quantum number changes to $\mathbf{L} = \mathbf{S} = 1$. Such pairing systems have much more symmetry, next to the Gauge symmetry it has three dimensional rotation symmetry for both the orbital and spin space. The total symmetry G is given by a product of the three independent symmetries.

$$G = SO(3)_\mathbf{L} \times SO(3)_\mathbf{S} \times U(1)_\phi. \quad (1.11)$$

The total symmetry can at least be broken in 13 different continuous subgroups, and 4 discrete subgroups. All subgroups have a different order parameter structure [12], [13], [14], [15], [16]. An illustration of the broken $SO(3)_\mathbf{L} \times SO(3)_\mathbf{S} \times U(1)_\phi$ into continuous subgroups is shown in figure 1.2, which is taken from Bruder and Vollhardt [16].

All subgroups correspond to minima, local minima, stationary points or at worst saddle points in the free energy density given by a Landau type of expression. The order parameter is now a complex 3×3 matrix, and equation (1.7) should be upgraded for such order parameters. Obeying the restrictions of invariance under spin and spatial rotations (and Gauge invariance) the free energy density for the homogeneous case, including strong coupling corrections, till fourth order is given by Mermin and Stare [12], [17] as

$$F_n - F_s = \alpha \operatorname{tr}(\mathbf{A}\mathbf{A}^\dagger) + \beta_1 |\operatorname{tr}\mathbf{A}\tilde{\mathbf{A}}|^2 + \beta_2 [\operatorname{tr}(\mathbf{A}\mathbf{A}^\dagger)]^2 + \beta_3 \operatorname{tr}[(\mathbf{A}^\dagger\mathbf{A})(\mathbf{A}^\dagger\mathbf{A})^*] + \beta_4 \operatorname{tr}[(\mathbf{A}\mathbf{A}^\dagger)^2] + \beta_5 \operatorname{tr}[(\mathbf{A}\mathbf{A}^\dagger)(\mathbf{A}\mathbf{A}^\dagger)^*], \quad (1.12)$$

where the 3×3 matrix \mathbf{A} is related to the spin space matrix $\Delta_{\mu\nu}$. The coefficients in the limit of the BCS weak-coupling approach are given by:

$$\alpha = -\frac{N(0)}{3} \left(1 - \frac{T}{T_c}\right) \quad (1.13)$$

$$\beta_i = \tilde{\beta}_i \beta_{BCS} = \tilde{\beta}_i \frac{7\zeta(3)}{240\pi^2} N(0) \left(\frac{1}{k_B T_c}\right)^2 \quad (1.14)$$

where $\tilde{\beta}_i = (-1, 2, 2, 2, -2)$. Strong coupling effects are included as $\Delta\beta_i$ in β_i .

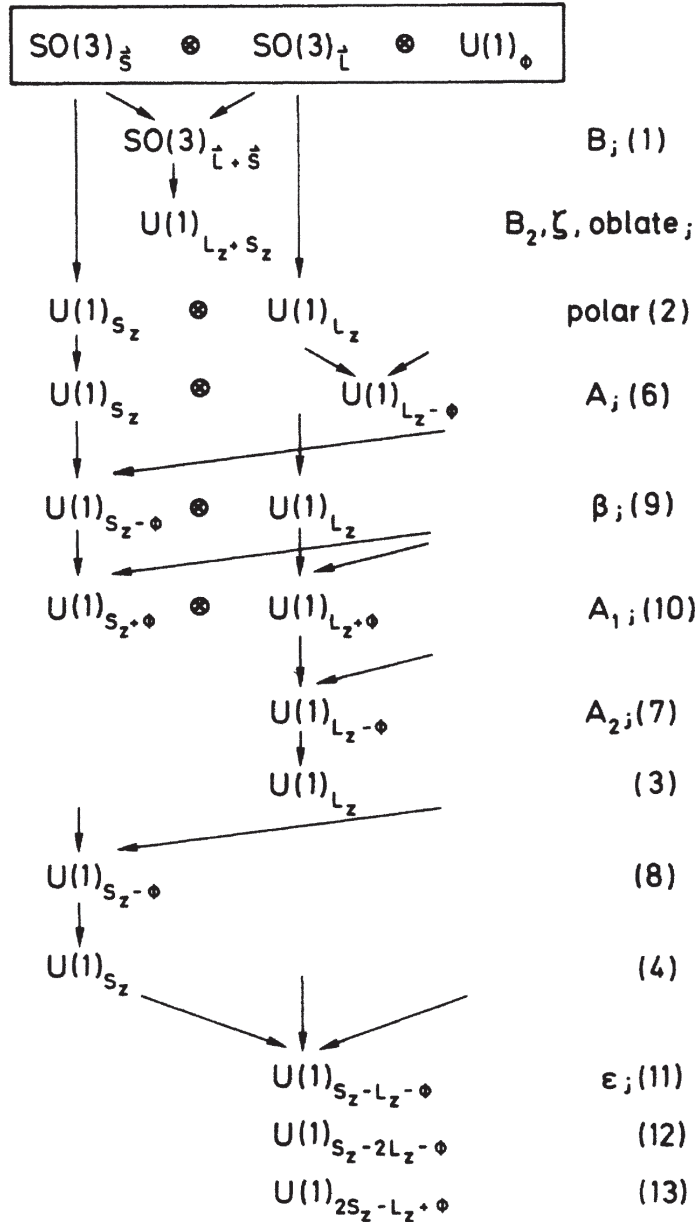


Figure 1.2: Scheme of $SO(3)_L \times SO(3)_S \times U(1)_\phi$ broken into continuous subgroups. Broken relative symmetries arise in factorizations involving more than one group, indicated by diagonal arrows. On the right name of phase (if any) is mentioned.

1.5 B-phase

Most experiments on the superfluid ^3He in this thesis are done in the B-phase of ^3He . This phase was for the first time described by Balian and Werthamer [18], and was called the BW-state. It is the lowest energy state of the free energy density (1.12), which corresponds with Mermin and Stare [12] when they investigate different gap structures in the weak coupling BCS theory. The gap structure, like in the case of type I superconductors, is isotropic (see figure 1.3). Here no preferred directions are demanded in spin-space.

In the B-phase the symmetry of the rotation in spin- and orbital space are broken, but not independently. The relative orientation is still ordered, and has still rotational invariance ($SO(3)_{\mathbf{L}+\mathbf{S}}$). This relative rotation lets itself be described with a rotation matrix \mathbf{R} characterized by $\hat{\mathbf{n}}$ and θ . The rotation axis $\hat{\mathbf{n}}$ is perpendicular to the plane formed by the \mathbf{L} and \mathbf{S} vectors of the Cooper pairs and θ is the angle between those two vectors.

The order parameter matrix of equation (1.12), for the B-phase, can be written as:

$$A_{\mu j} = 3^{-1/2} e^{i\phi} R_{\mu j}(\hat{\mathbf{n}}, \theta) \quad (1.15)$$

$$R_{\mu j} = (1 - \cos \theta) \hat{n}_\mu \hat{n}_j + \cos \theta \delta_{\mu j} - \sin \theta \sum_k \epsilon_{\mu j k} \hat{n}_k \quad (1.16)$$

where ϕ is the overall phase variable.

It should also be emphasized that the B-phase, contains all the triplet components for both the spin and the orbital angular momentum pairing, hence $\mathbf{S} = \mathbf{L} = 1$. Concerning spin-space, it is convenient to combine the three spin components into the order parameter vector of spin-space $\mathbf{d}(\mathbf{k})$. The energy gap matrix of spin space $\Delta_{\mathbf{k}\alpha\beta}$ expanded in Pauli matrices is then

$$\Delta_{\mathbf{k}\alpha\beta} = \sum_{\mu} d_{\mu}(\mathbf{k}) (\sigma_{\mu} i \sigma_2)_{\alpha\beta} = \begin{bmatrix} -d_1 + id_2 & d_3 \\ d_3 & d_1 + id_2 \end{bmatrix} = \begin{bmatrix} \Delta_{\uparrow\uparrow} & \Delta_{\uparrow\downarrow} \\ \Delta_{\downarrow\uparrow} & \Delta_{\downarrow\downarrow} \end{bmatrix}. \quad (1.17)$$

The energy gap in k -space is shown in figure 1.3. At the equator the gap is formed by combination of up-up and down-down spin pairs, while at the poles it is formed by combination of up-down and down-up spin pairs. The anisotropy of the spin pairs in the k -space mentions the B-phase also as 'pseudo'-isotropic.

1.6 B₂-phase

In the ^3He -B phase the gap parameter is isotropic, for which it can be referred to as the spherical state. If an external magnetic field is applied to the B-phase, the gap parameter becomes anisotropic. The gap in the z -direction (direction of magnetic field) is flattened, and one may speak of the squashed spherical state. This is a

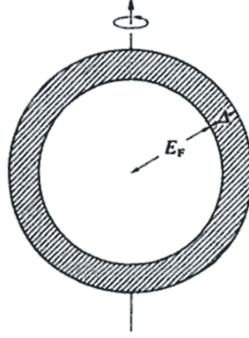


Figure 1.3: Scheme of the energy gap, indicated by the shaded area, of the B-phase in k -space. Ratio of Fermi energy E_F and the gap Δ is not to scale. Figure is taken from [19].

consequence of the fact that the Cooper pairs formed in a magnetic field prefer $|\uparrow\uparrow\rangle$ and $|\downarrow\downarrow\rangle$ spins pairs instead of $|\uparrow\downarrow\rangle$ spin pairs. Here the $SO(3)_{\mathbf{L}+\mathbf{S}}$ symmetry gets broken. The symmetry, which is conserved, is the rotation around the z -axis, hence $U(1)_{L_z+S_z}$. The phase corresponding with this symmetry is the B₂-phase, which was first described by Barton and Moore [13]. The order parameter matrix is given by:

$$A_{\mu j} = p_2 e^{i\phi} \begin{bmatrix} A & B & 0 \\ \pm B & \mp A & 0 \\ 0 & 0 & C \end{bmatrix} \quad (1.18)$$

where,

$$\begin{aligned} p_2 &= [2(|A|^2 + |B|^2) + |C|^2]^{-1/2} \\ A &= \frac{1}{2}(\Delta_{\uparrow\uparrow} + \Delta_{\downarrow\downarrow}) \\ B &= -\frac{1}{2}i(\Delta_{\uparrow\uparrow} - \Delta_{\downarrow\downarrow}) \\ C &= \Delta_{\uparrow\downarrow}. \end{aligned}$$

1.7 Dipole energy

The dipole interaction, coupling of the nuclear spins of the ^3He atoms, has influence on the relative orientation of \mathbf{L} and \mathbf{S} . However, this energy is so small that the influence on the forming of the order parameter itself can be neglected. Nevertheless, it is the most important orientation force in the superfluid, which cannot be 'turned off'³.

³in contrast with magnetic fields and surfaces.

The standard expression for magnetic-dipole interaction is

$$H_D = \frac{1}{2}(\gamma\hbar)^2 \int d^3\mathbf{r} \int d^3\mathbf{r}' \left\{ \frac{\boldsymbol{\sigma}(\mathbf{r}) \cdot \boldsymbol{\sigma}(\mathbf{r}')}{|\mathbf{r} - \mathbf{r}'|^3} - 3 \frac{[(\mathbf{r} - \mathbf{r}') \cdot \boldsymbol{\sigma}(\mathbf{r})][(\mathbf{r} - \mathbf{r}') \cdot \boldsymbol{\sigma}(\mathbf{r}')] }{|\mathbf{r} - \mathbf{r}'|^5} \right\}. \quad (1.19)$$

Where $\boldsymbol{\sigma}(\mathbf{r})$ is the spin density operator. This Hamiltonian is solved for a p -wave condensate by tremendous work of Leggett [20], [21], [22]. By expressing the dipole energy density F_D in terms of the order parameter matrix, one obtains

$$F_D = \frac{3}{5}g_D(T) \sum_{ij} [A_{ii}^* A_{jj} + A_{ij}^* A_{ji} - \frac{2}{3} A_{ij}^* A_{ij}], \quad (1.20)$$

where $g_D(T)$ is the dipole coupling constant

$$g_D(T) \approx \frac{1}{2}\pi\gamma^2\hbar^2 \langle R^2 \rangle_{av} \left[\frac{1}{2}N_F\Delta(T) \ln \left(\frac{2\varepsilon_c}{\Delta(0)} \right) \right]^2. \quad (1.21)$$

The renormalization factor $\langle R^2 \rangle_{av}$ is there because it is not entirely obvious that the expression of equation (1.19) is the same for quasi-particles, as discussed by Leggett and Takagi [22] [23]. However, experimentally it is shown that it should be very close to 1 (in fact it might be 1), which is the reason we put it to 1 for the rest of this thesis. The logarithm includes the cut off energy ε_c , which is proportional with the pair interaction potential:

$$\ln \left(\frac{2\varepsilon_c}{\Delta(0)} \right) \sim \frac{1}{N(0)V_1}. \quad (1.22)$$

The product $N(0)V_1$ can be obtained by fitting the experimentally found T_c , and is proportional with $\ln(T_c/T_F)$ [24]. So, the cut off energy ε_c is hardly pressure dependent and is roughly $\sim 0.7k_B$ [25]. Due to the logarithm, small deviations in ε_c have little or no consequence and, for this reason, it is kept fixed for all pressures.

If the B-phase order parameter matrix (1.15) is substituted in de dipole free energy density (1.20) we obtain:

$$F_D^B = \frac{8}{5}g_D(T) \left(\cos\theta + \frac{1}{4} \right)^2 + const. \quad (1.23)$$

The angle $\theta = \theta_L = \cos^{-1}(-1/4) \approx 104^\circ$ minimizes the dipole energy (and of course $\theta = 2\pi - \theta_L$). The L refers to Leggett and the angle θ_L is in the literature known as the Leggett angle. Consequently the angle between \mathbf{L} and \mathbf{S} in the B-phase will be θ_L . The $\hat{\mathbf{n}}$ -vector does not have a preferred orientation in the bulk B-phase, so it does not contribute to lower the dipole energy.

In the case of the B₂-phase the $\hat{\mathbf{n}}$ -vector does have a preferred orientation, which influences the total dipole energy. Putting the B₂-phase order parameter matrix (1.18) in equation (1.20) we obtain:

$$F_D^{B_2} = \frac{1}{5} \lambda_D N_F \left\{ f_0(\theta) + f_1(\theta)(\hat{\mathbf{n}} \cdot \hat{\mathbf{H}})^2 + f_2(\theta)(\hat{\mathbf{n}} \cdot \hat{\mathbf{H}})^4 \right\} + const, \quad (1.24)$$

where

$$\lambda_D N_F \equiv g_D(T)/\Delta(T)^2, \quad (1.25)$$

and

$$\begin{aligned} f_0(\theta) &= 8\Delta_{\perp}^2(\cos\theta + 1/4)^2 + 8(\Delta_{\parallel} - \Delta_{\perp})\Delta_{\perp}\cos\theta(\cos\theta + 1/4) \\ &\quad + 2(\Delta_{\parallel} - \Delta_{\perp})^2\cos^2\theta, \\ f_1(\theta) &= 2(\Delta_{\parallel} - \Delta_{\perp})[\Delta_{\perp}(3 + \cos\theta - 4\cos^2\theta) \\ &\quad + 2(\Delta_{\parallel} - \Delta_{\perp})\cos\theta(1 - \cos\theta)], \\ f_2(\theta) &= 2(\Delta_{\parallel} - \Delta_{\perp})^2(1 - \cos\theta)^2. \end{aligned} \quad (1.26)$$

Here the relations $\Delta_{\uparrow\uparrow} = \Delta_{\downarrow\downarrow} = \Delta_{\perp}$ and $\Delta_{\uparrow\downarrow} = \Delta_{\downarrow\uparrow} = \Delta_{\parallel}$ are used.

Equation (1.24) is minimal in energy, if the $\hat{\mathbf{n}}$ -vector and the magnetic field \mathbf{H} are parallel. This is true for all configurations of Δ_{\perp} and Δ_{\parallel} and at the minimum equation (1.24) becomes:

$$F_D^{B_2} = \frac{8}{5} \lambda_D N_F \left(\cos\theta + \frac{1}{4} \frac{\Delta_{\parallel}}{\Delta_{\perp}} \right)^2 + const., \quad \hat{\mathbf{n}} = \pm \hat{\mathbf{H}}. \quad (1.27)$$

Thus the total dipole energy is now minimized if the angle between \mathbf{L} and \mathbf{S} is [26], [27], [28]

$$\theta_0(H) = \cos^{-1} \left(-\frac{1}{4} \frac{\Delta_{\parallel}}{\Delta_{\perp}} \right). \quad (1.28)$$

The angle, now depending on the ratio of $\Delta_{\parallel}/\Delta_{\perp}$, varies between θ_L (if populations are the same, as in the case of the B-phase) and 90° (Δ_{\parallel} is unoccupied).

Magnetic fields change the population ratio, but also influence the orientation of the $\hat{\mathbf{n}}$ -vector. From equation (1.24) we can determine the orientation energy density due to magnetic field. The magnitude given to second order:

$$\Delta f_H^{B_2} = \lambda_D N_F \frac{(\Delta_{\parallel} - \Delta_{\perp})\Delta_{\perp}}{H^2} (\hat{\mathbf{n}} \cdot \mathbf{H})^2, \quad (1.29)$$

where [19]

$$(\Delta_{\perp} - \Delta_{\parallel})\Delta_{\perp} = \frac{5}{12} \left(\frac{\gamma \hbar H}{1 + F_0^a} \right)^2 \frac{\beta_{345}^{WC} T}{\beta_{345} T_c}. \quad (1.30)$$

Two points should be emphasized which are relevant for the experiments presented in this thesis. First the orientation energy density $\Delta f_H^{B_2}$ is a fraction of the dipole energy F_D (which is already small by itself) and makes it only temperature dependent to the lowest order. Secondly, the magnetic fields used in our experiments are kept small for purpose to stay close to the B-phase. Consequently, the difference in population is negligible, and also the angle θ_0 is nearly equal to θ_L . Nevertheless, the effect of the magnetic field on the direction of $\hat{\mathbf{n}}$ is important for the forming of the textures, which will be discussed later.

1.8 Coherence lengths

If we deal with spatial inhomogeneity in the superfluid, hence gradients in the order parameter, we should include the gradient free energy density part in equation (1.12). It is the equivalent of the gradient part in the Ginzburg Landau theory, see equation (1.10), and is given by:

$$F_{grad} = \frac{1}{2} \sum_{jl\mu} [K_1 (\nabla_j A_{\mu l}) (\nabla_j A_{\mu l}^*) + K_2 (\nabla_j A_{\mu l}) (\nabla_j A_{\mu j}^*) + K_3 (\nabla_j A_{\mu j}) (\nabla_j A_{\mu l}^*)]. \quad (1.31)$$

In the Ginzburg-Landau regime the coefficients do not depend on the order parameter, and are isotropic. However in a more general case the coefficients can be anisotropic in orbital and spin spaces. In the weak-coupling regime the coefficients ⁴ have been calculated [29]

$$K_1 = K_2 = K_3 \equiv K = \frac{1}{5} N_F \xi_0^2. \quad (1.32)$$

where N_F is again the density of quasi-particle states of both spin components in the normal phase at the Fermi energy and ξ_0 the coherence length at zero temperature. This length is corresponding to the size of the Cooper pair. The coherence length expressed in natural constants, Fermi velocity v_F and critical temperature T_c is given by:

$$\xi_0 = \left[\frac{7\zeta(3)}{48\pi^2} \right]^{1/2} \frac{\hbar v_F}{k_B T_c}. \quad (1.33)$$

At higher temperatures the coherence length grows and its temperature dependence is given by:

$$\xi(T) = \xi_0 (1 - T/T_c)^{-1/2}, \quad (1.34)$$

showing how it diverges at the transition temperature.

1.8.1 Coherence lengths of different interactions

The gradient energy density is minimized when the transition of the orientation of the order parameter is as smooth as possible. Typical length scales of this transition are indicated with a coherence length ξ . To give an estimation for the order of magnitude of such coherence length it is convenient to use the *London Limit*. Here the order parameter attains its equilibrium structure everywhere in bulk, where weak perturbation does not change its structure but merely influence the preferred direction in orbital and spin space (and phase) [19]. The gradient free energy density can be

⁴The weak-coupling limit is valid when the strongest interaction parameter V_L , forming the Cooper pairs, times the density of states $N(0)$, equals $N(0) |V_L| \ll 1$.

rewritten in terms of gradients of the symmetry variables only, and will be referred as the bending free energy density F_{bend} .

This bending free energy density for the B-phase, where ϕ is kept constant and $\theta = \theta_L$ is then given by:

$$F_{bend} = 2\frac{1}{2} \left(\frac{1}{2} K \Delta(T)^2 \right) \left\{ 4(\hat{\mathbf{n}} \times (\nabla \times \hat{\mathbf{n}}))^2 + \frac{13}{4}(\nabla \cdot \hat{\mathbf{n}})^2 + \frac{11}{4}(\hat{\mathbf{n}} \cdot \nabla \times \hat{\mathbf{n}})^2 \right. \\ \left. - \frac{\sqrt{15}}{2}(\nabla \cdot \hat{\mathbf{n}})(\hat{\mathbf{n}} \cdot \nabla \times \hat{\mathbf{n}}) + 4\nabla \cdot [(\hat{\mathbf{n}} \cdot \nabla)\hat{\mathbf{n}} - \hat{\mathbf{n}}(\nabla \cdot \hat{\mathbf{n}})] \right\} \approx \frac{1}{2} K \Delta(T)^2 \frac{1}{\xi_L^2}, \quad (1.35)$$

where $\Delta(T)$ is the energy gap of the B-phase and ξ_L is the healing length, which corresponds to the spatial variation of the texture. Comparing other energy densities with the bending energy density, one can make an estimation of the coherence length corresponding to that energy.

Dipole healing length

By comparing the dipole free energy (1.20) with the bending free energy (1.35) we find

$$\frac{1}{2} K \Delta(T)^2 \left(\frac{1}{\xi_D^B} \right)^2 \approx \frac{3}{5} g_D(T). \quad (1.36)$$

Using the definition of the dimensionless dipole coupling parameter λ_D (1.25) and K (1.32), the dipole healing length⁵ can be expressed as:

$$\xi_D^B \approx \sqrt{\frac{1}{6\lambda_D}} \xi_0. \quad (1.37)$$

While the expression is most accurate in the Ginzburg-Landau regime, the most important identity is that the healing length ξ_D^B is temperature independent. However, it does depend on pressure, since it is proportional with ξ_0 . Starting from melting pressure to zero bar, it varies between approximately 7 to 32 μm .

Magnetic healing length

The order of magnitude of the magnetic healing length ξ_H^B ⁶ can be derived by comparing the magnetic field orientation energy (1.29) with the bending free energy (1.35).

$$\frac{1}{2} K \Delta(T)^2 \left(\frac{1}{\xi_H^B} \right)^2 \approx \lambda_D N_F \frac{5}{12} \left(\frac{\gamma \hbar H}{1 + F_0^a} \right)^2 \frac{\beta_{345}^{WC} T}{\beta_{345} T_c}. \quad (1.38)$$

⁵Also called: dipole coherence length.

⁶Technically one should put $\xi_H^{B_2}$, however there should be no difference between the two, since the isotropic B-phase does not have a preferred direction, so it does not have a magnetic healing length.

Using the definition of K (1.32), the magnetic healing length can be expressed as:

$$\xi_H^B = \sqrt{\frac{12}{50}} \frac{1}{\sqrt{\lambda_D}} \frac{(1 + F_0^a)}{\gamma \hbar} \sqrt{\frac{\beta_{345}}{\beta_{345}^{WC}} \frac{\xi_0}{H}} \sqrt{\frac{T_c}{T}} \Delta(T). \quad (1.39)$$

Due to the approximations ⁷ the model is not accurate in detail for the whole temperature range. The limits, especially temperature near zero temperature, do not agree with the empirically found relations published in literature (see section 3.6 of this thesis.) However, it does describe the physical behavior. The healing length is zero at T_c and grows as temperature decreases. With the exception close to T_c the magnetic healing length ξ_H^B is longer than the dipole coherence length ξ_D^B . The inverse relation of the strength of the magnetic field H seems to be natural to first order, as one expects that the healing length will become smaller with higher field.

⁷Till second order of the magnetic field orientation, approximations in the relation $(\Delta_{\perp} - \Delta_{\parallel})\Delta_{\perp}$ and derived in the Ginzburg-Landau regime.

Chapter 2

Cell and read-out

2.1 Introduction

The NMR measurements on ^3He performed in this thesis are all characterized by their restricted geometry. Two different kinds of restricted geometry were studied. The first geometry was a cylinder with a diameter of 1 mm, in which we want to study spin waves formed in the B-phase of ^3He . The second geometry is once more cylindrical, however the diameter is now much smaller and is roughly 540 nm. The NMR signal coming from such a small cylinder is extremely small, and to increase the signal the measurement was performed with a bundle of those cylinders ¹. In this experiment we were searching for a new superfluid phase, namely the polar phase.

The configuration of the experimental cell was mostly determined by the dimensions of the experimental space in the dilution fridge. Nevertheless it was possible to create a cell in which both restricted areas were included, and could fit in the bore of a small magnet so that the NMR experiments could be performed. The magnet was designed to be as homogeneous as possible in the given configuration, to optimize the signal to noise ratio in the ^3He experiments. Also a fully new detection system for the rf-coils was simulated, tested and built to have an optimal read-out for the NMR absorption spectra. The experiment itself was performed in a home-built dilution fridge including a nuclear demagnetization stage, which is described in detail in the thesis of Eggenkamp [30].

2.2 Cell

A schematic drawing of the final cell is shown in figure 2.1. The cell is constructed on a block of copper, which fits on the experimental space of the nuclear stage and is 10 mm thick. In this way the cell with all the various components could be assembled

¹Actually it is a bundle of fibers.

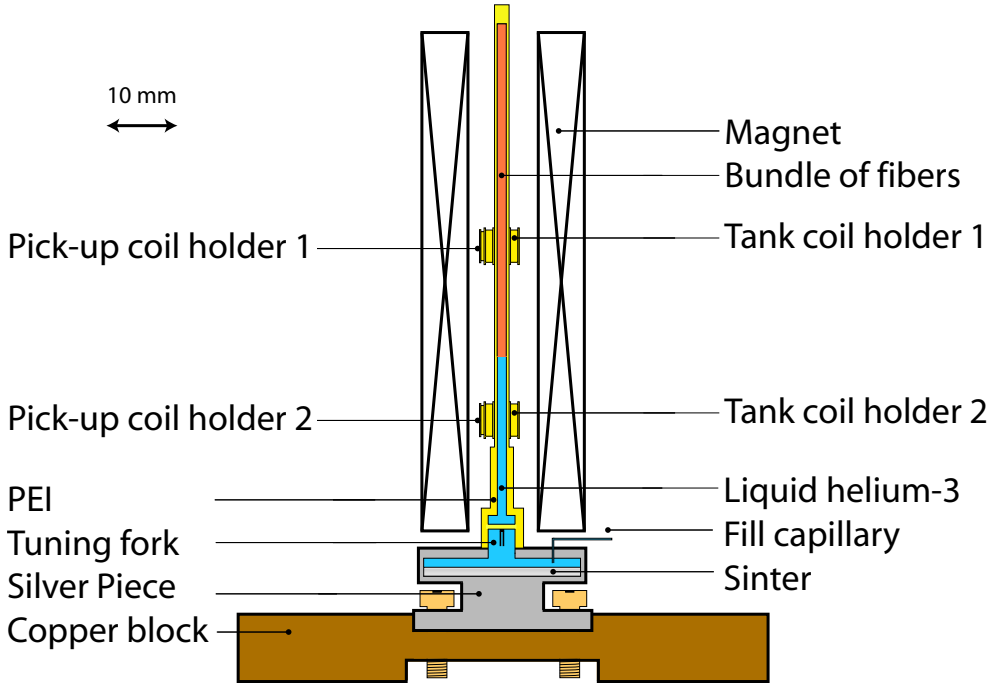


Figure 2.1: Cross section of the experimental cell.

outside the cryostat, including the magnet, and could easily be screwed on the nuclear stage. The cell itself mainly consists out of silver and PEI (Polyetherimide).

The silver piece sliced into the copper block, and was rigidly fixed with additional bolts. One should be sure that copper and silver pieces are squeezed sufficiently against each other, to prevent extra impedance for the thermal conduction. The silver piece itself, which has good thermal conducting properties at low temperatures [31], should cool the ^3He to the temperatures of the nuclear stage. Silver is preferred over copper, despite the fact that it has a lower thermal conductance, because its properties are more favorable in the presence of a magnetic field ². However, the interfacial thermal resistance, better known as the Kapitza resistance R_K , between the liquid ^3He and the silver becomes rather high at low temperatures. The amount of vibrations (phonons) is strongly decreased at low temperatures and in combination with the mismatch at the interface (low scatter probability) this gives a high Kapitza resistance. The temperature difference across such interface is given by

²The gyromagnetic ratio of silver is 7 times smaller than of copper. So by the same magnetic field the Zeeman splitting effects are smaller, resulting in less heating and cooling as the experimental magnet is swept during the measurements. These smaller Zeeman splitting effects are preferable during the measurement, this in contradiction for nuclear demagnetization cooling.

$$\Delta T = \frac{R_K \dot{Q}}{A}, \quad (2.1)$$

where \dot{Q} is the heat flow and A the surface area of the interface. In the case of an interface between ^3He and silver the Kapitza resistance at 2 mK is $R_K = 10^5 \text{ m}^2 \text{ K W}^{-1}$ [31]. To prevent the interface of becoming the highest impedance of the heat transport, the area should be made sufficiently large. This is accomplished by a silver sinter pressed on the silver piece. Here the sinter works as a sponge in the ^3He liquid and has an enormous surface area. The silver sinter was 0.5 mm thick and had an effective area of 25 m^2 , which gives a $\dot{Q}/\Delta T$ ratio of $2.5 \cdot 10^{-4} \text{ W K}^{-1}$. This is one order of magnitude better than the heat transport through helium in the cylinder, as we will see later, and made this interface not a limitation in the cool down process.

The part of the cell which fits into the magnet should be made of a non-metallic material. Otherwise it would lead to significant losses like eddy currents, which is bad for temperature stability and NMR measurements. For this purpose this part of the cell is mainly made out of polyetherimide PEI. PEI is a plastic which is easily to machine and has proven to be suitable to work with at low temperatures, meaning it does not crack after multiple cool downs ³. The disadvantage of working with PEI, whose molecular structure per unit polymer is given by $\text{C}_{37}\text{H}_{24}\text{O}_6\text{N}_2$, is the quantity of hydrogen atoms in it. The gyromagnetic ratio γ of hydrogen is relatively close to the one of ^3He (they differ approximately by a factor of ~ 1.31) and because the T_2 of hydrogen in the polymer is short (this will be discussed in more detail in section 2.7), the tail of the NMR absorption is visible at the resonance frequency of ^3He . From this point of view it is more desirable to work with quartz glass (SiO_2), it is also a non-metal and has not a net nuclear spin ⁴. However, the fabrication and machining of quartz glass cylinders is much more complicated. Together with the fact that several cell's needed to be constructed to find the optimal results for cooling the liquid, SNR of the NMR experiments, fiber gluing, etc., made it more convenient to construct the cell out of PEI.

The PEI part of the cell, starting from the silver sinter, is 80 mm long. It is cylindrically shaped and the part where the tank coils are positioned has an outer diameter of 2 mm. One cannot drill an 80 mm long hole through a cylinder of 2 mm, in fact the part exist of 4 different pieces. To make one rigid non-leaking solid piece, the separated pieces were constructed in such way that they could slide into each other, as illustrated in figure 2.2. This method took care that the outside diameter of the whole cylinder was 2 mm, which is important as the tank coil holders should be sliced over it in a later stage. The disadvantage is that we need a lot of the cylinder's material for a proper joint, which enabled us to create an inner diameter of more than

³Actually PEI is known of forming stress cracks, because by the fabrication of bulk PEI the outside cools faster than the inside. One can solve this problem by boiling the (un-machined) bulk of PEI in water for 20 minutes (boiling time is dependable an actual dimensions of the bulk piece) and gradually let it cool down to room temperature. This treatment releases the stress in the material.

⁴Technically oxygen and silicon do have isotopes which have a net nuclear spin, however their natural abundance is small 0.038 % and 4.6832 %, respectively. Besides, their gyromagnetic ratios are much smaller than of ^3He .



Figure 2.2: Illustration of piece of PEI. The total length is 30 mm and has an outside and inside diameter of 2 and 1 mm, respectively.

1 mm. All the pieces were carefully glued together from the inside. The used epoxy was (white) stycast 1266, which has a similar expansion coefficient as the plastic [31]. The PEI parts to the silver piece are in general (relative) risky joints, as the expansion coefficient of plastics is much higher than of metals. To increase the change of success, the two were glued over a relatively large area, also here stycast 1266 was used.

All pieces glued together results in the cell illustrated in figure 2.1. The ^3He enters the cell near the silver sinter through a small capillary, from where it fills the whole volume of the cell. The volume of experimental interest is the 75 mm long cylindrical tube with a diameter of 1 mm. This volume is divided into two sections, indicated with blue and red colors. The tank coil around the blue area is to perform NMR measurements of $^3\text{He-B}$ in a cylinder of 1 mm diameter. The tank coil around the red area is to perform NMR measurements of ^3He in small cylinders (diameters around 540 nm). In chapter 4, detailed information is given how those fibers are bundled and which properties they have. The rest of the volume is kept as small as possible, as the extra helium in the system only increase the heat capacity of the system. The total volume is estimated to be 0.34 cm^3 , which gives a total heat capacity of $\sim 4.24 \cdot 10^{-4} \text{ J/K}$ at 2 mK for zero pressure [32]. The thermal conductivity for those temperature and pressure is around $\sim 2 \text{ mW cm}^{-1} \text{ K}^{-1}$ [31], giving a $\dot{Q}/\Delta T$ ratio of $\sim 2 \cdot 10^{-5} \text{ W K}^{-1}$ in the cylinder. Roughly estimated, the temperature of the liquid in the cylinder, for typical used sweep rates of 0.31 mK/h , will be $0.7 \mu\text{K}$ behind compared to the nuclear stage (at the position of the MCT)⁵. Only significant slower sweep rates can reduce this gradient, as it is due to the geometrical property of the cell. However, we considered this feature acceptable, as it is of little consequence for the results.

In the cell, near the transition of the silver piece to the PEI part, a quartz tuning fork was installed, see figure 2.1. This tuning fork is a piezoelectric oscillator with a standard frequency of 2^{15} Hz (32.768 Hz). They are commercially available and extensively tested in liquid ^3He (and liquid ^4He) [33]. The resonance of the tuning fork has the same analogy of an electrical circuit with an inductor and capacitor in series. Sweeping through resonance will show a Lorentzian line shape. The damping of this oscillator is dominated by the viscosity of the liquid, for which the width at half height is

$$\Delta f \propto \sqrt{\eta}, \quad (2.2)$$

where η is the dynamic viscosity of the liquid. This makes the tuning fork an useful

⁵Most measurements were performed at lower temperatures for which the thermal conductivity is more beneficial for heat transfer, which made the temperature gradient even smaller.

viscometer of the liquid.

The temperature behavior of the viscosity of both the normal liquid and $^3\text{He-B}$ is known. The Fermi liquid theory says that the viscosity of the normal liquid is proportional with $\propto 1/T^2$, which means that $\Delta f \propto 1/T$. The viscosity of the B-phase is empirically described by Winkelmann *et al.* [34] for the hydrodynamic and ballistic regime. So, the tuning fork can be used as a secondary thermometer, which can give directly the temperature of the liquid. The reproducibility seems to be so good that it does not need to be recalibrated. In our case we mainly used the tuning fork to compare with the melting curve thermometer, to be sure the system is in equilibrium, or to know the temperature gradient between the nuclear stage and liquid in the cell.

2.3 Overview of used NMR techniques at helium-3 superfluids

The first experimental observations of superfluidity in helium-3 were performed by Osheroff, Richardson and Lee [8]. While these experiments were pressure measurements at the ^3He melting pressure it was directly clear that NMR measurements would reveal interesting additional information about the kinks discovered in the melting curve relation $P_{melt}(T)$. At that moment it was suggested that the kinks corresponded to magnetic transitions in the solid. However, in their NMR experiments Osheroff *et al.* found that both kinks correspond to a phase-transition in the liquid [35]. This discovery started the field in these 'strange' new anisotropic superfluids. The A-phase showed a frequency shift in the NMR spectrum, which increases by lowering the temperature and had, as Dave Lee termed it, a 'Pythagorean' relationship: $\omega_L^2 + \Omega_A^2(T)$. In the B-phase the resonance frequency jumped back to the Larmor frequency and the susceptibility reduced by cooling, which behavior is expected for a BCS-transition.

Already right after the discoveries of these superfluid phases the significance of NMR experiments was obvious. This became even clearer after the theoretical work of Leggett [20], who predicted that all superfluid states would have a different anisotropic susceptibility, for which one could expect different transverse frequency shifts. On top of that, he described that the ^3He liquid in the superfluid state could have a longitudinal NMR mode as well. Consequently NMR experiments form an extremely powerful method to distinguish the various superfluid phases.

In the first NMR experiments Osheroff *et al.* used the continuous wave NMR (cw-NMR) method. In this experiment the static magnetic field (\mathbf{B}_0) was varied between 3 and 85 mT, and the radio frequency coil (rf-coil) was made of copper, of which the wiring to room temperature is typically 1 to 2 meters long. To shield from pick-up noise one often uses coax cables or (shielded) twisted-pair wires. However, the consequence is that there is a parasitic capacitance (of the wires) parallel with the rf-coil (inductance in the coax cables does not play a significant role for these frequencies). In this way one creates an LC-circuit, of which the losses originate from both the rf-coil and the wiring to room temperature. The losses relative to the stored energy in the resonator (LC-circuit) are expressed by the quality factor

(Q). As explained in the next sections, the Q is proportional with the NMR signal. For optimal sensitivity the operating frequency should be matched to the resonance frequency of the LC-circuit. As the resonance frequency is often kept constant, one needs to tune the resonance frequency of the LC-circuit with a tunable capacitor at room temperature.

The most losses in such systems come from the wiring to room temperature, but by the lack of low temperature pre-amplifiers at that time, there was little one could do about the electronics inside the cryostat. As magnetic fields do influence the phase diagram of the superfluid ^3He , see figure 1.1, most NMR experiments are performed at relatively low frequencies, for which a typical Q of 100 could be achieved.

The first cw-NMR was a transverse resonance experiment, meaning that the static field \mathbf{B}_0 is perpendicular to rf-field \mathbf{B}_1 . A few years later Osheroff and Brinkman [36] did a longitudinal resonance experiment, hence the \mathbf{B}_1 is now parallel with \mathbf{B}_0 . These are not easy experiments, because the longitudinal component is independent of any external applied field. Nevertheless, in this experiment they succeeded to find the predicted longitudinal components by Leggett.

Also alternative methods to study the magnetization of the superfluids were devised and implemented. For example Paulson *et al.* measured the static magnetization of the superfluids with the help of an rf squid magnetometer [37].

The first pulse-NMR experiment on superfluid ^3He was also performed by Osheroff together with Corruccini [38]. This method can obtain the same information as in the case of cw-NMR, but is much more convenient if one wants to determine T_1 or T_2 . It is also possible to study the liquid in the non-linear regime. The magnetization, which is then far from equilibrium, gives interesting frequency shifts in the superfluid.

The disadvantage of pulse-NMR, especially at the lowest temperatures, is that it can generate more heat inside the cryostat. The heat input is also less regular than in the case of cw-NMR. In the case of cw-NMR the heat input is very regular and often (much) smaller, which makes it possible to keep the system in better thermal equilibrium during sweeping. The choice of method is depending on what one wants or can measure, what change (and how fast) needs to be observed and at which temperatures.

As in time smaller samples became interesting (study surface effects, textures, etc.), and one even wanted to measure (single) vortices in superfluid ^3He , more sensitive NMR probes were needed, which means very high-Q circuits became necessary. As the parasitic capacitance of the wiring was the dominating Q spoiler of the system, the LC-circuit should be decoupled from it. This can be realized by coupling the LC-circuit directly with a pre-amplifier at low temperatures. It is technically hard to implement a pre-amplifier for low temperatures with sufficiently high input impedance for operating frequencies at 1 MHz (this frequency is set by the desirable magnetic fields for the experiment). Nevertheless the Helsinki group managed to fabricate a low temperature pre-amplifier (GaAs FET) for cw-NMR [39] [40], and Richards *et al.* for pulse-NMR [41]. If the copper wire of the rf-coil in the LC-circuit is replaced by superconducting wire and put parallel to a very low loss capacitor one could get, in combination with the low temperature pre-amplifier, a Q of typically $10^4 - 10^5$. The

dominating noise source is these systems are the pre-amplifiers themselves, and have typically a noise voltage of $1 \text{ nV}/\sqrt{\text{Hz}}$. This represents a significant improvement of the sensitivity with respect to the earlier NMR circuits.

The change from copper to superconductor wires is good for the quality factor of the system, but can decrease the homogeneity of the \mathbf{B}_0 in the sample. As the diamagnetism of copper is very small \mathbf{B}_0 will hardly change, and the homogeneity of the external magnetic field is as calculated. In the case of superconductors the magnetic field lines will be expelled from the wires, which is bad for the homogeneity of the magnetic field if the coil is not too far from the sample. Dimitriev *et al.* [42] showed that they could restore the homogeneity of the magnetic field through the sample using coils made of type II superconductors (Nb, NbTi). They made the superconducting wires of the rf-coils normal for a few seconds at the moment that the value of the applied \mathbf{B}_0 was close to the experimentally desirable working value. In the normal state the magnetic field lines rearrange themselves as in the case of the copper coil. When the coil becomes superconducting again a large number of vortices (field lines) remain in the superconductor due to pinning effects, which reduces the distortion of \mathbf{B}_0 considerably.

Parallel to the development of low temperature pre-amplifiers one started to use dc SQUIDS. Freeman *et al.* presented a dc SQUID in open loop mode working at 1.9 MHz [43]. However, the noise temperature (300 mK) was limited by the read out electronics and was considered relatively large. Recently, Levitin *et al.* [44] have fabricated a pulsed NMR spectrometer around a two-stage dc SQUID, which was the result of a ten-year research program. The use of a two-stage SQUID amplifier improves the noise performance significantly and they claimed to have a noise temperature smaller than 10 mK. However, the Q of these system are deliberate put back to 300, this to prevent that the SQUID becomes normal when a pulse is given. Nevertheless, the SNR is typically one order of magnitude better then in the case of a low temperature pre-amplifier. This is desirable as they probe a single quasi-2D system, which has a very small filling factor.

At the moment this SQUID technology supplies probably the most sensitive probe for low frequency NMR on superfluid ^3He . However, together with the low temperature pre-amplifier they are both active systems, for which the stability can be questionable at long time scales. As we planned to make a continuous temperature sweep which could take days, we needed reliable detection electronics. We believed we could accomplish that by using only passive components. However, as our system of interest is a quasi-1D system, and the used samples have a small filling factor and volume (total amount of measurable helium-3 atoms will be of the order of a μmole), we needed to maintain a high Q resonator. We show that we could realize this by decoupling our LC-circuit with a small series capacitor and by reading-out the NMR signal picked-up from the rf-coil with a mutual inductance of a weakly coupled transformer.

The next sections of this chapter are about the simulations, development and testing of this circuit. It turned out that the Q and the SNR is comparable with the low temperature pre-amplifier detection scheme. Also the stability was what we hoped for, and the detection circuit did not let us down during very lengthy temperature

sweeps.

2.4 Read-out system

Nuclear magnetic resonance NMR is the method of choice to identify the different superfluid states of ^3He . A resonant circuit consisting of a capacitor C_T parallel with an inductor L_T (tank circuit) is used to pick up the NMR signal in a continuous wave experiment. The quality factor Q of the tank circuit is of great importance for a low-frequency NMR measurement, especially when the filling factor is small.

In the cw-NMR experiment, where the ^3He cell is positioned in the coil of the tank circuit, the tank circuit is kept at the resonance frequency ω_0 with a function generator. The rf-field \mathbf{B}_1 of the tank coil, L_T in figure 2.3, is perpendicular to an external applied magnetic field \mathbf{B}_0 . The \mathbf{B}_0 adjusts the angular velocity ω of the ^3He spins via: $\omega = \gamma|\mathbf{B}_0|$. The system is in resonance when the angular velocity ω matches the resonance frequency ω_0 of the tank circuit [45]. In resonance the resistance of the tank circuit is modified due to the power absorbed by the spin system, and the fractional change is given by:

$$\frac{\Delta R}{R_0} = \frac{L_T \omega_0}{R_0} 4\pi\chi'' = 4\pi\chi''Q, \quad (2.3)$$

where χ'' is derived from the Bloch equations [46], see also equation (2.11) and R_0 the resistance of the tank circuit in the absence of a sample. The change in impedance can be measured as a voltage change ΔV over the tank circuit. The proportionality of ΔV with Q makes it desirable to keep the quality factor as high as possible.

As one can see from figure 2.3, a function generator is connected to the tank circuit with a transmission line (coax cable). This transmission line goes from room temperature (position function generator) through the cryostat and is connected to

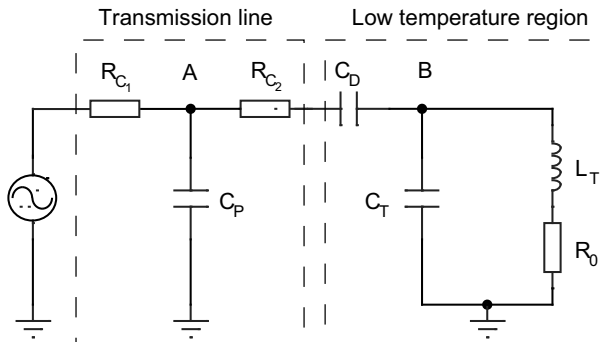


Figure 2.3: Function generator connected with a transmission line to the tank circuit. The tank circuit is decoupled from the parasitic capacitance of the transmission line with a capacitor C_D .

the tank circuit at the nuclear stage, the final set-up (including feedback) is illustrated in figure 2.19. Two properties of the transmission line concerning our cryostat and probe system are important. First, how much additional heat input is transported into the cryostat? The additional heat input will increase the boil off rate of the helium-4 in the helium bath, and can disturb the optimal operation of the dilution fridge. Secondly, how much does the transmission line load the tank circuit? The resistance of the transmission line in combination with its parasitic capacitance will influence the Q of the tank circuit.

The transmission line is modeled as two resistors R_{C_1} , R_{C_2} and one parasitic capacitance C_P as shown figure 2.3. This approximation is made plausible in appendix A.4. The resistors R_{C_1} and R_{C_2} are equal and form together the total resistance in the transmission line, and C_P corresponds with the total (parasitic) capacitance in the line. The tank circuit and transmission line are decoupled by a small decoupling capacitor C_D . If not, C_P will be directly parallel with both C_T and L_T (forming a new LC-circuit), and will play a significant role in the resonance frequency ⁶ of the LC-circuit. More importantly, the resistance R_{C_2} causes now, together with R_0 , the dissipation in the LC-circuit. R_{C_2} , normally much bigger than R_0 , will spoil the Q of the tank circuit. In the next section it will be explained how capacitor C_D can successfully decouple the transmission line from the tank circuit, in order to conserve a high Q .

Figure 2.3 illustrates how the function generator is connected to the tank circuit. Of course one is more interested how to read-out the voltage change ΔV over the tank circuit, due to the fractional change in impedance as one goes through resonance. A direct connection with a transmission line will again load the circuit, and once more spoil the Q of the resonator. One way to maintain a high Q is with the use of a cold pre-amplifier [40]. However, we believe we could create a more reliable (stable) probe system with passive components. We suggest here two passive methods to detect the NMR signal. The first method reads the signal over the parasitic capacitance of the coax cable (transmission line), which is placed in series with the tank circuit, see section 2.4.2. The second method is based on the mutual inductance of a transformer, see section 2.4.3.

Because of the dimensions of the cryostat the transmission line is typically 1-2 m long, meaning that the total parasitic capacitance C_P is typically 200 pF. The type of wire is important because of the additional heat input. Low resistivity wires, like copper, will maintain a high Q in the tank circuit, but are good thermal conductors. Phosphor bronze wires are good thermal isolators, however the resistivity is much higher which will influence the Q much more. To see the effect of the resistance of the transmission line both passive methods are simulated with a total resistance of 2, 20 and 60 Ω and a C_P of 200 pF. The R_C ⁷ of 1 Ω represents a transmission line made of copper, while the R_C of 10 and 30 Ω represent two different kinds of phosphor bronze transmission lines.

In total two tank circuits, one for each experiment, are built. Tank circuit 1 uses

⁶The resonance frequency of an LC-circuit is given by: $\omega_0 = 1/\sqrt{LC}$.

⁷The total resistance of the transmission line equals $R_{C_1} + R_{C_2}$. $R_{C_1} = R_{C_2} = R_C$.

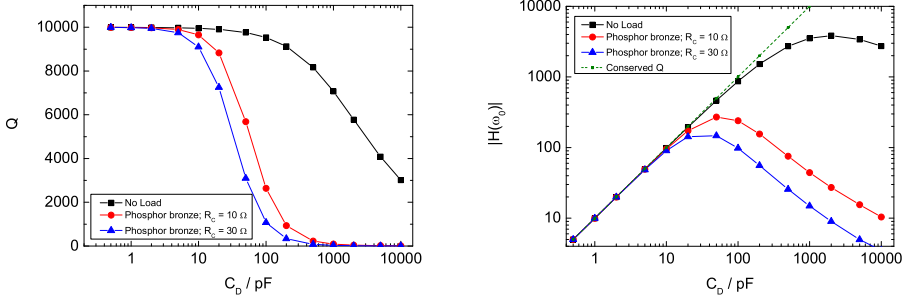
the upper tank coil, as illustrated in figure 2.1, and tank circuit 2 uses the lower tank coil. Eventually we used copper wires for tank circuit 1, and phosphor bronze wires for tank circuit 2.

2.4.1 The decoupling capacitor

A high Q tank circuit ($Q > 10,000$), for frequencies around 500 kHz and temperatures under 10 mK, can be made with an ultra-high Q capacitor [47] and a handmade coil of superconducting wire, see section 2.6. However, connecting this circuit to a function generator or spectrum analyzer puts an extra parallel capacitor over the tank circuit, due to the capacitance C_P of the coax cables. Not only will this shift the resonance frequency ω_0 of the circuit, but more important it will decrease the Q , due to the losses in the coax cable.

To prevent this from happening one can decouple the circuit by putting a high impedance in series. For passive decoupling around 500 kHz a low value capacitor is preferable, see figure 2.3. A resistor will give too much dissipation for low temperature experiments, besides it increases the noise level, and a coil of high inductance is practically impossible to make and unfavorable for the magnetic fields it creates, which may interfere with the experiment.

For an ideal case, which means no losses in the tank circuit ($R_0 = 0$) and a



(a) Simulation results of the Q of the tank circuit as function of C_D . Compared for no load and two different phosphor bronze transmission lines with an R_C of 10 Ω and 30 Ω , respectively.

(b) Gain at resonance as function of C_D . For conserved Q the gain is proportional with C_D , deviation is caused by extra losses and shift of resonance frequency. Simulations were done for no load and two different phosphor bronze transmission lines with an R_C of 10 Ω and 30 Ω , respectively.

Figure 2.4: For all the simulations the used parameters of the tank circuit are: $C_T = 1$ nF, $L_T = 100$ μ H and $R_0 \approx 0.0314$ Ω . The parasitic capacitance C_P is 200 pF.

perfect transmission line (C_P and R_C both zero), the frequency dependent voltage gain ($|H(\omega)| = |V_B/V_A|$)⁸ over the tank circuit indicated at point B in figure 2.3 is given by the following equation:

$$|H(\omega)| = \left| \frac{Z_{Tank}}{Z_{Tank} + Z_D} \right| = \left| \frac{\omega^2 L_T C_D}{\omega^2 L_T (C_T + C_D) - 1} \right|, \quad (2.4)$$

where Z_D is the impedance of the decoupling capacitor, and Z_{Tank} of the tank circuit. From this equation it is clear that C_D shifts the ω_0 of the LC-circuit for values near or larger than C_T . In most situations this is undesirable and one should choose $C_D \ll C_T$.

Simulations [48] (as function of C_D) of the tank circuit with a Q of 10.000, inductor L_T of 100 μH and a C_T of 1 nF loaded with a transmission line are shown in figure 2.4(a). The parameters for the transmission line are based on the wiring of a typical cryostat. The parasitic capacitance is around 200 pF and the losses are dominated by the phosphor bronze transmission line through the helium bath. Simulations were done for phosphor bronze cables with an R_C of 10 and 30 Ω , respectively. The Q of the tank circuit (B to ground) is determined from the frequency sweep (Lorentzian) as simulated, and compared with no load (ideal transmission line). As expected the Q can be maintained if one uses small enough C_D (high enough coupling impedance). More losses in the transmission line will decrease the Q more for the same C_D . In the case of no losses in the transmission line the width of the Lorentzian stays constant, but for big C_D (low impedance) the resonance frequency ω_0 shifts to a lower value, as shown in equation (2.4). Consequently the Q of the circuit as a whole drops.

So, a capacitor in series with an LC-circuit does more than decoupling only, it influences the resonance frequency and determines the voltage gain over the tank circuit. In the limit of small C_D (large decoupling impedance) the Q of the tank circuit is not influenced, consequently the gain at resonance will be

$$|H(\omega_0)| = \frac{C_D}{C_T} Q. \quad (2.5)$$

However, as is simulated and shown in figure 2.4(a), large C_D will influence the Q and with that the voltage gain over the tank circuit. The simulations of the gain $|H(\omega_0)|$ over the tank circuit at resonance (ω_0) for increasing C_D are plotted in figure 2.4(b). For the maximal gain with our simulated phosphor bronze cables we should match C_D to C_P , typically one order of magnitude lower.

2.4.2 Measuring over the parasitic capacitance

To measure the NMR signal, the drop of ΔV over the tank circuit, one should connect the tank circuit with an additional transmission line. Direct connection will spoil the Q . One way to prevent the tank circuit from loading is by connecting the pre-amplifier (at room temperature) with the tank circuit in such way that the C_{P_2} of

⁸ V_A is the voltage given by the function generator.

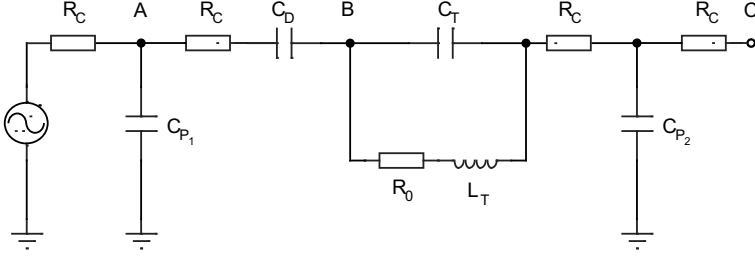


Figure 2.5: In this configuration the tank circuit is directly connected with a transmission line to room temperature. The pre-amplifier (at room temperature) is connected to point C. Due to the high input impedance of the pre-amplifier, the tank circuit is connected to the ground via the parasitic capacitance C_{P_2} of the transmission line. The NMR signal, generated in the tank circuit, is measured as a voltage change over C_{P_2} .

the transmission line⁹ is in series with the tank circuit, see figure 2.5. Here the tank circuit is not (directly) connected to ground. Point C is connected to the pre-amplifier at room temperature. The input impedance of the pre-amplifier needs to be an order or magnitude higher compared to the parasitic impedance $Z_{C_{P_2}}$ of the transmission line, meaning that the tank circuit is effectively connected to ground via C_{P_2} .

In this configuration C_{P_2} , together with C_D , forms the decoupling capacitance for the tank circuit with respect to the transmission line from the function generator (R_C is small compared to both $Z_{C_{P_2}}$ and Z_{C_D}). As long as C_D is small compared to C_{P_2} the loading is minimized.

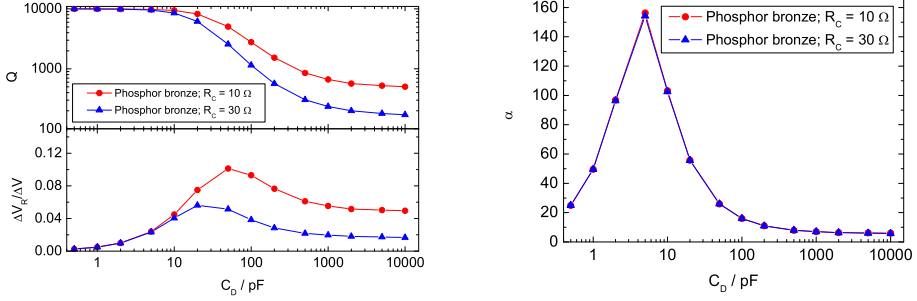
The NMR signal in this configuration is measured over C_{P_2} at point C (V_C). In the experiment the voltage amplitude at point A (V_A) with respect to ground is kept constant. The voltage drop ΔV , due to the NMR absorption, over the tank circuit is then distributed over the capacitors C_D and C_{P_2} (we neglect the voltage drop over the R_C 's, which are small compared to the other impedances in the system). The fraction of the NMR signal ΔV_R seen over C_{P_2} is thus proportional with $C_D/(C_{P_2} + C_D)$.

To maximize this fraction, one should increase the ratio between C_D and C_{P_2} . Desirable is to make C_{P_2} as small as possible, but practically (length of coax in cryostat) much smaller than 200 pF is hard. Varying C_D is more feasible. However, this may introduce more losses to the tank circuit.

Simulations for two different phosphor bronze coaxes (transmission lines) are made, see figure 2.6(a). $C_{P_2} = 200$ pF with an $R_C = 10, 30 \Omega$, respectively. It should be emphasized that the output resistance of the function generator (50Ω) and the input impedance of the pre-amplifier (25 pF and $100 \text{ M}\Omega$) are included in the simulations.

As expected, the Q as function of C_D will be less for higher resistance R_C . The

⁹The parasitic capacitance of each transmission line is indicated with C_{P_1} and C_{P_2} , respectively. However, one should keep in mind that $C_{P_1} = C_{P_2} = C_P \approx 200$ pF.



(a) Simulation results of Q and $\Delta V_R/\Delta V$ as function of C_D for 2 different phosphor bronze transmission lines with an R_C of 10 and 30 Ω , respectively.

(b) Simulation results of α from equation (2.6) as function of C_D . Both phosphor bronze transmission lines, with an R_C of 10 and 30 Ω , show (approximately) the same results, and have the best SNR by a C_D of 5 pF.

Figure 2.6: For all the simulations the used parameters of the tank circuit are: $C_T = 1$ nF, $L_T = 100$ μ H and $R_0 \approx 0.0314$ Ω . The parasitic capacitance C_P is 200 pF.

ratio $\Delta V_R/\Delta V$, where ΔV is the NMR signal in the tank circuit, can be optimized with the right C_D .

While a high ratio of $\Delta V_R/\Delta V$ can be obtained, it is not as important as a high signal to noise ratio SNR. In the simulations we have assumed that the dominating noise source is the thermal noise ΔV_{noise} generated in the transmission lines from room temperature to the tank circuit at the nuclear stage. An assumption which was not entirely correct as is pointed out in section 2.8. We assumed that the noise generated in the transmission lines (to and from the tank circuit) are equal. The noise generated by the function generator and the pre-amplifier are considered to be much smaller, and are for this reason neglected. Also the thermal noise generated in the tank circuit was in this stage considered to be much smaller than in the transmission lines, due to the low temperature ($T < 10$ mK) and small R_0 (~ 0.0314 Ω).

The voltage generated with the function generator and with a frequency matching the resonance frequency of the tank circuit, as is pointed out in equation (2.5) and figure 2.4(b), is amplified over the tank circuit. Of course the same happens with the noise ΔV_{noise} generated in the incoming transmission line with the frequencies matching the resonance frequency. Absolutely speaking, the noise over the tank circuit is higher for more gain.

The NMR signal ΔV is proportional to $V_0 \xi \chi'' Q$, where V_0 is the voltage over the tank circuit and ξ the filling factor. The fraction of the NMR signal ΔV_R seen over

C_{P_2} is thus $\Delta V \cdot C_D / (C_{P_2} + C_D)$.

The noise generated by the incoming transmission line and corresponding to the frequency of the tank circuit ω_0 is amplified as $\Delta V_{noise} |H(\omega_0)|$, see equation (2.5). We consider only the frequencies close to the resonance frequencies of the tank circuit, as it filters out the frequencies far from the resonance frequency. Moreover the signal (after the pre-amplifier) is measured with a lock-in, which adds an extra filter. The fraction of the noise seen over C_{P_2} is $\Delta V_{noise} |H(\omega_0)| \cdot C_D / (C_{P_2} + C_D)$. In the transmission line from the tank circuit to the pre-amplifier an additional noise voltage V_{noise} is generated, and the total noise measured with the lock-in (additional noise of pre-amplifier or lock-in is neglected) is then given by: $\sqrt{(\Delta V_{noise} |H(\omega_0)| \cdot C_D / (C_{P_2} + C_D))^2 + \Delta V_{noise}^2}$. Within these assumptions the SNR for the obtained NMR signal is given by:

$$\text{SNR} \sim \frac{V_0 \xi \chi''}{\Delta V_{noise}} \frac{Q \frac{C_D}{C_D + C_P}}{\sqrt{(|H(\omega_0)| \frac{C_D}{C_D + C_P})^2 + 1}} \equiv \frac{V_0 \xi \chi''}{\Delta V_{noise}} \alpha, \quad (2.6)$$

α is plotted in figure 2.6(b) as function of C_D . Both graphs overlap, and the best SNR is found for C_D close to 5 pF. This is understandable from the equation (2.6), because for small C_D the 1 in the nominator is dominating and the Q for both configurations is close to 10.000, see figure 2.6(a). For big C_D the $\text{SNR} \sim Q / |H(\omega_0)| \sim C_T / C_D$, see equation (2.5), which is again the same for both values of R_C . Consequently, the best SNR for both configurations is close to the same value of C_D , which is 2.5 % of the actual¹⁰ NMR signal.

2.4.3 Mutual inductance

An alternative way to read out the NMR signal is to make use of the mutual inductance M between two coils, see figure 2.7. Here the voltage over the tank coil is related to the voltage over the pick-up coil, which makes it possible to read out the NMR signal. The pick-up coil is connected to the pre-amplifier at room temperature via a transmission line. The effect of the load of the transmission line on the tank circuit could be limited by reducing the coupling between tank and pick-up coil. The relation of the mutual induction between two coupled inductors is given by the following relation:

$$M = k \sqrt{L_T L_P}, \quad (2.7)$$

where k is the coupling coefficient, L_T the inductance of the tank coil and L_P the inductance of the pick-up coil. When the inductors are completely coupled ($k = 1$), the tank circuit is maximally loaded. Consequently the Q of the tank circuit will drop due to the losses in the coax cable. To lower the load the inductors should be coupled weaker, which can be done by putting the pick-up coil further away from the tank coil. However, the voltage read from the tank circuit with the pick-up coil

¹⁰Actual is here a bit misleading term. The signal is compared with a tank circuit which is not loaded.

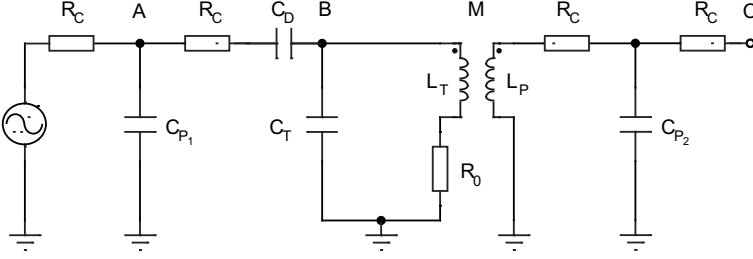
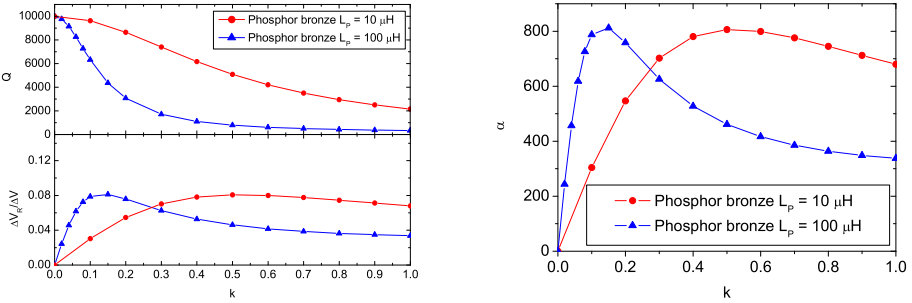


Figure 2.7: In this configuration the tank coil L_T is probed with a pick-up coil L_P , and the NMR signal is measured by reading out the pick-up coil. This pick-up coil is connected, through a transmission line, to a pre-amplifier at room temperature (Point C). The load on the tank circuit is tuned by the coupling between tank and pick-up coil.

is proportional with $k\sqrt{L_P/L_T}$. To maximize the read-out of the NMR absorption signal, one should optimize the product $k\sqrt{L_P/L_T} \cdot Q(k)$.

To minimize the load from the transmission line coming from the function generator, as discussed before, one should take the C_D as low as practically possible (0.5



(a) Simulation results of Q and $\Delta V_R/\Delta V$ as function of k for 2 different pick-up coils. The pick-coils have an induction of $10 \mu\text{H}$ and $100 \mu\text{H}$, respectively. The phosphor bronze transmission line had an R_C of 30Ω .

(b) Simulation results of α from equation (2.8) as function of k . Both pick-up coils give the same maximal value, but by different coupling with the tank circuit.

Figure 2.8: For all the simulations the used parameters of the tank circuit are: $C_D = 0.5 \text{ pF}$, $C_T = 1 \text{ nF}$, $L_T = 100 \mu\text{H}$ and $R_0 \approx 0.0314 \Omega$. The parasitic capacitance C_P is 200 pF .

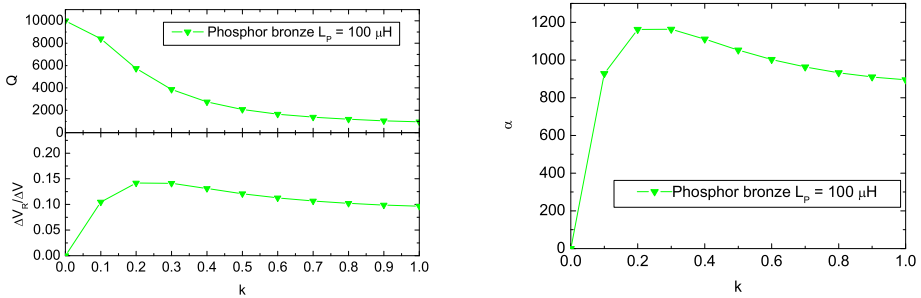
pF). Two simulations of this mutual inductance configuration (figure 2.7) with phosphor bronze transmission lines, both with R_C of 30 Ω and C_P of 200 pF, but with different inductance L_P for the pick-up coils are shown in figure 2.8(a). The upper figure shows the changing of the Q as function of k . For the same value of k the Q is higher for lower L_P , which makes sense since a lower voltage transfer causes less losses 'seen' from the transmission line into the tank circuit. However, as illustrated in figure 2.8(a) (lower panel), the NMR signal ΔV_R compared to ΔV has the same maximum value for the two different pick-up coils, only at different k .

As discussed before, the noise over the tank circuit is higher for higher gain and if we again use the same assumptions as in the previous section, the SNR for this circuit is given by:

$$\text{SNR} = \frac{V_0 \xi \chi''}{\Delta V_{\text{noise}}} \frac{Q k \sqrt{\frac{L_P}{L_T}}}{\sqrt{(|H(\omega_0)| k \sqrt{\frac{L_P}{L_T}})^2 + 1}} \equiv \frac{V_0 \xi \chi''}{\Delta V_{\text{noise}}} \alpha. \quad (2.8)$$

However, due to the choice of C_D (0.5 pF), see equation (2.5), the (noise) gain is kept as small as possible. Together with the fact that the Q is high when k is low and vice versa, the total noise measured with the lock-in is not changing much as function of k . Consequently, the best SNR, see figure 2.8(b), is proportional with V_R , for which one can get 8 % of the actual¹⁰ NMR signal.

Results of the simulation with an R_C of 10 Ω , C_P of 200 pF and a pick-up coil



(a) Simulation result of Q and $\Delta V_R/\Delta V$ as function of k for pick-up coil with an L_P of 100 μH . The phosphor bronze transmission line had an R_C of 10 Ω .

(b) Simulation result of α from equation (2.8) as function of k for pick-up coil with L_P of 100 μH and R_C of 10 Ω .

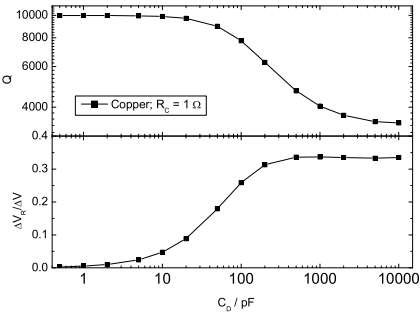
Figure 2.9: For all the simulations the used parameters of the tank circuit are: $C_D = 0.5$ pF, $C_T = 1$ nF, $L_T = 100 \mu\text{H}$ and $R_0 \approx 0.0314 \Omega$. C_P is 200 pF.

of $100 \mu\text{H}$ are shown in figures 2.9(a) and 2.9(b). As expected, due to the lower R_C , the system can be coupled stronger for maximal SNR. In this configuration it is even possible to get 14 % of the actual NMR signal.

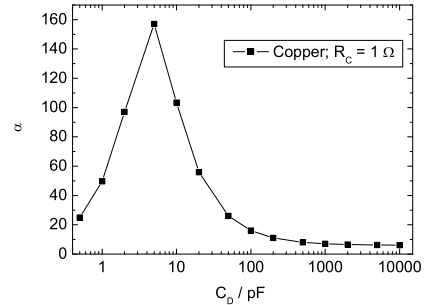
2.4.4 Copper wiring to room temperature

If one could replace the phosphor bronze transmission lines for copper transmission lines, so that the heat input in the system is still tolerable, one may reduce the losses generated in the transmission lines significantly. In this case a R_C of 1Ω (total resistance of the transmission line is than $2R_C = 2 \Omega$) can be achieved. However, the C_P will still be typically 200 pF.

The simulations when the transmission line is put in series with the tank circuit are shown in the figures 2.10(a) and 2.10(b). Because of the low dissipation in the system the Q , as function of C_D , drops in a similar way as in figure 2.4(a) where the tank circuit is not loaded. The ratio between $\Delta V_R/\Delta V$ is maximum with a C_D of 1000 pF. However, looking at α (SNR) the maximum is still found for a C_D of 5 pF, as in the case with the phosphor bronze cables. This is in agreement with the explanation given in the section 2.4.2, where the phosphor bronze cables were considered. So, independent of the wiring, but with typical value of C_P (200 pF), the best SNR is always around a C_D of 5 pF, no matter the dissipation. This also implies that, like in the case of phosphor bronze cables, only 2.5 % of the actual NMR signal can be read out.

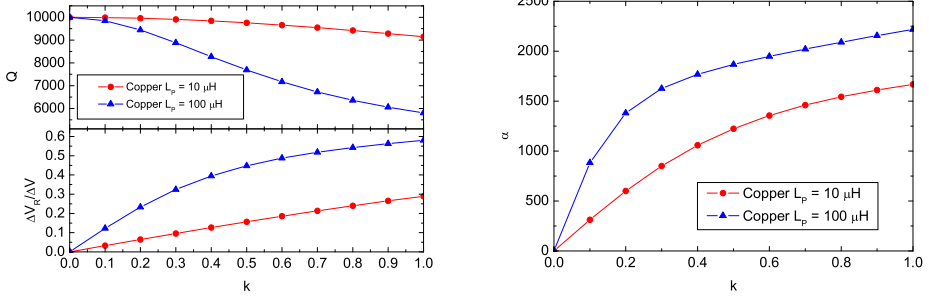


(a) Simulation results of Q and $\Delta V_R/\Delta V$ as function of C_D for a copper transmission line with an R_C of 1Ω .



(b) Simulation results of α from equation (2.6) as function of C_D . The best SNR is found by a C_D of 5 pF, which is similar to the phosphor bronze transmission lines.

Figure 2.10: For all the simulations the used parameters of the tank circuit are: $C_T = 1 \text{ nF}$, $L_T = 100 \mu\text{H}$ and $R_0 \approx 0.0314 \Omega$. The parasitic capacitance C_P is 200 pF.



(a) Simulation results of Q and $\Delta V_R/\Delta V$ as function of k for 2 different pick-up coils. The pick-coils had an induction of $10 \mu\text{H}$ and $100 \mu\text{H}$, respectively. The copper transmission line had an R_C of 1Ω .

(b) Simulation results of α from equation (2.8) as function of k for pick-up coils with L_P of $10 \mu\text{H}$ and $100 \mu\text{H}$, respectively. The copper transmission line had an R_C of 1Ω .

Figure 2.11: For all the simulations the used parameters of the tank circuit are: $C_D = 0.5 \text{ pF}$, $C_T = 1 \text{ nF}$, $L_T = 100 \mu\text{H}$ and $R_0 \approx 0.0314 \Omega$. The parasitic capacitance C_P is 200 pF .

The results in figures 2.11(a) and 2.11(b) are obtained by simulating the weakly coupled transformer with copper $R_C = 1 \Omega$ and an inductance L_P of 10 and $100 \mu\text{H}$, respectively. In this case we see that the Q of the system decreases slowly as the coupling is made stronger. The Q of the tank circuit when fully coupled ($k = 1$) is, due to the low losses in the transmission line, relatively high compared to the unloaded tank circuit. When the system is fully coupled with an inductance L_P of $100 \mu\text{H}$, which is equivalent to direct read-out of the tank circuit, one can still achieve a Q of 6000 . The ratio $\Delta V_R/\Delta V$ for these inductances is getting better by stronger coupling, which suggests, as can be seen from figure 2.11(b), that in this case the best SNR is achieved by maximal coupling. For this reason there is no benefit in working with a weakly coupled transformer, as the losses in the transmission lines are too low. However, if one is able to increase the Q of the tank circuit in such a way that the ratio $R_C/R_0 \approx 100$, it is preferable to use the weakly coupled transformer again. Also when one has $C_P \gg 200 \text{ pF}$ this configuration is better.

In general one can say that a weakly coupled transformer is useful when $R_0 < (\frac{C_P}{C_T})^2 \sqrt{\frac{C_T + C_P}{C_T}} R_C$, where $(\frac{C_T}{C_P})^2 \frac{R_0}{R_C}$ compares the total dissipation between the tank circuit and transmission line and the term $\sqrt{\frac{C_T + C_P}{C_T}}$ the relative change of the Q .

2.4.5 Considerations

In the methods concerning the phosphor bronze transmission line it is possible to obtain a high Q for the tank circuit. The weakly decoupled inductors can get the best SNR, for parameters realistic for wiring of a cryostat, which corresponds to 8 - 14 % of the NMR signal of the unloaded tank circuit. However, in practice it may be hard to couple the pick-up coil weakly enough to the tank coil for optimal result. Another disadvantage can be that there is not enough space in the magnet to place the pick-up coil near the tank coil. One should also keep in mind that, if one uses a pick-up coil of superconducting wire, this coil may have a negative effect on the homogeneity of the magnetic field B_0 .

To measure directly over the parasitic capacitance of the transmission line the best SNR corresponds of 2.5 % of the NMR signal of on unloaded tank circuit. The SNR may be lower than the previous method, but optimizing the system is practically much easier.

Concerning the configuration with low dissipation in the cabling of the system, like in the case of copper wires, both methods will not be more efficient than when the system is read-out directly. In general one can say that the weakly coupled transformer method is useful when $R_0 < (\frac{C_P}{C_T})^2 \sqrt{\frac{C_T + C_P}{C_T}} R_C$.

Eventually we used 2 different kinds of transmission lines, for two different tank circuits. The first transmission line was made of copper but had an R_C of 2 Ω , the second transmission line was of phosphor bronze with an R_C of 28 Ω , see also section 2.6.1. The best SNR is, as simulated with these transmission lines, when both tank circuits are read-out by the mutual inductance technique. Consequently the choice of read-out of our experiment is by the mutual inductance of a weakly coupled transformer.

2.5 Experimental Magnet

The magnet providing the B_0 magnetizes the sample as $M = \chi H_0$. Here χ is the dynamic susceptibility which can be rewritten in terms of dispersion χ' and absorption χ'' as:

$$\chi = \chi' - j\chi'', \quad (2.9)$$

χ' and χ'' themselves are, including the saturation term [49], given by

$$\chi'(\omega) = \frac{\chi_0(H_0)}{2} \omega_0 T_2 \frac{(\omega - \omega_0)T_2}{1 + (\omega - \omega_0)^2 T_2^2 + \gamma^2 B_1^2 T_1 T_2}, \quad (2.10)$$

$$\chi''(\omega) = \frac{\chi_0(H_0)}{2} \omega_0 T_2 \frac{1}{1 + (\omega - \omega_0)^2 T_2^2 + \gamma^2 B_1^2 T_1 T_2}. \quad (2.11)$$

The equations are characterized by two time constants T_1 , T_2 , and χ_0 the static susceptibility. The spin lattice relaxation time T_1 is the typical time for the spins to

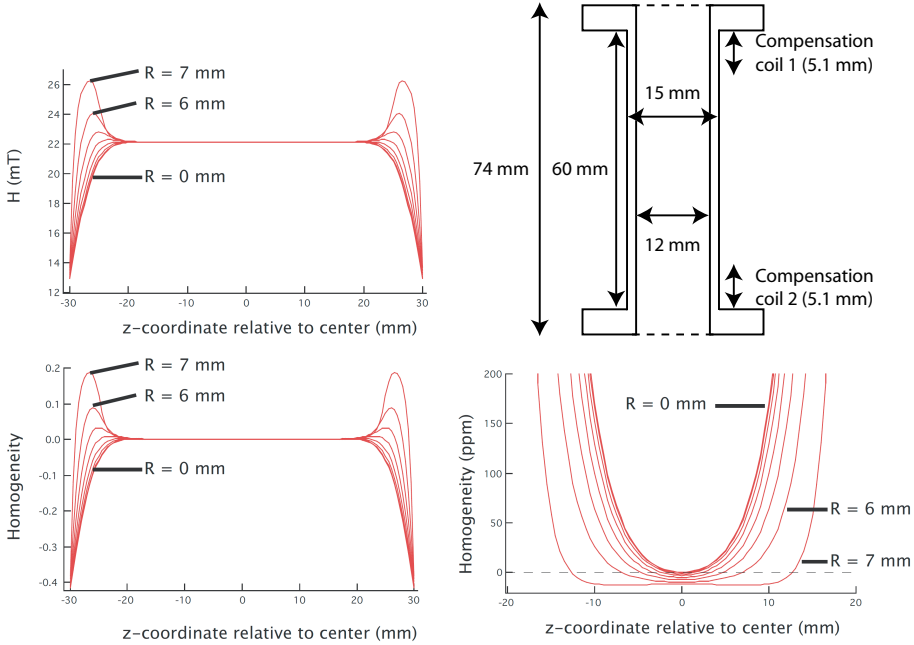


Figure 2.12: Simulated field profiles for the experimental magnet as designed.

relax back to the equilibrium position, hence aligning with respect to \mathbf{B}_0 . The spin-spin relaxation time T_2 is the typical time during which the spins move coherently¹¹ in the xy-plane ($\mathbf{B}_0 \parallel \hat{z}$), for which there is a net transverse magnetization. Both processes happen at the same time.

The term $\gamma^2 B_1^2 T_1 T_2$ is known as the saturation term and will decrease the susceptibility of the system (as the term approaches to one). While γ , T_1 and T_2 are inherent to the system, the B_1 should be chosen in such a way that it does not saturate the system.

If one adjusts the rf-field B_1 far from saturation, the width of the Lorentzian shaped absorption χ'' is determined by the T_2 of the sample (without saturation the $\text{FWHM} = 1/T_2$). In case of solids this T_2 is rather short, corresponding to a wide NMR signal. In the case of liquid ^3He the T_2 is relatively large ~ 1 s [50], which is good concerning the saturation and width of the NMR signal. However, an inhomogeneous magnetic field can also cause line broadening. The reason can be explained as follows: identical nuclei in a NMR sample are submitted to a slightly different magnetic field (inhomogeneity from the magnet). The resonance frequency for each individual nucleus is described by the equation: $\omega = \gamma B_0$. If the field varies

¹¹Or one can say the typical time of dephasing.

Layer	Number of windings
1 st layer	518
2 nd layer	518
3 th layer	515
4 th layer	517
Compensation 1	44
Compensation 2	44

Table 2.1: Windings of the Magnet.

over the NMR sample, so does the observed resonance frequency, broadening the NMR line. As the relaxation time of liquid ^3He is so long, the width of the NMR signal will be limited by the inhomogeneity of the magnet. The effective T_2^* of the system is then given by:

$$\frac{1}{T_2^*} = \frac{1}{T_2^{He^3}} + \frac{1}{T_2^{Magnet}}. \quad (2.12)$$

As the SNR in our system is rather small, because we measure at small volumes (especially in the part concerning the fibers), it is a necessity to reduce the inhomogeneity of the magnet as much as possible. We estimated, that with the spatial limitation of the experimental space, a magnetic field homogeneity of $\Delta H(\mathbf{r})/H \approx 10^{-5}$ in a cylinder ¹² of 5 mm long and a radius of 1 mm could be reached in the center of the magnet. After the example of existing superconducting magnets [51], we made calculations for magnets concerning our dimensions. Calculations were done with Magneeti [52], which took into account the dimensions of the holder, extensiveness of the wires, amount of layers, superconducting shield outside, superconducting foil in the inside, compensation coils, etc. The calculated field profiles are shown in figure 2.12.

The coil former, which is made of copper, is 15 mm in diameter and 60 mm long, as is illustrated in figure 2.12. The wire is a NbTi in CuNi matrix superconductor, which has in total 2156 turns shared over 4 layers and 2 compensation coils, see table 2.1. The compensation coils are positioned at the opposite ends of the magnet and are one layer only. The 4 layers and 2 compensation coils are wound with the same wire, which corresponded with a total length of 101.5 m. The resistance is $35 \Omega\text{m}^{-1}$, corresponding with a total resistance of 3.6 k Ω at room temperature. The magnetic field is 22 mT/A and is expected to have a homogeneity of $1 : 10^5$ in the center in a cylindrical volume of 5 mm long and a radius of 1 mm in the center of the magnet.

The magnet rests on the copper block of figure 2.1 with Vespel holders, and did not touch the experimental cell. Vespel is one of the best thermal insulators for low temperatures and the thermal conductivity $\kappa < 5 \cdot 10^{-8} \text{ W cm}^{-1} \text{ K}^{-1}$ [53]. In this way it was possible that the magnet itself was cooled by the mixing chamber and

¹²This volume, as we will see in the next section, is close to the sample space which fits inside the tank coil.

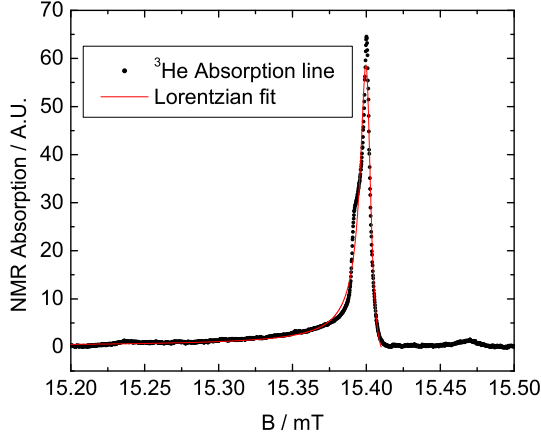


Figure 2.13: Typical absorption line of ^3He in the normal phase obtained with our magnet at the lower tank coil. Due to inhomogeneity in the magnet the data is fitted with a Lorentzian in polar coordinates. The fit shows an effective width of $8.3 \mu\text{T}$, which results in a field homogeneity of $\Delta H(\mathbf{r})/H = 5.38 \cdot 10^{-4}$ for the lower tank coil.

thermally decoupled from the nuclear stage. This thermal isolation prevents that the thermal oscillation in the copper coil holder, due to the sweeping of the magnetic field \mathbf{B}_0 ¹³, influences the temperature at the nuclear stage. The heat induced in the magnet is released to the mixing chamber, which is connected by copper braid.

As one can see from the overview of the cell in figure 2.1, the two tank coils are not positioned exactly in the center of the magnet. Consequently the inhomogeneity at that position should be worse than $\Delta H(\mathbf{r})/H \approx 10^{-5}$. The upper tank coil, as illustrated in figure 2.1, is positioned 0.5 cm from the center, while the lower tank coil is 2 cm off from the center of the magnet. The separation was necessary to be able to perform both measurements at the same time without interference from each other, see also next section. The inhomogeneity of the magnet will manifest itself in the NMR absorption spectrum of liquid ^3He in the normal phase, as measured by the pick-up coils. Such an NMR spectrum at 3 mK and zero pressure is plotted in figure 2.13 for the lower tank coil (which has the worst inhomogeneity of the two tank coils). Here the excitation of the rf-coil was optimized just before saturating the system. The absorption spectrum, see equation (2.11), should be Lorentzian shaped. However, if the inhomogeneity of the magnet determines the effective T_2^* the curve will become more asymmetric. The field away from the cylinders axis is higher than in the center, as illustrated in figure 2.14. If this magnetic field is slowly increasing, the ^3He at the surface of the cell will be in resonance first and ends with the ^3He in the center. To

¹³Eddy currents, etc.

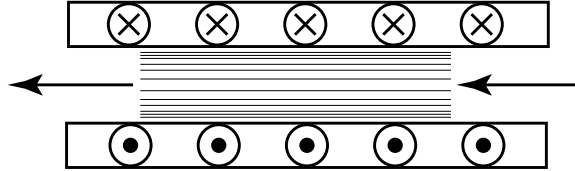


Figure 2.14: Sketch of magnetic field lines in the solenoid. The density of field lines is highest at the outside of the bore compared to the center. Field line profile is exaggerated.

take care of the spatial field distribution, and with cylindrical symmetry, we fitted the data with a Lorentzian in polar coordinates.

The measured field homogeneity of the lower tank coil was about $\Delta H(\mathbf{r})/H = 5.38 \cdot 10^{-4}$, mostly coming from the helium-3 inside the tank coil (cylinder of 4.4 mm long with a diameter of 1 mm) 2 cm off the center of the magnet. This result was better than we had calculated, as one can see in figure 2.12. We do not know if the use of superconducting wires for the tank coils made the field locally more homogenous, as the tank coils are relatively close to the ^3He sample¹⁴. The fitted NMR spectrum has some deviations compared to the Lorentzian. We assume that this is because of the Helmholtz configuration of the tank coils, see section 2.6, which means that deformation (due to the superconductor) may be different in the x- and y-direction¹⁵. Nevertheless, we are satisfied with the results and considered it good enough for NMR experiments.

¹⁴Mainly to increase the filling factor as much as possible, but also because of the limitation in space.

¹⁵The NMR spectrum would only be perfectly described by a Lorentzian in polar coordinates if the inhomogeneity of the field is cylindrical isotropic.

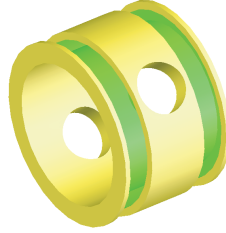


Figure 2.15: Tank Coil holder, Helmholtz configuration.

2.6 Tank Coil

For the design of the tank coil the following criteria were considered: Low dissipation, high as possible filling factor, reasonable homogeneity, induction should (together with capacitor) give the right resonance frequency (~ 500 kHz) and it should fit in the bore's magnet. The most suitable configuration was considered a Helmholtz configuration as illustrated in figure 2.15. The coil holder had a 2 mm hole in the middle, so it could be moved over the rod of PEI (see figure 2.1) to the desirable position, and was fixed between two rubber rings. The two circular coils are 2.4 mm separated from each other, and had a diameter of 4.4 mm (first layer was wound directly on the PEI). In total the coil had 120 windings, divided over 4 layers, of $65 \mu\text{m}$ diameter¹⁶ superconducting wire. The total inductance was $\sim 100 \mu\text{H}$ which gives (with parallel capacitor of 1 nF) the desirable resonance frequency f_0 of ~ 500.000 Hz.

The tank coil, including wiring, is slightly off from a perfect Helmholtz configuration. This was due to a compromise between: spatial dimensionality, total inductance, availability in diameters of the superconducting wires and limitations in winding. The inhomogeneity of the tank coil is not as important¹⁷ as in the case of the experimental magnet, and was not considered as a limitation.

Superconducting wire is used to reduce the dissipation in the tank coil as much as possible. We tested three commercially available superconductors of the same dimensions. Two pure superconductors Nb, Nb⁴⁷Ti and NbTi in CuNi matrix. The Q of the tank circuit¹⁸ was measured at 4 K, resulting in 5000, 4600, 3800 for Nb, NbTi and NbTi_CuNi, respectively. As expected the pure superconductors gave fewer losses in the system¹⁹. However, the resonance frequency shifts as function of magnetic field, generated by the experimental magnet \mathbf{B}_0 , see figure 2.16. The resonance frequency decreases, meaning that the inductance of the coil increases in magnetic field. Somehow the field lines do increase the permeability of the coil,

¹⁶This diameter is including the insulation (Formvar), the bare diameter is $50 \mu\text{m}$.

¹⁷At worst a second order effect.

¹⁸All tests were done in the same configuration.

¹⁹One does expect more losses in NbTi_CuNi due to possible eddy currents in the copper. However, the other superconductors still contain rf losses as well, mainly to dielectrics such as the wire insulation (Formvar) and the coil former.

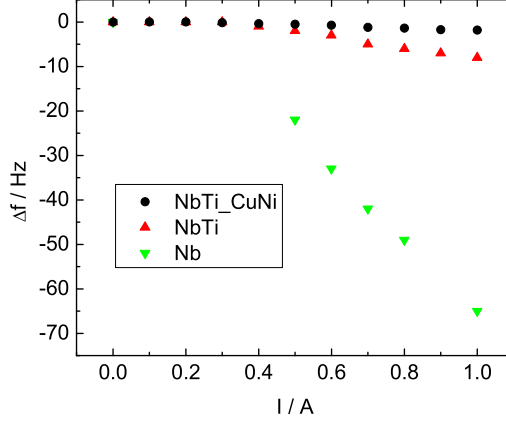


Figure 2.16: Shift of the resonance frequency (relative to zero field) as function of current through the experimental magnet, for tank coils wired with Nb, NbTi and NbTi-CuNi.

and seem to have more effect on the wires of the pure superconductor. For both superconductors the external applied magnetic field is lower than the first critical field H_{c1} (no vortices enter the superconductor), meaning that the entire field is repelled from the superconductor. However, the London penetration depth λ_L in Nb²⁰ metals is a couple of times shorter than in NbTi²¹ [54], so the field lines are repelled (bent) stronger in Nb. In case of NbTi in CuNi matrix the field lines can penetrate the matrix without problem, resulting in the least repulsion and bending of the field lines of all tested tank coils. It seems reasonable to conclude that the total effective repulsion does increase the permeability of the coil, but the mechanism of it is enigmatic.

In our cw-NMR method, where the frequency is fixed at the resonance frequency of the tank circuit and the B_0 is swept, has a disadvantage concerning the baseline. It is not a zero measurement, meaning the baseline is non-zero, but has the amplitude of the tank circuit as measured by the pick-up coil. This amplitude forms the baseline and in an ideal system would only change if one goes through the resonance with the ^3He atoms.

Despite the fact that the Q of the tank circuits hardly changes as function of current I (field \mathbf{B}_0) the baseline for cw-NMR does. If one sweeps the magnet (like in figure 2.13), and keeps the frequency fixed at the resonance frequency of the tank

²⁰ λ_L 39 nm at zero K [2].

²¹The exact differences depend on composition and purities, but values up to 10 times longer have been measured.

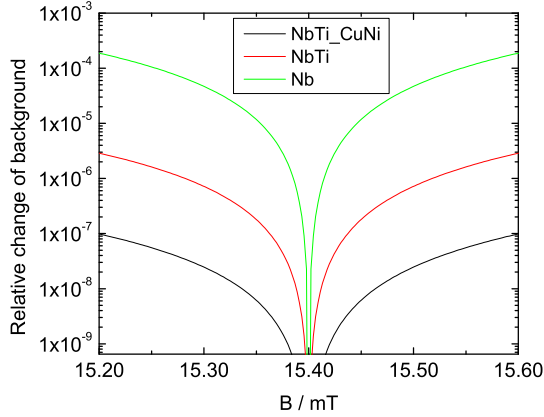


Figure 2.17: Simulation of relative change of the background due to the change of resonance frequency of the tank coil as function of external magnetic field. The frequency was fixed at 500.000 Hz, which is the resonance frequency of the tank circuit at 15.4 mT. Tank coils wound with Nb, NbTi and NbTi_CuNi wires are compared.

circuit, which is 500.000 Hz at 15.4 mT, the baseline changed as is plotted in figure 2.17. Within this sweep domain (typical sweep domain for ^3He) the baseline with the Nb wire changed more than 100 ppm. The smallest signals we expected to measure were estimated to be 100 ppm as well. So, despite of the higher Q with Nb it would not be convenient to use it for the NMR experiments. While at this temperature the pure NbTi wires would still fulfill the conditions, we expected it will not anymore at the lowest temperatures. The Q will increase by at least a factor of 3, and would then change the baseline comparable to 100 ppm. Leaving the NbTi in CuNi matrix the best candidate to measure these smallest signals at the lowest temperatures, for which we decided to wire the tank coils with NbTi in CuNi matrix.

2.6.1 Pick-up Coil

As described in section 2.4 the best SNR can be achieved by the weak coupling technique, meaning that a pick-up coil is attached to the tank coil. As explained, the optimal SNR is determined by the product of $k \sqrt{L_P/L_T}$. While L_T is the inductance of the tank coil (is fixed at 100 μH), we can tune L_P (inductance pick-up coil) and k for optimal result.

The wiring to room temperature for tank circuit 2 is made from phosphor bronze, and as simulated (see figure 2.4.3) the product $k \sqrt{L_P/L_T}$ should be around 0.17. By fixing the pick-up coil on one site of the tank coil, a coupling k of ~ 0.5 was achieved. From here the inductance of the pick-up coil was optimized and was close to 12.5 μH .

The total product gives 0.18, which is sufficiently close to the optimal product.

The wiring of tank circuit 1 could be made of copper wires. In section 2.4.4 the optimal read out for copper wires was calculated to be a direct one (coupling $k = 1$), but was simulated for the case that the R_C of the wires was 1Ω . However, to limit the heat input in the helium bath (and to the dilution fridge) smaller diameters were used, making the total resistance 4Ω ($R_C = 2$). In this case the optimized product ($k \sqrt{L_P/L_T}$) was calculated to be ~ 0.44 . Here the pick-up coil ²² was placed on both sides of the tank coil, which made the coupling a bit stronger and was estimated to be 0.7. The total inductance of this pick-up coil was $40 \mu\text{H}$, making the total product 0.44.

While the system was designed such that both tank coils could be read out simultaneously, the pick-up coils should not have interference with each other. To minimize this effect, the coils were put in a perpendicular position. Also the distance (2.5 cm) between the two was carefully chosen and as the Biot-Savart law says:

$$\mathbf{B}_1(\mathbf{r}) = \frac{\mu_0}{4\pi} \int_L \frac{d\mathbf{I} \times (\mathbf{r} - \mathbf{r}')}{(\mathbf{r} - \mathbf{r}')^3}, \quad (2.13)$$

the magnetic field drops as r^3 . In this configuration a fraction smaller than $5 \cdot 10^{-5}$ is expected to be seen from each other, which is sufficiently small not to have any hinder ²³. Also this configuration allows that both coils could be positioned close enough to the center of the experimental magnet, so that both have enough field homogeneity.

2.7 Baseline and Feedback system

The configuration of our chosen cw-NMR setup does provide us a high Q . However, as explained before, the frequency is fixed at the resonance frequency of the tank circuit, while the B_0 is swept. This has a disadvantage concerning the baseline. The amplitude of the tank circuit, as measured by the pick-up coil, is non-zero, and would in an ideal system only change if one goes through resonance of the ^3He . However, no system is ideal, and all effects which change the amplitude in the tank circuit are seen as a change in the baseline. In the previous section we already discussed the effect of the wires of the tank coil in an external magnetic field, and how to reduce this effect as much as possible. However, there are two other issues to be considered, which have great influence on the shape and change of the baseline.

The first one is the tail of the hydrogen signal. In figure 2.18 the NMR spectrum of both the hydrogen and ^3He signal are plotted. The hydrogen signal comes from the PEI and the epoxy. By a Lorentzian fit its T_2 is estimated to be $8 \mu\text{s}$, which is considered to be normal for hydrogen bounds in polymers at low temperatures. As

²²Total pick-up coil was separated in two parts, of course still connected, which were both placed on the other side of the tank coil.

²³The coil around the fibers has a filling factor of 1 % compared to the other coil. So, in the same circumstances the signal is here 100 times smaller, and one must be sure that the signal is not obscured by the other NMR experiment.

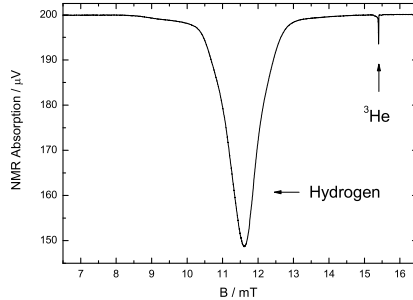


Figure 2.18: NMR Spectrum including both the signals of hydrogen and ^3He . The hydrogen is mostly coming from the PEI, but also from the epoxy (stycast 1266) used to fill the empty spaces between the fibers. The T_2 of hydrogen, obtained by fit, is approximately $8 \mu\text{s}$. The tail of the NMR signal of hydrogen is still visible in the ^3He .

the gyromagnetic ratios of hydrogen and ^3He are relatively close to each other (they differ a factor 1.31) and the width of the proton signal is relatively large (low T_2), one obtains a fraction of the hydrogen signal in the ^3He signal. This tail of hydrogen curves the baseline for the ^3He , which is especially noticeable if we try to measure small signals. As already explained in section 2.2, we could in principle replace the PEI with quartz glass, but due to technical difficulties and considerations of different configurations of the cell we decided to work with PEI. However, we did use as little PEI as possible to minimize the effect on the ^3He signal, so that we could subtract the hydrogen signal with a simple straight line. The advantage of a clear hydrogen signal in the spectrum is that one has a well-defined point²⁴ between frequency and magnetic field, which is helpful if one has to search for ^3He signals with $\text{SNR} \simeq 1$.

The second issue is the change of the resonance frequency of the tank circuit due to change of magnetic field and temperature. Using NbTi in CuNi matrix wires helped to reduce this effect significantly (compared to the other candidates), but it is still present. Change of the circuit resonance frequency has also been noticed at temperature sweeps, or when the temperature changes in the tank circuit if the excitation amplitude is adjusted. Also the sweep rate of the magnet (induction heating) has influence on the stability of the resonance frequency of the tank circuit.

Changes due to the magnetic sweep decrease the resonance frequency with increasing field and vice versa. The total frequency shift was only a few Hz per scan, but once one deals with a Q over 10.000 one Hz out of resonance changes the baseline over 40 ppm. This is for most ^3He experiments not problematic, but as we expected such

²⁴The magnetic field of the demag, and also the created circular current in the superconducting shield around the experimental magnet do create a stray field for the experiment. It results in a DC offset of the B_0 field, which value can be easily determined with the NMR signal of hydrogen.

small signals ²⁵ it will obscure our measurements. The temperature effects do change the properties of tank circuit a bit, and may take hours before it is in equilibrium. In general the shift due to temperature changes is slow, however after hours one can be out of resonance by 20-100 Hz.

These effects will undo the benefits of our high Q system (line with FWHM $\simeq 50$ Hz). This is definitely noticeable when the operating frequency is not modified to the proper resonance frequency over time. To obtain the best NMR spectrums of ^3He it is crucial to instantly adjust the operating frequency to the actual resonance frequency ($\omega_0 = 1/\sqrt{L_T C_T}$) of the tank circuit. If one scans through the resonance frequency of the tank circuit and reads the signal of the pick-up coils with a lock-in amplifier, we measure the impedance of the circuit as function of frequency. The complex impedance of the tank circuit, as in figure 2.3, is given by

$$Z = \frac{R_0 + ((1 - \omega^2 C_T L_T)\omega L_T - \omega C_T R_0^2)j}{(1 - \omega^2 C_T L_T)^2 + \omega^2 C_T^2 R_0^2}. \quad (2.14)$$

Using a 2-phase lock-in amplifier, we measure the Lorentzian shaped in-phase component

$$X = A \frac{R_0}{(1 - \omega^2 C_T L_T)^2 + \omega^2 C_T^2 R_0^2}, \quad (2.15)$$

and its Kamers-Kronig related quadrature component

$$Y = A \frac{(1 - \omega^2 C_T L_T)\omega L_T - \omega C_T R_0^2}{(1 - \omega^2 C_T L_T)^2 + \omega^2 C_T^2 R_0^2}, \quad (2.16)$$

where A depends on the excitation amplitude of the circuit ²⁶. It should not be surprising, as this is a resonance experiment like NMR, that the in-phase component X and quadrature component Y have the same behavior as the absorption χ'' and dispersion χ' terms of equation (2.11) and (2.10), respectively.

Both components and terms are Kramers-Kronig related, and do provide the same information of the system. This allows the use of one component for a feedback channel to compensate for the frequency shifts, see figure 2.19. As illustrated in figure 2.20(a) the Y component is zero in resonance ²⁷, and does behave linearly for values of 1 Hz (with an accuracy of 1 ‰) around the resonance frequency. By monitoring the Y component one can track the frequency shift.

To compensate for the shift of the resonance frequency of the tank circuit, due to the effects described in previous sections, one should keep the operating frequency

²⁵If we would divide the smallest expected absorption signal by its corresponding baseline, it is close to 100 ppm. As in these conditions the baseline changes already over 40 ppm, and the SNR is expected to be around one (see also section 2.8 for the noise) it is definitely hard to observe the absorption signal. Not to mention that the sensitivity of the measurement reduces as the resonance frequency of the tank circuit shifts away from our initially set (resonance) frequency.

²⁶Actually A is the excitation as measured by the pick-up coil.

²⁷Technically if Y is fixed at zero than, for our used parameters, X is 0.004 Hz removed from the maximum of the top. The relative change of the amplitude of is than $5 \cdot 10^{-9}$, which it is not considered to be a problem.

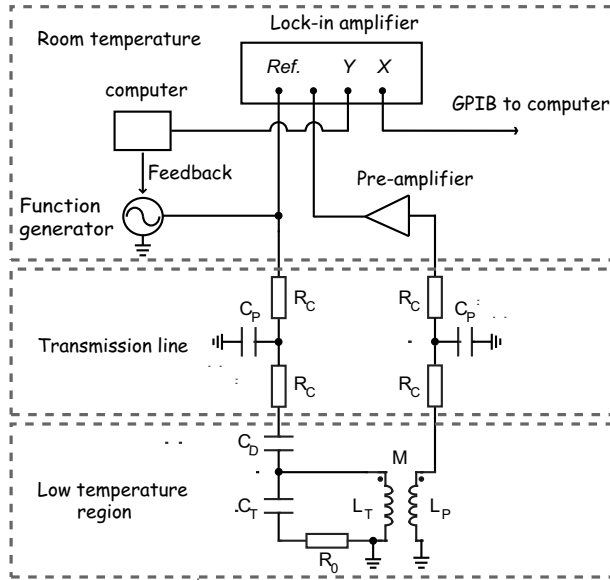


Figure 2.19: Scheme of the circuit including the feedback loop. Initially the frequency of the function generator is matched with the resonance frequency of the tank circuit. The signal generated, due to mutual induction, in the pick-up coil is sent to the lock-in, where it is compared with the reference signal of the function generator. The X component is directly stored in the database of the measurement computer. The feedback controls the frequency of the function generator, which is all times adjusting the operating frequency so that $Y = 0$ and equals the resonance frequency of the tank circuit.

at the resonance frequency of the tank circuit. Any frequency shift will change the absolute value of $|Y|$ from zero²⁸. To stay in resonance, the operating frequency is changed till the $|Y|$ component is zero, for which one knows to be at the resonance frequency of the tank circuit again. The sign of the Y component provides the direction of compensation, while the absolute value²⁹ determines the change Δf of the operating frequency. This frequency adjustment was done continuously with a refresh time of 50 ms. The adjustment rates are listed in table 2.2, which are realized taking the following into account: excitation values³⁰, slope of Y around the resonance frequency (is determined by the Q of tank circuit), sweep time of the NMR scan, resolution of the lock-in amplifier, and the changes of baseline due to magnetic and or temperature effects.

As the smallest expected signals are around $1 \cdot 10^{-4}$ relative to the baseline³¹, we

²⁸If starts with the resonance frequency of the tank circuit.

²⁹This is the value as measured by the pick-up coil.

³⁰The maximal excitation (without saturation effects) is used.

³¹If we would divide the smallest expected absorption signal by its corresponding baseline, it is

$ Y / \mu\text{V}$	$\Delta f / \text{Hz}$
< 100	$5 \cdot 10^{-1}$
< 10	$5 \cdot 10^{-2}$
< 1	$5 \cdot 10^{-3}$
< 0.1	$5 \cdot 10^{-4}$
< 0.01	0

Table 2.2: The frequency shift Δf for value of $|Y|$. $|Y|$ is as measured by the pick-cup coil.

aimed that the feedback should refresh the frequency in such way, that the relative change of the baseline (due to external effects) is not more than $1 \cdot 10^{-5}$, which corresponds to a maximum deviation of ~ 0.025 Hz from the circuit resonance frequency (with Q of 10.000).

Testing this feedback system with an empty cell ³², we indeed get a stability for periods much longer than our planned sweep times. It could keep the Y component at zero with an accuracy of the noise of the system. The noise level, which will be discussed in detail in section 2.8, is typically 20 – 40 nV (with a bandwidth of 2.6 Hz). Meaning that when the system is in equilibrium, the operating frequency is adjusted to with $5 \sim 10^{-4}$ Hz around the resonance frequency. This means that theoretically (if Q is 10.000) the maximal relative change of the baseline is only 2 ppb, of course the noise will be here the limitation.

While this feedback mechanism is able to keep the operating frequency with high accuracy at the resonance frequency of the tank circuit, there could be a discrepancy in the absorption peaks (obtained by NMR measurements) compared to the 'normally' expected Lorentzian shaped absorption spectra without feedback. So, we will now consider the effects of the feedback on the NMR line shape in various conditions.

First of all, as the Y component is fixed at zero, we have to drop the dispersion χ' relation. However, as it is Kramers-Kronig related with the absorption χ'' , it is not considered as losing information of our system. Secondly, the change of susceptibility (by the NMR experiment) does change the total inductance of the coil.

$$L_T = L_0[1 + 4\pi q\chi(\omega)] = L_0[1 + 4\pi q(\chi'(\omega) - j\chi''(\omega))], \quad (2.17)$$

where q is the filling factor of the system. The change of the inductance of the tank coil will change the properties of the tank circuit. The absorption term χ'' modifies the dissipative part of the impedance, and by that the total losses in the tank circuit. The dispersion term χ' does change the resonance frequency. The in-phase component

estimated to be close to 100 ppm.

³²This test was to see how good the operating frequency could stay at the resonance frequency of the tank circuit, as we sweep the magnetic field and temperature. Effects of the feedback system at the NMR absorption peaks were not yet considered/tested here (as it is performed with an empty cell). This will be discussed in detail in the following paragraphs.

of the tank circuit (equation (2.15)), including the NMR effects (equation (2.17)), will change to

$$X = A \frac{L_0 \omega 4\pi q \chi'' + R_0}{(1 - \omega^2 C_T L_0 (1 + 4\pi q \chi'))^2 + (\omega^2 C_T L_0 4\pi q \chi'' + \omega C_T R_0)^2}, \quad (2.18)$$

If the absorption and dispersion terms are sufficiently small, so that the resonance frequency and/or the width of equation (2.18) hardly changes compared to the initial properties (without sample) of the tank circuit, we will measure a fractional change of resistance as given by equation (2.3)³³. If the susceptibility is significantly large, we will expect deformations in the Lorentzian shaped NMR absorption peak. In general the deformation is due to the combination of the Q (width) of the LC-circuit, the filling factor q , and the spin-spin relaxation time T_2 of the sample.

To have a better understanding of how this will influence our absorption spectra we have simulated our system. The used parameters are: The effective T_2^* determined by the (in)homogeneity our magnet, the susceptibility $\chi_0 \approx 3.81 \cdot 10^{-8}$ [55] of ^3He at zero pressure, the tank capacitor C_T of 1 nF, and the tank coil inductance L_0 of 100 μH . The filling factor q was varied between 0.01, 0.1 and 1. Also the Q of the tank circuit (without sample) was varied: $1 \cdot 10^2$, $1 \cdot 10^3$, $1 \cdot 10^4$, $1 \cdot 10^5$ and $1 \cdot 10^6$.

The simulations are done with and without feedback. Without feedback, the system is kept at the resonance frequency $\omega_0 = 1/\sqrt{L_0 C_T}$ of the LC-circuit (without sample). Including feedback, the system is adjusted instantly to the new resonance frequency, hence $\omega_0 = 1/\sqrt{L_0(1 + 4\pi q \chi')C_T}$, necessary adjusting times are neglected³⁴. In the simulation the magnet is swept with constant speed, but as the resonance frequency changed, the relative difference between the magnetic field³⁵ and the resonance frequency did not change linearly anymore, for which corrections in the simulation are included.

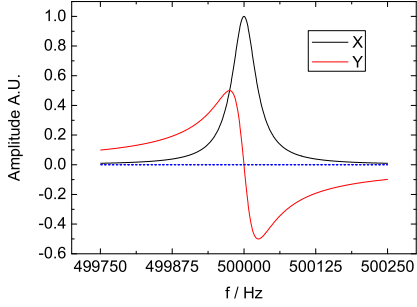
The simulated absorption spectra are plotted in figure 2.20(b), 2.20(c) and 2.20(d). We did not consider the absolute amplitude here, as it should be clear that it is proportional with qQA at resonance.

The simulations show for relatively small quality factors Q and filling factors q an absorption spectrum as expected according to equation (2.11) (without saturation term). For low Q and q the effective values of χ' and χ'' are (relatively) small compared to the width and the resonance frequency of the tank circuit, and will hardly deform the expected Lorentzian line shape. This change as the Q and/or q increases. Then the dynamic susceptibility does change the properties of the tank circuit significantly, and thus the absorption spectra. In first instance the black lines show more deformation (they get wider), an effect which is delayed in the case with feedback (red lines) as we keep the nominator of equation (2.18) smaller during the sweep. The widening is a reflection of decreasing the Q factor of the tank circuit, however one should realize that at resonance the amplitude is still proportional with the initial Q (tank circuit

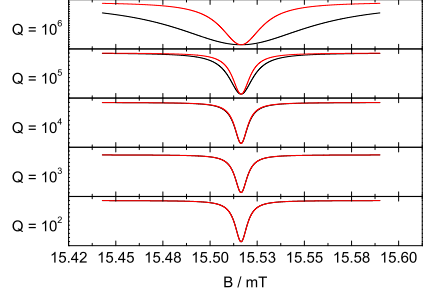
³³This is the case for most NMR experiments.

³⁴This is valid as the feedback is much faster than the scan rates.

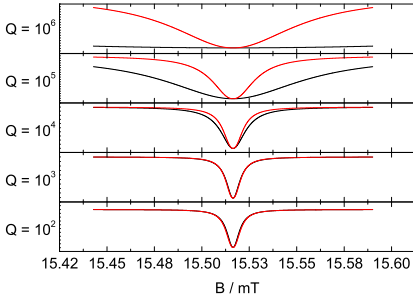
³⁵To compare the magnetic field to a frequency it is multiplied with the gyromagnetic ratio of ^3He , hence $\omega = \gamma | \mathbf{B}_0 |$.



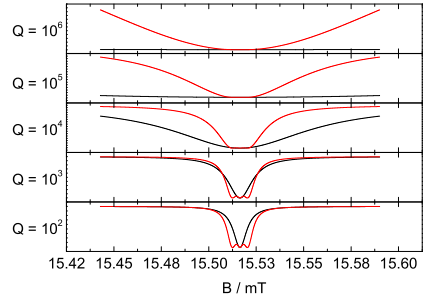
(a) In-phase component X and quadrature component Y as one scan through resonance of the tank circuit. The blue line indicated the zero of the y-axis.



(b) Simulated absorption spectrum with a filling factor q of 0.01. The black lines correspond with simulation where the operating frequency is kept fixed, $\omega_0 = 1/\sqrt{L_0 C_T}$. Red lines correspond with simulations including the feedback.



(c) Simulated absorption spectrum with a filling factor q of 0.1. The black lines correspond with simulation where the operating frequency is kept fixed, $\omega_0 = 1/\sqrt{L_0 C_T}$. Red lines correspond with simulations including the feedback.



(d) Simulated absorption spectrum with a filling factor q of 1. The black lines correspond with simulation where the operating frequency is kept fixed, $\omega_0 = 1/\sqrt{L_0 C_T}$. Red lines correspond with simulations including the feedback.

Figure 2.20:

without sample). As the amplitude is equal with or without feedback system, it is

beneficial to have the feedback system ³⁶ as a smaller line width allows a reduction of the total sweep.

If the dynamic susceptibility becomes (relatively) big, or in case of our simulations the filling factor q is close to one, the feedback makes the spectrum less Lorentzian. The adjustment of the resonance frequency becomes too strong and flattens out the absorption spectrum near resonance. In that case (at least for the lower Q regime), it may be preferable to work without feedback.

In general one should know χ_0 , q , T_2 and Q of the system to determine if the feedback will improve (or not) the absorption spectrum. In our case the Q of the system is around 10.000 and the filling factor q is estimated to be 0.01. This corresponds with the middle graph of figure 2.20(b). Here the feedback induces no significant differences in the NMR line shape.

It is nice to see, that our simulations showed that in some circumstances the feedback will even improve the NMR spectra. However, the reason for us to use any feedback was to compensate for the shifts of the resonance frequency (of the tank circuit). Important to know was: does the feedback harm the NMR measurements? As shown by the simulations ³⁷ (for parameters concerning our system) the feedback hardly influenced the absorption spectrum. Realizing that in practice the frequency shifts in an uncontrolled way due to magnet or temperature effects, it is certain that much better absorption spectra will be obtained including the feedback.

2.8 Noise

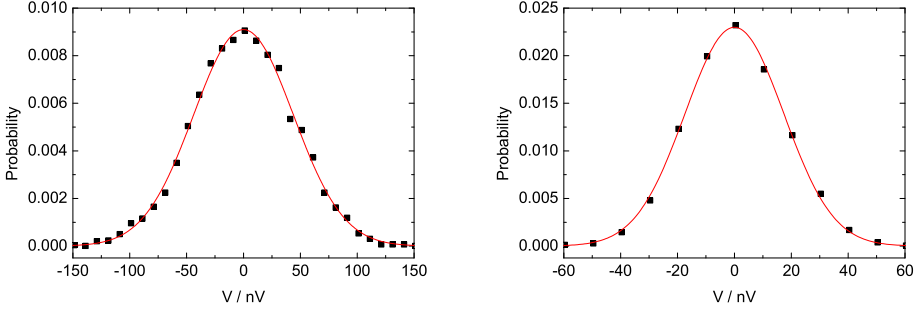
In general it can be quite complex to point out where the most significant noise sources of the electronic circuit are located. While there is white or wide-band noise, it is advantageous that we use high Q LC-circuits. The resonance frequencies are around 491800 Hz and 488000 Hz with a Q of 10700 and 15200, respectively. Not only is the high Q good for our NMR experiments, it is also good to filter out frequencies far from the resonance frequency. More over the signal from the pick-up coils is measured with a lock-in, which adds an extra filter.

The main differences between the two tank circuits are the coupling of the tank coil with the pick-up coil, the inductance of the pick-up coil and the wiring (through the helium bath) to room temperature. The wiring through the helium bath of the pick-up coil of tank circuit 1 was made of copper wires, the pick-up coil of tank circuit 2 had phosphor bronze wires ³⁸. As the copper wires have lower resistivity, the pick-up coil is coupled stronger, as described in section 2.4, and has a total Q of ~ 10.000 for

³⁶Maybe an exception is if one deals with resolution difficulties, then one may prefer a bit wider spectrum.

³⁷In the simulations the baseline was considered to be stable, and not changed by any external effect.

³⁸Preferably the wires should have as low resistivity as possible. However, that coincides with good thermal conductivity. To prevent too much heat input in the helium bath and cryostat, the amount of copper wires in the cryostat are limited. Phosphor bronze wires are good thermal insulators, but will increase the total resistivity of wiring by approximately 1 order of magnitude.



(a) Noise as measured at the lowest temperatures for tank circuit 1 in resonance with a bandwidth of 2.6 Hz. The noise is fitted with a Gaussian (red line) and has a standard deviation σ of 43.85 nV. The noise is independent of its mean μ (here put to zero).

(b) Noise as measured at the lowest temperatures for tank circuit 2 in resonance with a bandwidth of 2.6 Hz. The noise is fitted with a Gaussian (red line) and has a standard deviation σ of 17.15 nV. The noise is independent of its mean μ (here put to zero).

Figure 2.21:

which the SNR is believed to be optimized. Optimizing tank circuit 2 (with phosphor bronze wiring) gave us a Q of 15000.

Typically measurements with our tank circuits at the lowest temperatures have a noise behavior at resonance as plotted in figure 2.21(a) and 2.21(b). Here the $\Delta V/\sqrt{\text{Hz}}$ is 27.2 nV/ $\sqrt{\text{Hz}}$ and 10.6 nV/ $\sqrt{\text{Hz}}$ for tank circuit 1 and 2, respectively. Off-resonance the noise is for both circuits about 4.8 nV/ $\sqrt{\text{Hz}}$, this is typically the noise generated by the commercial pre-amplifier (Stanford Research Systems Model SR560). The extra noise at resonance for the circuit is then 26.8 nV/ $\sqrt{\text{Hz}}$ and 9.45 nV/ $\sqrt{\text{Hz}}$, respectively. This noise is generated in the circuitry and to compare the ratio between them, $\Delta V_1/\Delta V_2 \approx 2.84$, we can reconstruct the origin of the dominant noise source.

If the noise would be mostly coming from the wiring of the pick-up coils to room temperature, then the ratio difference should be around $\sqrt{56/4.4} \sim 3.57$ (ratio between the resistance of phosphor bronze and copper wires). This ratio is too high to be the dominant noise source ³⁹.

The circuitry before the decoupling capacitor is for both tank circuits identical,

³⁹At least if the thermal noise is the dominating source; if other spurious signals are picked up we would have expected a ratio close to one.

meaning that the ratio of the noises generated over there should be equal to

$$\frac{|H(\omega_{01})| \cdot k_1 \sqrt{L_{P_1}/L_{T_1}}}{|H(\omega_{02})| \cdot k_2 \sqrt{L_{P_2}/L_{T_2}}} \approx \frac{1}{1.5} \frac{0.70}{0.5} \sqrt{\frac{40}{12.5}} = 1.67. \quad (2.19)$$

This ratio is too small to be the dominant noise source of the system.

The thermal noise (Johnson-Nyquist noise) V_n generated in the tank circuit is given by

$$V_n = \sqrt{4k_B T \Delta f R_0}. \quad (2.20)$$

At resonance, the noise over the tank coil equals $Q \cdot V_n$. So, at 1 mK and a bandwidth Δf of ~ 2.6 Hz, the noise in the tank circuit should be 0.43 nV/ $\sqrt{\text{Hz}}$ and 0.52 nV/ $\sqrt{\text{Hz}}$ for the tank circuits, respectively. This is significantly lower ⁴⁰ than measured with the pick-up coils, but due to the coupling a fraction of the losses in the tank circuit is at higher temperatures. The total losses in the tank capacitor and tank coil are expected ⁴¹ to be ~ 0.015 Ω , meaning that the tank circuit 'sees' 0.015 Ω and 0.005 Ω from the wiring to room temperature, respectively. These wires go from 4 K to room temperature, and it is not trivial to determine the temperature of each segment. But if we assume that the resistance increases linearly with its length and the temperature gradient is constant between the maximal level of the liquid helium to room temperature, we estimate an effective temperature of 25 K. Using these parameters we find a noise voltage in the tank coil 1 of

$$Q \sqrt{4k_B T R_0} / \sqrt{\text{Hz}} = 10000 \sqrt{4 \cdot k_B \cdot 25 \cdot 0.015} / \sqrt{\text{Hz}} \approx 46 \text{ nV} / \sqrt{\text{Hz}}, \quad (2.21)$$

and in tank coil 2,

$$Q \sqrt{4k_B T R_0} / \sqrt{\text{Hz}} = 15000 \sqrt{4 \cdot k_B \cdot 25 \cdot 0.005} / \sqrt{\text{Hz}} \approx 40 \text{ nV} / \sqrt{\text{Hz}}. \quad (2.22)$$

Measured with the pick-up coil these signal should correspond ⁴² to 20.2 nV/ $\sqrt{\text{Hz}}$ and 6.8 nV/ $\sqrt{\text{Hz}}$, respectively. These calculated values are off by 30% compared to real noise measurements, which is quite good as it is hard to estimate certain details (like the effective temperature). But more important their ratio is 2.97, which is only off by 5%. So it seems that this is the most dominant noise source of our setup. Another way to look at it, is that the product of the fraction R_0 'seen' by the tank circuit times its Q is more than the actual resistance of the wires to room temperature, and so is its total thermal noise.

Other noise sources like phase noise, noise pick-up from the environment or noise generated by the function generator seem not to be of great influence. Even if one sweeps the magnetic field \mathbf{B}_0 , the noise level seem to be unchanged, with the exception that the baseline changes as discussed in the previous section.

⁴⁰In reality the electron temperature should be higher due to the bad electron-phonon interaction at low temperatures. However, even in the case that the electrons have a temperature of 50 – 100 mK the noise should still be much lower than measured.

⁴¹Actually it is measured in a previous cool down. For a circuit who was minimal coupled ($k < 0.01$), the Q was around ~ 20000 . Due to the low coupling the losses elsewhere can be neglected.

⁴²Signal is multiplied with the corresponding factor of $k \sqrt{L_P/L_T}$.

In the case of similar Q and in optimal conditions⁴³ low temperature pre-amplifiers [39] can give an order of magnitude lower noise voltage. However, in practice, due to interference effects, their noise level equals ours. As our system is built from passive elements, it has practical advantages. Not only do we avoid additional energy dissipation in the cryostat⁴⁴, active elements always have the downside of reliability and stability.

The optimization of the system is a long and complex iteration, and we still believe it can be improved more. The system is initially optimized according to equation (2.8), with the assumption that the thermal noise in the tank circuit could be neglected and the dominant noise was coming from the (thermal) noise generated in the transmission lines. As it seems now, we can improve the SNR to decouple the tank circuit a bit more, the Q will go up and the noise level drops. As the noise of the pre-amplifier is already visible not much improvement could be made from this stage, because it would be the next limiting factor. Better pre-amplifiers can be built and in combination with the reduction of the parasitic capacitance in the transmission lines, one order of magnitude in the SNR should be relatively easy to reach within this configuration.

The only method of significantly improving the SNR ratio would be with the help of SQUID amplifiers. One can use the same LC-circuit, but instead of reading out with the pick-up coil, it is done by a SQUID. If this SQUID noise (including the feedback electronics) is much lower than the noise generated in the LC-circuit, then the ultimate SNR ratio of $\sim Q/\sqrt{Q} \propto \sqrt{R_0}/R_0$ can be achieved with an effective thermal temperature as low the electrons can be cooled. If one assumes that the electrons can be cooled to 50 mK, a 20 times better SNR could be achieved. However, one has then an active system including its difficulties. The constantly changing stray fields in the cryostat can make it hard to work with stable SQUID amplifiers. Also the preparation time for an optimal SQUID system with operating frequencies of 500 kHz is very time consuming. While it is clear that SQUID's in theory are more advantageous, in practice it is very hard to have a completely stable setting during the very long continuous measurements. This was not a problem for the weakly coupled transformer, which was very reliable during continuous measurements for days.

2.9 Conclusion

We managed to construct a cell to do our NMR experiments, for which any cooling obstacles were minimized. Despite the space limitations a reasonably homogeneous experimental magnet is constructed to perform these NMR experiments. As the restricted geometry measurements coincide with small filling factors, weakly coupled transformer techniques were simulated and built to obtain sufficient SNR. The wiring of tank coils was carefully chosen, and together with a feedback loop, baseline defor-

⁴³Perfect impedance match between amplifier and tank circuit. Noise is mainly dominated by the input noise of the preamplifier.

⁴⁴low pre-amplifiers are positioned at the 4 K stage, and can dissipate power up to 50 mW.

mation could be minimized. The SNR for the smallest expected signals is estimated to be 5, for integration times (bandwidth) matching our desirable sweep rates.

Chapter 3

Spin waves in cylinder of 1 mm in diameter

3.1 Spin waves

Spin waves refer to a collective excitation of spins in a system, for example electron spins in a lattice. In analogy with lattice vibrations or phonons, which are collective excitations of atomic positions in a lattice. Quantum mechanically one can speak about magnons, which are then the quantized spin waves. In the case of ^3He , NMR is the ideal technique to detect such spin waves, but the measured signal is the integrated magnetization of the spins of ^3He , which will average to zero ¹. However, standing spin waves will give a detectable signal. One way to create standing spin waves is to apply an inhomogeneous magnetic field, which allows even the detection of spin waves in the normal phase of ^3He [56]. In the superfluid phases the inhomogeneity of the texture allows the existence of standing waves as well. Here the spin waves are the Goldstone modes associated with the spontaneously broken rotational symmetry in spin space ².

The bulk isotropic superfluid B-phase of ^3He is not suitable to form standing spin waves measurable with conventional NMR techniques, since the $\hat{\mathbf{n}}$ -vector has no preferred orientation, causing the integrated magnetization to average to zero. However, walls and magnetic fields will introduce a preferred orientation for the $\hat{\mathbf{n}}$ -vector, which is explained in detail in section 3.3.

In confined geometries including magnetic fields the orientation of the $\hat{\mathbf{n}}$ -vector will be locally different, which results in the bending of the $\hat{\mathbf{n}}$ -vector over the sample. This bending occurs over a typical distance of the magnetic healing length ξ_H , which is

¹Technically one can measure a net magnetization if the NMR coils are of the same dimension as the wavelength of the system, which is normally not the case.

²In the case of ^3He -B the relative broken spin-orbit symmetry.

a few millimeters long [57] [58]. If the superfluid B-phase is formed in such geometry, with at least one dimension close to the magnetic healing length, it will create a texture which may act as a potential for standing spin waves. These spin waves can be detected by transverse NMR experiments, and are observed as satellite peaks in the absorption spectrum.

The very first experiment which observed spin waves in the superfluid B-phase was performed by Osherhoff, see for example [59]. He used a slab geometry (separations of the plates was $L \leq \xi_H$) and a magnetic field \mathbf{B}_0 parallel to the plates. The transverse NMR experiment found a more or less constant separation of the spin wave modes (NMR resonances), of which the intensities dropped as function of k^{-1} (k is the spin wave mode). This was in good agreement (at least to first order) with the solutions of the differential equation for this geometry [60] [61], see also section 3.5. It was seen as the proof of the existence and possibility of spin waves in the superfluid B-phase.

Another convenient geometry to create spin waves is a cylinder with a radius of few times the magnetic healing length. The cylindrical symmetry makes it relatively easy to calculate the allowed textures and spin waves, see sections 3.4 and 3.5. One of the first transverse spin wave experiments in a cylindrical geometry was performed by Hakonen *et al.* [62]. The experiment also showed a nearly equal separation between the spin wave modes, of which the intensity decreased as a function of k . These experiments could be explained by numerical calculations of Jacobsen and Smith [63].

The cylindrical geometries were also convenient to study vortices in the superfluid B-phase. Consequently several groups build rotating nuclear refrigerators to study this phenomena [64] [65] [66] [67] [68] [69]. Vortices affect the $\hat{\mathbf{n}}$ -vector mainly through a change in the magnetic orientation energy, which results in a different textural configuration compared to the non-rotational situation [70]. The effects show up in the experiments by a change of intensity and spacing of the spin waves. In this way an interesting discontinuity in the spin wave resonant frequencies was observed [58] [62], which marks a transition between the two different vortex states in the B-phase.

Our interest concerns the non-rotating cylinder experiment. We are interested in the textural configuration in the cylinder, which should be revealed by the spin waves. The magnetic healing length decreases as a function of temperature, and with a sufficiently small container radius one expects a textural transition. However, we found that the $\hat{\mathbf{n}}$ -texture formed a metastable configuration, which is unchanged to the lowest temperature. Not only did this metastable texture create a temperature independent potential for the spin waves, but the form of the potential is close to a quadratic function. This makes the potential interesting for two reasons. First, it is pressure and temperature independent, which is different from the situation in earlier spin wave experiments. However, modifying the pressure will still change the dipole coherence length of the superfluid, which will increase (or decrease) the amount of spin wave modes in the container. Meaning that we can now study this effect in the same energy 'landscape'. Secondly, the differential equation describing this geometry is analytically solvable for a quadratic potential, and allows us to explain the

absorption intensities of the spin wave modes. This is a unique phenomenon in the superfluid B-phase spin wave experiments.

The theory and the experiments of the spin waves in the metastable texture are described in this chapter. Also the experiments with the textural transition to the expected uniform texture is included in this chapter. From that experiment we conclude that the metastable texture could be realized if its growing speed is sufficiently slow.

3.2 Transverse NMR in $^3\text{He-B}$

Normally, in the absence of magnetic field, the spin orientation in a sample is isotropic. In that case, when cw-NMR is applied, there is resonance at the Larmor frequency as described in section 2.4. However, the order parameter of ^3He can be anisotropic (including the spin orientation), which induces a shift in the resonance frequency compared to the Larmor frequency. In cw-NMR experiments a shift in the resonance frequency will occur when a transverse oscillation Ω_\perp of the spins contributes to the (transverse) oscillation of the rf-field from \mathbf{B}_1 . The new transverse resonant frequency ω_0 will then be

$$\omega_0^2 = \omega_L^2 + \Omega_\perp^2. \quad (3.1)$$

As already mentioned before, the dipole energy (despite the fact that it is small by itself) has strong influence on the orientation of the order parameter, and thus on the frequency shift. From the Hamiltonian describing the spin orientation of the system,

$$H_S = \frac{1}{2}\gamma^2\mathbf{S}\boldsymbol{\chi}^{-1}\mathbf{S} - \gamma\mathbf{S} \cdot \mathbf{H} + H_D, \quad (3.2)$$

where $\boldsymbol{\chi}$ is the susceptibility tensor, the spin dynamics in the superfluid can be derived [21], [71], [72]. From here the oscillator frequencies can be obtained. In the linear regime, meaning small deviations from the equilibrium values (spatially homogenous conditions), the oscillator frequencies get the form of

$$\Omega_{\mu\nu}^2 = \frac{\gamma^2}{\chi} \frac{\partial^2 f_D}{\partial\theta_\mu\partial\theta_\nu}. \quad (3.3)$$

If one would apply the dipole energy of the (zero field) B-phase (1.23) to this equation one would not expect a transverse component, since the orientation of the $\hat{\mathbf{n}}$ -vector is isotropic. However, if we take the limit for the magnetic field $H \rightarrow 0$, keeping $\hat{\mathbf{n}}$ parallel to the magnetic field \mathbf{H} , equation (1.23) changes into

$$F_D^B = \frac{8}{5}g_D(T) \left(\cos\theta_z + \frac{1}{4} \right)^2 + \text{const}. \quad (3.4)$$

From equation (3.3) and by putting $\theta_z = \theta_L$ we get:

$$\Omega_{xx} = \Omega_{yy} = 0, \quad (3.5)$$

$$\Omega_{zz}^2 = 3\frac{\gamma^2}{\chi_B}g_D(T) \equiv \Omega_B^2. \quad (3.6)$$

As expected, the B-phase does not have transverse frequency components, but it has a longitudinal one. This would not be observed in a transverse cw-NMR experiment, but can be seen in longitudinal cw-NMR experiment, hence with the rf-field \mathbf{B}_1 parallel with \mathbf{B}_0 . These longitudinal resonances have been observed experimentally [73], [36].

In the B_2 -phase one would expect, due to preferred orientation of the $\hat{\mathbf{n}}$ -vector, a transverse frequency shift from the Larmor frequency. Using the relations (1.24) and (1.28) with (3.3) and including only small deviations around equilibrium, one obtains the transverse components [21]

$$\Omega_{xx}^2 = \Omega_{yy}^2 = \frac{2}{5} \lambda_D N_F \gamma^2 \chi^{-1} (\Delta_{\perp}^2 - \Delta_{\parallel}^2). \quad (3.7)$$

It implies two elliptical polarization modes with frequencies:

$$\omega^2 = \frac{1}{2} \omega_L^2 + \Omega_{xx} \pm \frac{1}{2} \omega_L \sqrt{(\omega_L^2 + 4\Omega_{xx}^2)}. \quad (3.8)$$

Because we do low-frequency NMR in our experiments the difference in population ($\Delta_{\perp}^2 - \Delta_{\parallel}^2$) is rather small. The transfer shift due to the orientation effects in the B_2 -phase can be neglected, especially because there is a much more dominating effect on the transverse shift.

If one studies NMR in restricted geometries like cylinders, slabs, aerogel or powders, surface effects play a dominating role on the orientation of the order parameter $\hat{\mathbf{n}}$, see section 3.3. The $\hat{\mathbf{n}}$ -vector will orientate from equilibrium $\hat{\mathbf{n}} \parallel \mathbf{H}$ to the normal of the surface. This transverse shift ω_0 can be expressed in the longitudinal resonance frequency of the B-phase (see equation (3.6)) and the angle β , which is the angle between the $\hat{\mathbf{n}}$ -vector and the (external) applied magnetic field [74]:

$$\omega_0^2 = \frac{1}{2} (\omega_L^2 + \Omega_B^2) + \sqrt{\frac{1}{4} (\omega_L^2 + \Omega_B^2)^2 - \omega_L^2 \Omega_B^2 \cos^2 \beta}. \quad (3.9)$$

The angle β is a function of position in the cell, so the total NMR spectrum from the ^3He fluid, if we neglect field inhomogeneity and relaxation times, is then given by the line shape function

$$f(\omega) = \int_V d^3\mathbf{r} \delta[\omega - \omega_0(\mathbf{r})]. \quad (3.10)$$

3.3 Orientation of the $\hat{\mathbf{n}}$ -vector due to bulk and surface effects

The orientation of the $\hat{\mathbf{n}}$ -vector is determined by effects in the bulk liquid and by the surface of the sample. The two most important orientation energies in the bulk are: The bulk-field free energy F_{BH} and the bulk-bending free energy F_{BB} .

The bulk-field free energy F_{BH} equals the $\hat{\mathbf{n}} \cdot \mathbf{H}$ dependency of the dipole energy density (1.24) to lowest order. Higher orders are not needed, because they hardly give any contribution to the bulk-field free energy.

$$F_{BH} = -a \int d^3r (\hat{\mathbf{n}} \cdot \mathbf{H})^2. \quad (3.11)$$

The term $(\hat{\mathbf{n}} \cdot \mathbf{H})^2$ is described by Leggett [21] as a combination of the depairing effects of the magnetic field and the dipole energy. The coupling strength a , in the case of $^3\text{He-B}$, is estimated to be $|a| \sim 4 \cdot 10^{-12} \text{ erg cm}^{-3} \text{ G}^{-2}$ [55], [22], [75]. The magnetic field in the bulk will try to orientate $\hat{\mathbf{n}}$ in the same direction, for which the energy is minimized.

The $\hat{\mathbf{n}}$ -vector is oriented by local conditions, however the change of this orientation can only be continuous. Fast changes (discontinuities) of the order parameter will be energetically unfavorable. It means that all spatial variations should be smoothed (out) over a finite distance, which is accomplished if F_{BB} is expressed as an invariant combination of the gradients of the order parameter [76], [60]. Basically, the bulk-bending free energy is obtained by integrating the bending free energy density (1.35) over the whole volume.

$$F_{BB} = \frac{c}{13} \int d^3r \{ 16(\hat{\mathbf{n}} \times (\nabla \times \hat{\mathbf{n}}))^2 + 13(\nabla \cdot \hat{\mathbf{n}})^2 + 11(\hat{\mathbf{n}} \cdot \nabla \times \hat{\mathbf{n}})^2 - 2\sqrt{15}(\nabla \cdot \hat{\mathbf{n}})(\hat{\mathbf{n}} \cdot \nabla \times \hat{\mathbf{n}}) + 16\nabla \cdot [(\hat{\mathbf{n}} \cdot \nabla)\hat{\mathbf{n}} - \hat{\mathbf{n}}(\nabla \cdot \hat{\mathbf{n}})] \}, \quad (3.12)$$

where $|c| \sim 4 \cdot 10^{-10} (\rho_s/\rho) \text{ erg cm}^{-1}$, and (ρ_s/ρ) the fraction between the superfluid and the normal liquid in a static configuration [55], [22], [75].

The most important energies, responsible for the orientation of the $\hat{\mathbf{n}}$ -vector at the wall, are the surface-dipole free energy F_{SD} and the surface-field free energy F_{SH} . The surface-dipole free energy F_{SD} deals with the fact that the orbital angular momentum \mathbf{L} of the Cooper pairs at the wall are suppressed as:

$$F_{SD} = -b \int d^2r (\hat{\mathbf{n}} \cdot \hat{\mathbf{s}})^2, \quad (3.13)$$

where $|b| \sim 1 \cdot 10^{-10} \Delta(T)/\Delta(0) \text{ erg cm}^{-2}$ and $\Delta(T)/\Delta(0)$ indicates the amount of Cooper pairs [55], [22], [75]. $\hat{\mathbf{s}}$ is the surface normal, and parallel alignment of $\hat{\mathbf{n}}$ will minimize the total energy.

When a magnetic field is included, there is a competition between the surface and field aligning forces. The energies of this interplay are expressed in the surface-field free energy F_{SH} [60] :

$$\begin{aligned} F_{SH} &= -d \int d^2r (\hat{\mathbf{s}} \cdot \mathbf{R} \cdot \mathbf{H})^2 \\ &= -\frac{25}{16}d \int d^2r [(\hat{\mathbf{n}} \cdot \hat{\mathbf{s}})(\hat{\mathbf{n}} \cdot \mathbf{H}) + \sqrt{\frac{3}{5}}\hat{\mathbf{n}} \cdot (\hat{\mathbf{s}} \times \mathbf{H}) - \frac{1}{5}(\hat{\mathbf{s}} \cdot \mathbf{H})]^2, \end{aligned} \quad (3.14)$$

where \mathbf{R} is the rotation matrix specified by $\hat{\mathbf{n}}(\mathbf{r})$ and θ (1.16). The second part of the equation is obtained by insertion the rotation matrix with the angle $\theta = \theta_L = \cos^{-1}(-\frac{1}{4})$ (for which the dipole energy is minimized in the bulk liquid). The coefficient d is approximately $\xi(T)(\chi_N - \chi_B)$. The difference in susceptibility ($\chi_N - \chi_B$) between the normal- and the B-phase (Balian-Werthamer state) is maximum at zero temperature, which is approximately $2/3\chi_N$. The temperature dependent coherence length $\xi(T)$ comes in as a length scale over which the order parameter can recover.

The preferred orientation of $\hat{\mathbf{n}}$, for which F_{SH} is minimized, also depends on the relative direction of \mathbf{H} and $\hat{\mathbf{s}}$. In the case that \mathbf{H} is perpendicular to $\hat{\mathbf{s}}$, as in the case of our experiments, it is shown [60] that F_{SH} is minimized when $\hat{\mathbf{n}}$ makes an angle $\beta = \cos^{-1}(1/\sqrt{5}) \simeq 63.4^\circ$ with respect to both $\hat{\mathbf{s}}$ and \mathbf{H} . This situation is illustrated in the figure 3.1, taken from the article by Spencer and Ihas [77].

All these forces mentioned above (and other higher order forces) do want to align the $\hat{\mathbf{n}}$ -vector in the most (energetically) favorable orientation corresponding to that force. However, the superfluid takes the configuration which minimizes the total free energy over the whole sample. This results in continuous change of the orientation from the $\hat{\mathbf{n}}$ -vector over the whole sample, which is called the $\hat{\mathbf{n}}$ -texture [76].

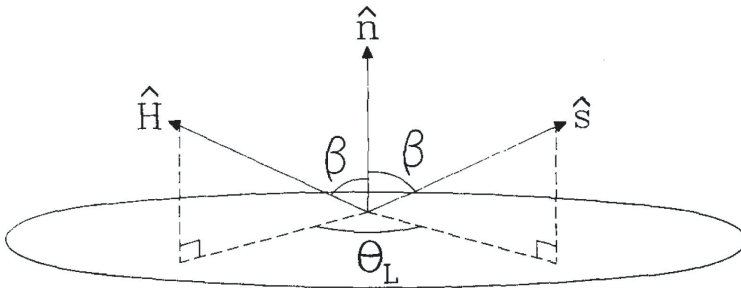


Figure 3.1: The vectors \mathbf{H} , $\hat{\mathbf{s}}$, and $\hat{\mathbf{n}}$ shown relative to a plane perpendicular to $\hat{\mathbf{n}}$ when the surface normal $\hat{\mathbf{s}}$ and magnetic field \mathbf{H} are perpendicular. The angles are given by $\hat{\mathbf{n}} \cdot \hat{\mathbf{s}} = \hat{\mathbf{n}} \cdot \mathbf{H}/H = \cos \beta = 1/\sqrt{5}$ and $\cos \theta_L = -1/4$. Rotation by θ_L about the axis $\hat{\mathbf{n}}$ takes the $\hat{\mathbf{s}}$ vector into the \mathbf{H} vector.

From the four coefficients of the equations (3.11), (3.12), (3.13) and (3.14) we can define one important characteristic length R_c and two characteristic fields H_S and H_B .

$$R_c = \frac{c}{b}. \quad (3.15)$$

This length defines the typical sample size for which the surface-determined orientation of the $\hat{\mathbf{n}}$ -vector is noticeable in the bulk liquid of the sample. When the size of the sample is much bigger than this length, the surface energy becomes more important than the bending energy.

The definition of the characteristic field H_S is given by

$$H_S = \sqrt{\frac{b}{d}}. \quad (3.16)$$

This parameter indicates which surface energy, namely the surface-dipole or the surface-field free energy, is dominating. In low fields the surface-dipole free energy determines the orientation of the $\hat{\mathbf{n}}$ -vector and in high fields the surface-field free energy will.

Finally, the characteristic field

$$H_B = \frac{b^2}{ac}. \quad (3.17)$$

This field indicates whether the bulk or the surface effects have most influence on the orientation on the $\hat{\mathbf{n}}$ -vector.

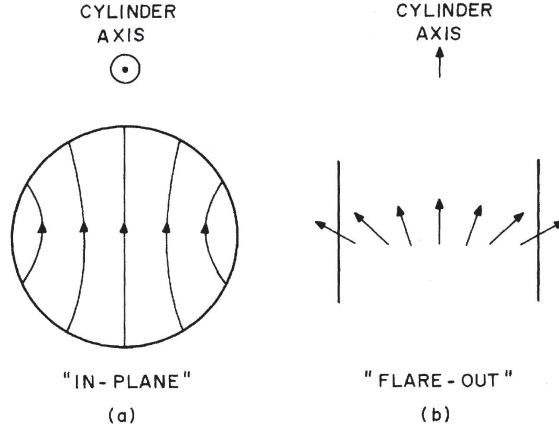


Figure 3.2: Orientation of the $\hat{\mathbf{n}}$ -vector in cylindrical symmetry. (a) in-plane texture and (b) the flare-out texture. Orientation of the cylinder is indicated.

3.4 Orientation of the $\hat{\mathbf{n}}$ -vector in cylindrical samples

In general different textures (in different geometrically samples) seem to be possible. Even in a cylindrical sample, many stable textures can be expected. However, in the case of an axial magnetic field two stable textures are calculated by Smith, Brinkman and Engelsberg [60]. In the absence of a magnetic field (or the limit to zero), the $\hat{\mathbf{n}}$ -vector's orientation is determined by a competition of the bulk-bending free energy and the surface-dipole free energy. If the radius R of the cylinder is close to the characteristic length R_c , the in-plane texture is energetically favorable. Here the $\hat{\mathbf{n}}$ -vector has no component along the z -axis, see figure 3.2 (a) (figure is taken from the article of Smith, Brinkman and Engelsberg [60]). The bulk-bending free energy determines this texture as long as the radius of the cylinder is $R < 10.0R_c$. However for very small R there are some deviations to this texture, due to boundary conditions at the surface.

If the radius of the cylinder is $R \gg R_c$, than the surface energy gets more important³. In this case the boundary conditions put $\hat{\mathbf{n}} \parallel \hat{\mathbf{s}}$, with $\hat{\mathbf{s}}$ the normal to the cylinder wall. As this is impossible in an in-plane texture, the consequence is that the $\hat{\mathbf{n}}$ -vector has to flare out into the z -direction of the cylinder, see figure 3.2 (b). In the absence of a magnetic field the flare-out configuration is the lowest energy configuration as long as $R \geq 10.0R_c$. While it is intuitively clear that axial magnetic fields will favor the flare-out texture, it is generally hard to calculate the reduction of R , for which the crossover between the two textures occurs. However, perturbation theory is done

³The bulk-bending free energy increases like $\ln(R/R_c)$.

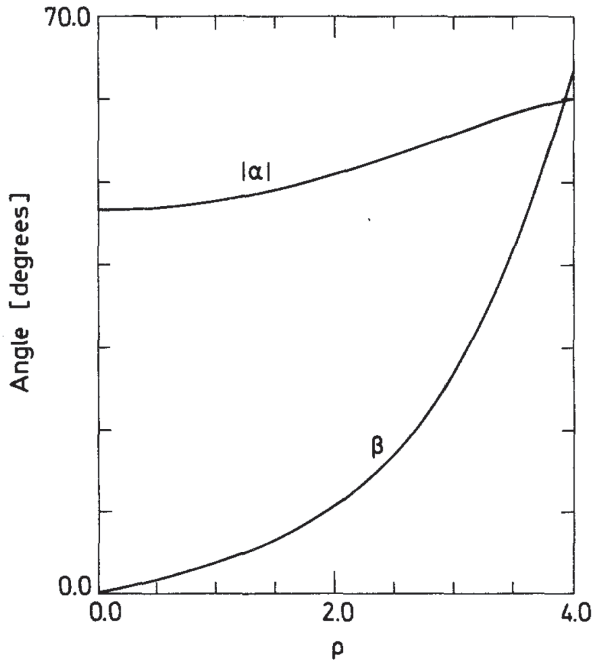


Figure 3.3: The radial dependence of the azimuthal angle α and the polar angle β for a cylinder of radius R . $\rho \equiv r/\xi_H$. The radius $R = 4\xi_H = 4\sqrt{65/8}\xi_H$.

[60], and for small field ($H \ll H_S \wedge H \ll H_B$) the crossover is at a radius of:

$$R = 10.0R_c - 137(H/H_B)^2 R_c. \quad (3.18)$$

For higher magnetic fields ($H \gg H_S$) the surface-field free energy is smaller than the surface-dipole free energy. Here we expect that the $\hat{\mathbf{n}}$ -vector is parallel to the z -axis in the center of the cylinder and aligns itself over a typical length ξ_H (magnetic healing length) to the orientation directed by the surface-field free energy ($\hat{\mathbf{n}}$ has an angle with \mathbf{H} and $\hat{\mathbf{s}}$ of $\cos^{-1}(1/\sqrt{5})$). These two boundary conditions change the $\hat{\mathbf{n}}$ -vector orientation in a spiral-like configuration, which may be parameterized by

$$\hat{\mathbf{n}} = \sin \beta \cos \alpha \hat{\mathbf{r}} + \sin \beta \sin \alpha \hat{\boldsymbol{\phi}} + \cos \beta \hat{\mathbf{z}} \quad (3.19)$$

in cylindrical coordinates. The angles α and β are functions of r only. Its behavior has been studied analytically [78], [79] and numerically [63]. The dependence of α and β do matter on the cylinder size as well, it changes the boundary conditions for α (it may vary between 60° to 38° for $\alpha(0)$) and the way β varies over the sample.

At this point it is convenient to express the radius of the cylinder in terms of ξ_H , the magnetic healing length of $^3\text{He-B}$. We know as long as there is sufficient magnetic

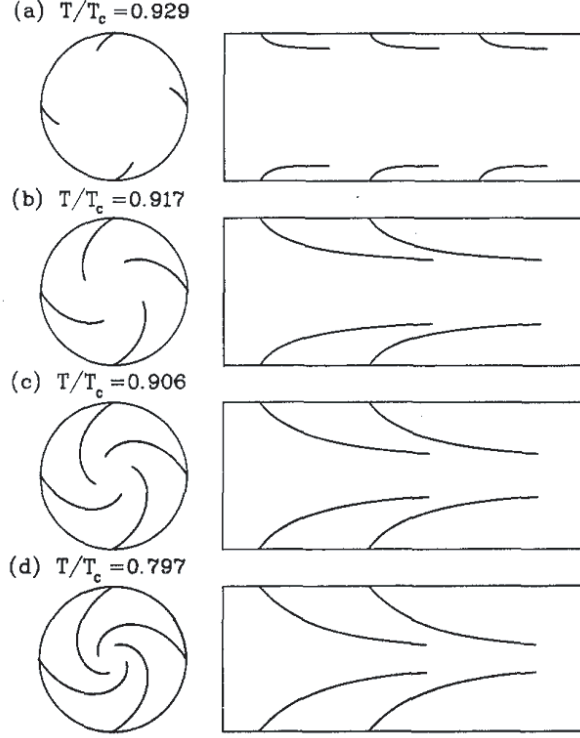


Figure 3.4: Some views of the growing $\hat{\mathbf{n}}$ -texture obtained from the experiment of Spencer and Ihas. Figure is taken from [57].

field the flare-out configuration is favorable. In other words, as long as the radius is at least a couple of times ξ_H the texture should be in the flare-out configuration. So, in the case we deal with cylinders where $R > \xi_H$, the boundary conditions for β are: $\beta(R) = \cos^{-1}(1/\sqrt{5}) \approx 63.4^\circ$ and $\beta(0) = 0$. The angle β changes quadratically for small r with some exponential prefactor. On the other hand, α hardly changes as function of r and is plotted together with β , in the case $R = 4\tilde{\xi}_H = 4\sqrt{65/8}\xi_H$, in figure 3.3. This figure is taken from the article of Jacobsen and Smith [63]. Here the two angles α and β are connected such that the total free energy was minimized.

Experimentally the r -dependence of the two angles was already found by Spencer and Ihas in 1982 [57], and was later worked out in detail [77]. In their transverse NMR experiments they could find the $\beta(r)$ and $\alpha(r)$ by deconvoluting their NMR spectra. As explained in equation (1.39) the magnetic healing length ξ_H grows with decreasing temperature, which enabled them to model the texture growing as it is parameterized by (3.19), see figure 3.4. It is interesting to see, and important for us as we will see later, that the texture gradually grows in a spiral way to the center. The growing

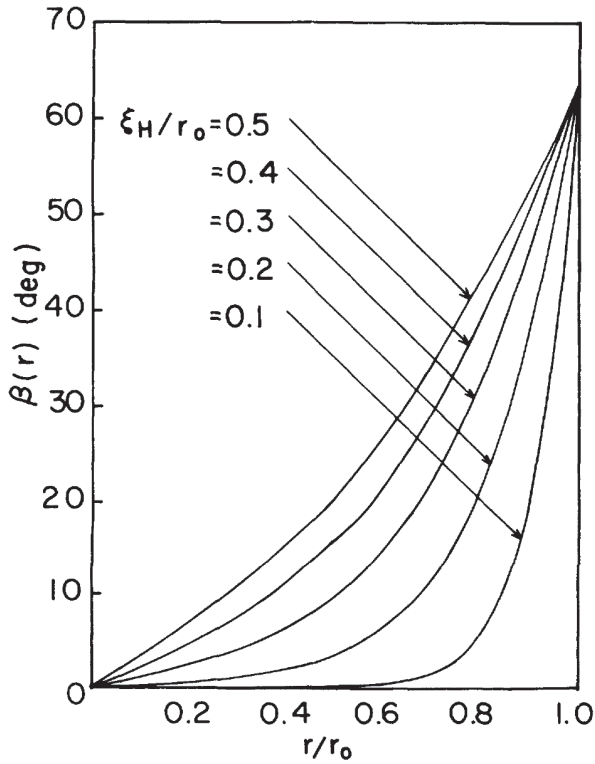


Figure 3.5: $\beta(r)$ for several values of ξ_H/r_0 . Figure taken from [79].

should be able to continue as long as the boundary conditions can be fulfilled, meaning that the flare-out texture will grow as long it is the most energetically favorable configuration.

As mentioned before, much effort is done to calculate the radial behavior of β . The results of Maki and Nakahara [79], who calculated β for different ratios of ξ_H/r_0 are plotted in figure 3.5. All these simulations support the flare-out configuration. Simulations for ratios $\xi_H/r_0 > 0.5$ become hard, as it cannot be approximate linearly. However, one may assume that the most extreme form of the flare-out configuration would be a straight line connecting the boundary conditions, which corresponds to a gradual change of the $\hat{\mathbf{n}}$ -vector over the sample. Not clear is how this is energetically in proportion to other textures. Actually, because of complications in the calculations, it is not clear at all how transitions to other textures should occur when $\xi_H \geq R$. Of course the qualitative answer for the limit $\xi_H \gg R$ is clear. The texture should be completely uniform, and β should have an angle of $\cos^{-1}(1/\sqrt{5})$, as is imposed by the surface.

3.5 Spin dynamics in a non-uniform texture

The influence of non-uniform textures on spin dynamics can be solved with the Hamiltonian approach. In this case the Hamiltonian of equation (3.2) should be extended with the gradient free energy density of equation (1.31). By assuming the following: The equilibrium $\hat{\mathbf{n}}$ varies on a scale of ξ_H , θ_μ varies on a scale of ξ_D (which is much longer than ξ_H , see section (1.8)), spin-orbit angle is fixed ($\theta = \theta_L$) and parameterize the order parameter in terms of θ_μ , the bending energy is given as [60] [80]

$$f_{bend} = \frac{1}{2} \frac{\chi}{\gamma^2} \Omega_B^2 \xi_D^2 \left\{ \bar{K} \sum_{\mu\nu} (\nabla_\mu \theta_\nu)^2 - \bar{K}' \left[\sum_{\mu\nu} R_{\mu\nu}^L (\nabla_\mu \theta_\nu) \right]^2 \right\}. \quad (3.20)$$

The coefficients are given by $\bar{K}' = \bar{K}_2 + \bar{K}_3$ and $\bar{K} = 2\bar{K}_1 + \bar{K}'$ with $\bar{K}_j = K_j \Delta^2 \gamma^2 / (\chi \Omega_B^2 \xi_D^2)$. $R_{\mu\nu}^L$ is the rotation matrix at the dipole-locked rotation angle ($\theta = \theta_L$), which contains the information of the equilibrium $\hat{\mathbf{n}}$ -vector (see equation (1.16)).

The spin equations (dynamics) can now be solved from the effective Hamiltonian, hence

$$i\hbar \dot{\mathbf{S}} = [\mathbf{S}, H_S + f_{bend}]. \quad (3.21)$$

Considering a weak rf-field \mathbf{B}_1 in a static uniform magnetic field \mathbf{B}_0 (determining the z -axis), Theodorakis and Fetter [81] showed that the following differential equation is obtained

$$(D_m + V_m)\theta_m = \frac{1}{\Omega_B^2} [(\omega^2 - m\omega\omega_L - \Omega_B^2)\theta_m - i\omega\gamma H_{1m}], \quad (3.22)$$

where $V_m = -1 + |\hat{\mathbf{n}}_m|^2$ and $D_m \equiv D_{mm}$:

$$D_{\mu\nu} = \xi_D^2 \left[-\delta_{\mu\nu} \bar{K} \nabla^2 + \bar{K}' \sum_{\lambda\lambda'} (R_{\mu\lambda}^L \nabla_\lambda)(R_{\nu\lambda'}^L \nabla_{\lambda'}) \right]. \quad (3.23)$$

The differential equation can be rewritten in the form of the Schrödinger equation (assuming that there is a no spin super current through the surface)

$$(D_m + V_m)\psi_{m,k} = E_{m,k}\psi_{m,k}. \quad (3.24)$$

Here D_m and V_m play the role of the kinetic and the potential energy, respectively. The polarization of the vector field is indicated with m . Transverse components coincide with $+$ and $-$, and the longitudinal component with $m = 0$. The two equations can be connected by expressing θ in terms of eigenfunctions $\psi_{m,k}$:

$$\theta_m(\mathbf{r}) = \sum_k c_{m,k} \psi_{m,k} \quad (3.25)$$

where $c_{m,k}$ is chosen such that equation (3.22) can be regained. The relations of the (k th) eigenfrequencies and energies are then given by.

$$\omega_{m,k}^2 - m\omega_{m,k}\omega_L - \Omega_B^2 = E_{m,k}\Omega_B^2. \quad (3.26)$$

It is this set of frequencies, which correspond to spin waves, which can be experimentally accessed.

3.5.1 Cylindrical geometry

Spin waves can be expected if one goes to restricted geometries, where the surface plays an important role in the orientation of the $\hat{\mathbf{n}}$ -vector. In general the differential equation (3.24) for a given geometry is not trivial to solve. However, for the parallel-plate and cylindrical geometries the differential equation, to a certain extent, can be solved. In the case of slab geometry (separation of the plates $L \leq \xi_H$) and \mathbf{B}_0 parallel to the plates, transverse NMR experiments could detect spin waves [59]. Here the spacing between the spin waves (NMR resonances) was (more or less) constant, and the intensity dropped as a function of k^{-1} . This is in good agreement (at least to first order) with the solution of the differential equation (3.24) for this geometry [82].

Our experiments are performed in a cylindrical geometry in a transverse NMR configuration. The effective potential V_m , see equation (3.22), for the transverse case ($m = +$), where the equilibrium $\hat{\mathbf{n}}$ -vector for long circular cylinders is parameterized as in equation (3.19), is axially symmetric and given as:

$$V_+ = -1 + \frac{1}{2} \sin^2 \beta. \quad (3.27)$$

In this axially symmetrical case the differential equation (3.24) is given by [79]:

$$(-\bar{K} + \bar{K}' |R_{+r}^L|^2) \xi_D^2 \left[\frac{1}{r} \frac{d}{dr} \left(r \frac{d}{dr} \right) \right] \psi_{+,k} - \left(1 - \frac{1}{2} \sin^2 \beta \right) \psi_{+,k} = E_{+,k} \psi_{+,k} \quad (3.28)$$

If we are in the experimental situation, illustrated in figure (3.3), the potential V_+ varies (determined by its boundary condition) between -1 ($r = 0$) and $-3/5$ ($r = R$). It has a quadratic behavior near its center, and one may want to replace the $1/2 \sin^2 \beta$ part with $(r/L_1)^2$, where L_1 is a measure for the curvature bounded by the boundary conditions. By taking $|R_{+r}^L|^2 = 1/2$ (which is its value at $r = 0$), the differential equation reduces to the Schrödinger equation for the two dimensional harmonic oscillator. One may consider these approximation a bit rough (errors over 10% far from the center can be expected). However, it is, as shown later in this thesis, interesting to investigate which features a quadratic potential would show in the transverse NMR experiments.

The eigenvalues of the two dimensional harmonic oscillator are given by

$$E_{+,k} = -1 + 2\sqrt{\left(\bar{K} - \frac{1}{2}\bar{K}'\right) \frac{\xi_D}{L_1}} (k + 1). \quad (3.29)$$

Only the s -wave states couple to the homogeneous rf-field, or with other words: only the $l = 0$ modes have non-vanishing intensities in experiments using uniform rf-fields [63]. Consequently, only the even k modes couple to the corresponding NMR frequencies. It means for the eigenvalues that they are equally spaced, like in the case of slab geometry. However, the relative intensity is given by:

$$I_k/I_0 = 1 \text{ for } k = 2, 4, 6, \dots \quad (3.30)$$

Where I_k is the intensity of the k^{th} spin wave mode. The NMR absorption lines for the excited modes should all show the same intensity. This is in sharp contrast with the planar \hat{n} -textures, here the intensity drops as k^{-1} . However, experiments performed with cylindrical geometries do show a decrease of intensity with increasing k [62]. Jacobsen and Smith [63] did numerical calculations, where the configuration of the texture (which determines the effective potential) was determined by minimizing the appropriate free energy and solving the resulting Euler-Lagrange equations. It explained the experimental data, for which the quadratic potential approximation seemed to be too crude.

3.6 The magnetic healing length of $^3\text{He-B}$

In section 1.8 a rough estimation of the magnetic healing length in the B-phase was performed. It shows the physical properties but it fails to describe the healing length in detail. The experimentally found magnetic healing length as function of temperature near melting curve pressures $\simeq 30$ bar and 30 mT, as fitted by Maki and Nakahar [79], are put in figure 3.6. The fit was obtained from data at temperatures between the transition temperature T_c and $0.7 T_c$. At lower temperatures an extrapolation of these fit functions was used. However, for the lowest temperatures it will more likely be proportional with the gap energy. Both fits show the same behavior before extrapolation and are approximately 0.5 mm for temperatures at $0.7 T_c$ and magnetic fields of 30 mT. In our experiments the magnetic field was half this value (15 mT), and according to (1.39) one should than expect a healing length of 1.0 mm. In addition equation (1.39) shows a ξ_0 dependence, which is 5 times longer for zero pressure compared to the melting pressures. It is reasonable to believe that our magnetic healing length is at least 5 mm for zero pressure, and ~ 2.5 mm for 6 bar at $0.7 T_c$ and 15 mT⁴.

3.7 NMR absorption in cylinder of 1 mm diameter

The NMR experiments performed in the cylindrical part of the cell with a cross section of 1 mm in diameter are done at relatively low pressures. Several measurements were done with a pressurized cell between 0 and 6 bar. The data is obtained by

⁴The data of Spencer and Ihas indeed show (roughly) 3 times longer magnetic healing length ξ_H^B for the low pressure data (2.89 bar) compared to the melting curve pressure.

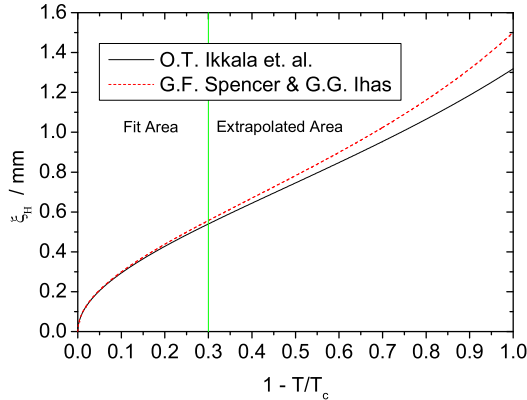


Figure 3.6: Fit of the magnetic healing length as function of temperature, obtained from the data from Spencer and Ihas [57] and Ikkala *et al.* [58]. Both have comparable systems with pressures around ~ 30 bar with magnetic fields of ~ 30 mT. The fit is obtained from data between T_c and $0.7 T_c$. The curves at lower temperatures are extrapolates of the fit functions. Both areas are separated by the green line in the figure.

increasing temperature sweep, which gives 'better' thermal equilibrium and minimizes the hysteresis effects of the superfluid.

These measurements were all done in the same way. First the cell was put at the desirable pressure, same temperature far above the T_c of the superfluid. Then the whole system was cooled down by adiabatic cooling of the nuclear stage. Typically till temperatures of $0.3 T_c$. At this point we waited till the whole system was in thermal equilibrium, as observed from the melting curve thermometer and the tuning fork. To increase the temperature, the magnetic field of the nuclear stage was slowly increased. Simultaneously, the cw-NMR measurements were started, and the data were collected nonstop by a labview controlled system.

The benefit to warming up the system adiabatically is that, at least ideally, the total amount of entropy is conserved. Measurements could be repeated much faster, without the time consuming pre-cooling of the nuclear stage. The disadvantage of this method is that stray fields of the magnet are not constant. While compensation coils reduce almost all the field at the experimental space, still a small fraction (around 0.01 %) can be seen in the NMR spectrum as a contribution to \mathbf{B}_0 . Practically it is not a problem to compensate for this effect, especially considering the benefits of this method.

Increasing (slowly) the field constantly in time, results in a proportional increase

of the temperature ⁵.

$$T = T^* + \frac{T^*}{B^*} \Delta B(t), \quad (3.31)$$

where T^* and B^* are the initial temperature and magnetic field and $\Delta B(t)$ the field added at B^* after $t = 0$. Typically the temperature was increased by 0.31 mK h^{-1} . The sweep time for the cw-NMR was typically 7 minutes, which means that the temperature increases by $\sim 35 \text{ } \mu\text{K}$ from start to end. Significant changes in the NMR spectra happen at much longer temperature scales. Meaning that temperature sweep is sufficient to map a good temperature dependence with the NMR technique.

A typical temperature sweep of the NMR spectrum is plotted in figure 3.7. Here the measurement is performed at 6 bar, and the temperature is swept between 0.57 mK and 1.56 mK (transition temperature).

At and above T_c the resonance frequency occurs at the Larmor frequency. Below T_c and at this pressure, the ^3He will have a transition from the normal phase to the B-phase. Technically, due to the magnetic field of NMR, it is in the B₂-phase. However, the NMR frequencies are low, meaning the population differences are approximately zero, see equation (1.30). To a very good approximation the values of the spin susceptibility and θ_L can be taken from the B-phase as well. Still the $\hat{\mathbf{n}}$ -vector has a preferred orientation, due to magnetic field and surface effects, and a resonance frequency shift, as described in equation (3.9), can indeed be seen in the figure.

Section 3.4 explained that for a cylindrical symmetric container with an axial magnetic field, in which the radius is at least a few times the magnetic healing length ξ_B , a flare-out texture can be expected. For temperatures near T_c the healing length is indeed smaller than the diameter (1 mm) of the cylinder. However, as explained in the previous section, the healing length increases to approximately 2.5 mm at $0.7 T_c$ for 6 bar, which is 5 times the radius of the cylinder. One should expect, from energetic arguments, a uniform texture where all the $\hat{\mathbf{n}}$ -vectors have an angle β (angle between the $\hat{\mathbf{n}}$ -vector and external applied magnetic field \mathbf{B}_0) of $\cos^{-1}(1/\sqrt{5})$.

The line shapes in figure 3.7 show that such a uniform texture is not created. As the temperature decreases ⁶ the absorption spectrum becomes wider, meaning that the orientation of the $\hat{\mathbf{n}}$ -vector radially changes in the cylinder. A more peculiar phenomenon becomes clear for temperatures below $0.7 T_c$. One can notice spin waves in the NMR spectrum. The spin waves are more or less equally separated, but more importantly they have approximately the same intensities. This effect, as described in section 3.5.1, is expected for textures in a flare-out configuration, which forms a quadratic potential. For the lowest temperatures (at 6 bar) one can clearly distinguish 5 spin wave modes, lower pressures reduce the amount of modes. This pressure dependence will be worked out in detail in the following section.

⁵In an ideal adiabatical magnetization system the ratio between magnetic field and temperature is constant, $B/T = B^*/T^*$. If one starts with a magnetic field B^* the current magnetic field can be expressed as $B = B^* + \Delta B(t)$, where $\Delta B(t)$ is the increased amount of magnetic field after $t = 0$.

⁶Technically the data is obtained with increasing temperature, but has the same behavior for decreasing temperatures. See remark next paragraph.

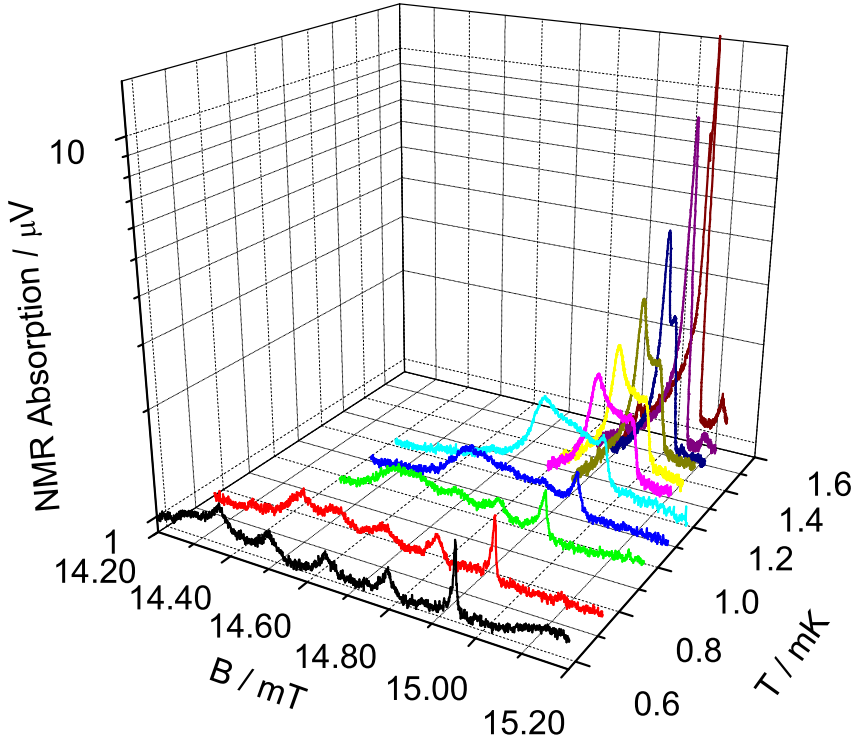


Figure 3.7: NMR absorption scans of helium in a cylinder with a radius of 0.5 mm at 6 bar for various temperatures. The absorption is expressed in μV , which is the signal measured with the pick-up coil. The temperature range is between 0.57 mK and T_c (1.56 mK). At the transition temperature the absorption peak is in resonance at the Larmor frequency, lower temperatures show a shift of the resonance frequency due to texture effects. At even lower temperatures, $T/T_c < 0.7$, several spin waves modes become visible.

At this point it should be emphasized that the cell was always pressurized in the normal phase. So, before the start of every measurement, the liquid was cooled from the normal phase to the superfluid phase. The data presented in this thesis are obtained at increasing temperature sweeps, which gives quantitatively better temperature reliability, however decreasing temperature sweeps show qualitatively the same results. Beginning the cool down above T_c starts the texture in the flare-out

configuration. Increasing the magnetic healing length ⁷ does not show any textural transition. Somehow the texture seems to get stuck in this configuration.

3.8 Metastable texture

From the data shown in figure 3.7 one can conclude that the $\hat{\mathbf{n}}$ -vector finds itself still in the flare-out configuration. Somehow it does not make a transition to another textural distribution. It may be that such a transition corresponds with sharp jumps of the $\hat{\mathbf{n}}$ -vector, which will definitely be discouraged by the bulk-bending free energy. If that is the case, one can consider the flare-out configuration, at low temperatures, as a metastable state.

Assuming the state is still in the flare out configuration for such long magnetic healing lengths, it is unclear how the angle β radially distributes over the cylinder, except that the boundary conditions determine that β should increase from 0 at the center to $\cos^{-1}(1/\sqrt{5}) \approx 63.4^\circ$ degrees at the surface. From figure 3.5 one can see that for increasing magnetic healing lengths the curve becomes straighter. Here simulations for magnetic healing lengths up to half of the radius were presented, which could still be performed in a linear regime. Longer magnetic healing lengths make these calculations hard or unreliable. However, by extrapolating the curves, one can assume that in the most extreme case of a flare-out configuration β will increase proportionally with r . In other words, the $\hat{\mathbf{n}}$ -vector changes gradually from the surface to the center, which is also the distribution giving the lowest bending free energy.

The potential of equation (3.27), assuming that $\beta(r)$ is proportional with r , is plotted together with a quadratic potential in figure 3.8. The maximal relative difference between those two potentials is 6.5%. To analyze our data we do not consider this difference problematic, so that we can replace the potential in the differential equation (3.28) by a quadratic potential, to get an analytically solution. By combining the equations (3.26), (3.29) and (3.6) we get:

$$(\omega_k - \omega_L)\omega_k = \frac{6\gamma^2}{\chi_B} g_D(T) \sqrt{\left(\bar{K} - \frac{1}{2}\bar{K}'\right)} \frac{\xi_D}{L_1} (k+1). \quad (3.32)$$

In literature [83], [62], [79] one of the most important temperature dependency concerning the spin waves modes is the growing (or decreasing) magnetic healing length. As in our case the texture appears to be 'stuck', the effective magnetic healing length seems to stay constant for temperatures of $T/T_c < 0.7$, and so should L_1 . In this quadratic potential and cylindrical cell with a radius of 0.5 mm the length $L_1 = \sqrt{5/2} R \approx 7.9 \cdot 10^{-4}$ m.

The dominating temperature dependencies are coming from the gap energy $\Delta(T)$ and the spin susceptibility $\chi_B(T)$. By combining the equations (1.3), (1.4), (1.5), (1.6), (1.21), (1.32), (1.33), (1.36), (3.6) and using the definitions of \bar{K} and \bar{K}' from

⁷It is increasing by decreasing the temperature.

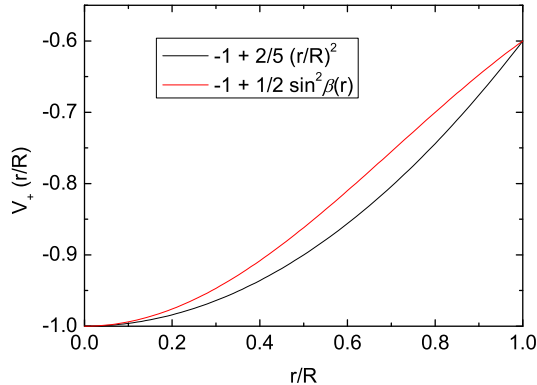


Figure 3.8: The potential V_+ and a quadratic potential in a cylindrical symmetric container of radius R are plotted as function of r . Here it is assumed that $\beta(r)$ is proportional with r . The only requirement for the quadratic potential is that it has the same boundary conditions as V_+ , meaning it varies from -1 in the center to $-3/5$ at the surface.

(3.20) we can rewrite (3.32) as

$$(\omega_k - \omega_L)\omega_k \approx 6\sqrt{\frac{14\zeta(3)}{240\pi^3}}(1.76)^2\gamma(1 + F_0^a)\sqrt{\frac{v_F^3}{\hbar^3}k_B T_c} \frac{m^*}{L_1} \times \ln\left(\frac{2\varepsilon_c}{1.76k_B T_c}\right) \frac{\chi_N}{\chi_B(T)} \frac{\Delta(T)^2}{\Delta(0)^2}(k+1). \quad (3.33)$$

The equation is now expressed in natural constants and pressure dependent observables as listed in the appendix A.1. The temperature dependence of $\Delta(T)/\Delta(0)$ and $\chi_B(T)/\chi_N$ are plotted and fitted in appendices A.2 and A.3, respectively.

The following two graphs (figures 3.9 and 3.10) contain the (average) position of the spin wave modes, as function of temperature, for 0 and 6 bar, respectively. Also the theoretically expected positions, according to equation (3.33), are plotted. The position is expressed as their frequency multiplied with the difference between the Larmor frequency. Data of the spin waves peaks are from temperatures below $T < 0.7T_c$, for which the overlap of the peaks is reduced enough, so they can be distinguished from each other.

The separations of the peaks are not perfectly equal. However, at higher pressures this seems to improve, which probably means that the potential is better approximated by a quadratic one. The maximal relative difference between the data and theory is over 20 %, however the essence of measurements can be explained by theory. More important the number of modes seems to grow as function of pressure. For zero

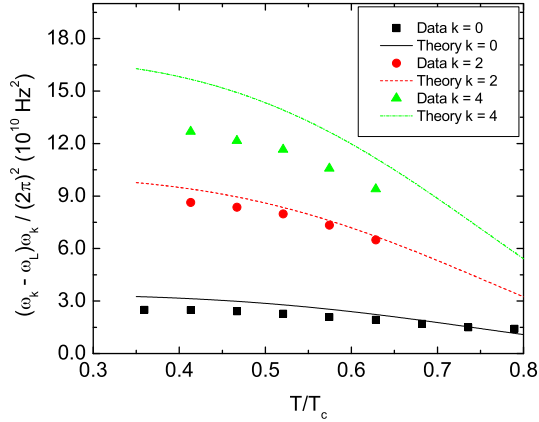


Figure 3.9: Here the spin wave data, at 0 bar, are plotted as function of reduced temperature. The data points correspond to the positions of the spin wave modes as observed in the measurement. The lines correspond to the positions of the peaks as predicted by theory. In total 3 modes are detected.

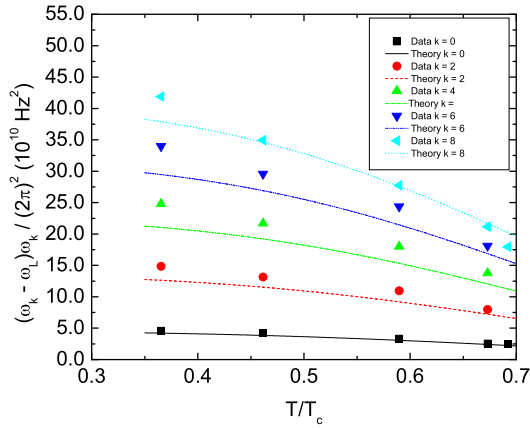


Figure 3.10: Here the spin wave data, at 6 bar, are plotted as function of reduced temperature. The data points correspond to the positions of the spin wave modes as observed in the measurement. The lines correspond to the positions of the peaks as predicted by theory. In total 5 modes are detected.

pressure 3 modes are observed, to 5 modes for 6 bar.

The geometrical pre-factors and L_1 ⁸ are constant. The dipole coherence length ξ_D , see equation (1.37), is proportional to the coherence length ξ_0 , which depends on pressure. We use equation (3.29) to calculate the amount of spin waves that can be formed in this potential. In the weak-coupling Ginzburg-Landau limit the eigenvalues are only pressure dependent. Then \bar{K} and \bar{K}' are 8/5 and 4/5, respectively. In this limit only the dipole coherence length ξ_D change as function of pressure, which can be tuned between 32 (zero pressure) and 7 μm (melting pressure). The energy difference between the modes of equation (3.29) is decreasing as function of pressure and as the potential (at least for $T/T_c < 0.7$) is unchanged more spin waves can exist in the system by higher pressures. Of course only discreet numbers of modes can exist.

The spin wave modes for several different pressures obtained at the lowest achievable temperatures are shown in figure 3.11 and their relative intensities in figure 3.12. The theoretically predicted positions of the spin wave peaks at zero temperature⁹ are plotted as well.

The measurements are in good qualitative agreement with the theory. Still the trend is that the theory predicts smaller spacing between the frequencies of the spin modes. Higher spin wave frequencies (bigger spacing) are expected for steeper increasing potentials, and as shown in figure 3.8, V_+ is indeed steeper than the quadratic potential (except close to the cell wall). This may explain the mismatching between the two. Also the amount of spin modes is as predicted by theory. There is one exception, for zero pressure one would expect 2 spin wave modes, however we see 3 modes. The frequency of the highest mode, see green line in figure 3.9, has the largest differences from the theory and its intensity, which is different from the normal trend, as we will show later. Somehow it seems to be a half mode, a spin wave which is seen to be into the system. Another possibility is that it is a side effect due to the finite length in the z -direction. Nevertheless, the reason is not very clear and the effect is only visible for zero pressure. At higher pressures (above 1 bar) such artifacts do not appear and seem to be in (reasonable) agreement with theory.

The width of the absorption peaks gets wider for higher k and increases maximally by a factor of 5. We believe that the most important cause of this is due roughness at the wall. The cell is made of the plastic Polyetherimide PEI of which the surface is relatively rough. As the transverse component is maximal at R (at the wall) one would expect to see the most surface effects for higher k , for which the weight of the wave function is closer to the surface. More peculiar is that the intensity of each mode is increasing as function of k , as is shown in figure 3.12. Here the relative intensity can increase to 2.5 - 3 times. For a 2D harmonic oscillator in a cylindrical symmetry one would expect the same intensity for all k -modes (solid lines of figure 3.12), a consequence of the behavior of the density of states in this 2D system (with quadratic potential), which is then a constant. An increase of the intensity for the higher k -

⁸As we have assumed.

⁹The obtained data is from temperatures lower than 0.3 T_c . As can be seen from appendices A.2 and A.3 only very small changes due to temperature are expected, which makes to data suitable to compare with zero temperature theory.

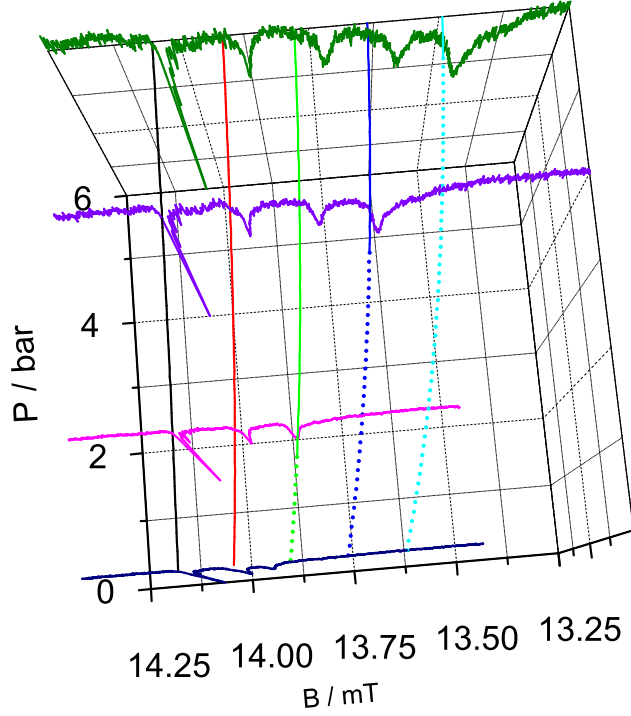


Figure 3.11: Spin wave absorptions peaks as function of magnetic field by pressures of 0, 1.5, 4 and 6 bar. The absorption is expressed in arbitrary units and corresponds with temperatures below $0.3 T_c$. The longest peak corresponds with mode $k = 0$, the neighboring peak to the mode $k = 2$, and so on. The curves are the theoretically predicted spin wave frequencies at zero temperature. Black, red, green, blue and cyan correspond with the mode 0, 2, 4, 6 and 8, respectively. All curves are plotted (dotted) for increasing pressures (started from 0 pressure), but become solid when theory predicts the mode to exist.

modes is what one would expect if the potential would increase faster compared to a quadratic potential (and a constant density of states).

By taking the density of states constant, the potential energy is known at the boundary (surface) and using the relative increase of the intensities as given in figure 3.12, we could reconstruct the potential, as plotted in figure 3.13, in our cell as it should be according to our data. The reconstruction of the potential was done for all four pressures. However, we believe that data for the higher pressure is more reliable,

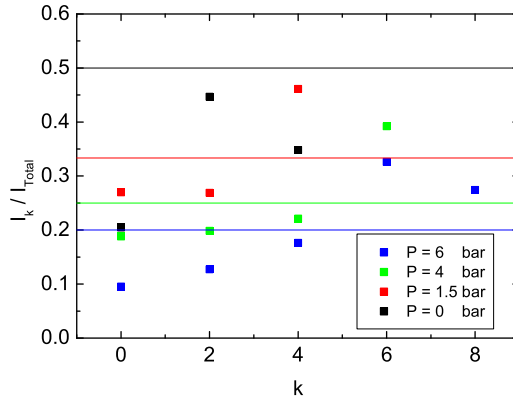


Figure 3.12: The relative intensities of the k modes from the data of figure 3.11. The scattered data are the estimations of the measurements, well the lines correspond to the theoretical prediction if the potential is perfectly quadratic. Black, red, green and blue squares corresponds to the pressures of 0, 1.5, 4 and 6 bar, respectively.

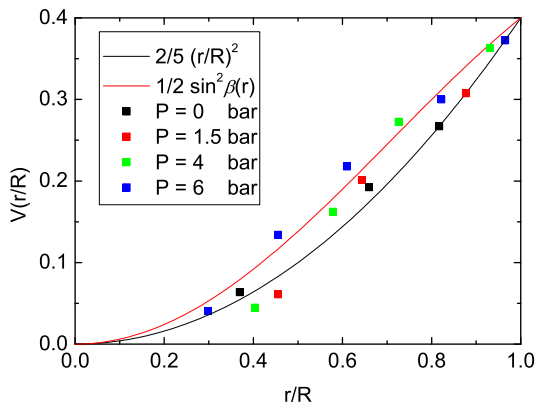


Figure 3.13: The reconstructed potential from the data of figure 3.12. The data points are calculated values of the potential as function of the radius for different pressures. Black, red, green and blue squares correspond to the pressures of 0, 1.5, 4 and 6 bar, respectively. The solid lines are the potentials discussed in figure 3.8.

since the reconstructed data points of the potential coincide with the amount of spin waves modes. If one can compare more absorption peaks with each other, the errors

will reduce. Also the spatial dependencies become clearer with more data points.

The potential (especially clear for the higher pressures) seems to follow the potential of $1/2 \sin^2 \beta(r)$ for $r > 0.5R$, for small r there seems a trend to drop faster. However, the lack of sufficient data makes it hard to give a strong statement. To investigate the potential at small r , measurements at higher pressures should be performed. Presently we can conclude that our results are consistent with a proportionality of β with r for $r > R/2$.

3.9 Textural transition

The textural configuration described in the previous section is from energetic point of view not the expected state. However, it seems to be a stable state and once the superfluid is in this configuration no transition to another textural configuration is observed. Most cool downs were executed with a relatively slow speed rate, to be sure that the nuclear stage was cooled adiabatically. Faster¹⁰ cool downs would sometimes show, at least initially, a more uniform shift of the absorption peak. This phenomenon made us realize that the creation of a flare-out texture is correlated with a sufficiently slow enough cool down. As already mentioned in the previous section, the slowly growing texture is forced to stay in this configuration, as the threshold to jump to a different may be too high.

If one would cool down more rapidly, the magnetic healing length ξ_H^B would grow and oversize the radial dimension of the system much faster than in normal procedure. At the moment the superfluid is formed the $\hat{\mathbf{n}}$ -vector is not given the time to grow smoothly into the flare-out configuration. The surface will dominate the forming of the configuration, and a completely uniform texture would be expected. One of the fastest ways to cool down the liquid would be to cool the system to lowest temperatures, and then locally (while the rest of the system is kept cold) warm the superfluid above T_c . At the moment the liquid is in the normal state one should stop the heat input, so that the locally heated liquid will cool down to the initial temperature. The heat only needs to be removed locally, instead from the whole system, which makes the cooling of the liquid considerably faster.

By doing NMR, one always heats the sample locally. As explained in section 2.4 the absorption signal actually shows the change in the fractional resistance $\Delta R/R_0$. The ΔR is the dissipation due to NMR and the average power dissipated in the liquid is then equal with

$$\bar{P} = i^2 \Delta R, \quad (3.34)$$

with i the average alternating current through the coil. As the field lines of \mathbf{B}_1 are almost uniform over the whole sample, most dissipation (at least till first order) occurs in the volume between the two coils of the Helmholtz tank coil, see figure 2.15. Increasing the voltage over the tank circuit, would increase the power absorbed into the liquid in this volume. The energy needed to make the superfluid (at $T = 0 K$)

¹⁰The speed rate of the cool down should still be in the adiabatically regime, but faster than the usually procedure.

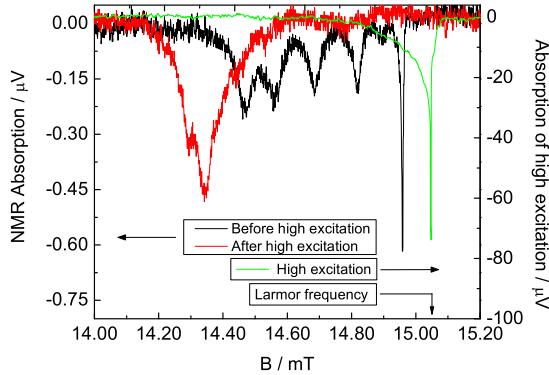


Figure 3.14: Local heating of the superfluid with NMR. The black and red curves show the absorption spectrum of 6 bar at 300 μK before and after heating the sample, respectively. The corresponding values of both absorption curves are put on the left y -axis. The green curve corresponds with the absorption curve while heating the sample, absorption values are put on the right y -axis. Here the values are 2 orders of magnitude higher, so enough energy is dissipated to locally warm up the liquid to the normal state, as is indicated by a jump of the peak to the Larmor frequency. After the local heating, the texture is changed from flare-out to a uniform configuration.

normal, is roughly equal the product of the volume and the energy density of equation (1.9). For 6 bar this is approximately equal to

$$(F_n - F_s) V \approx \frac{1}{4} N_F (1.76 k_B T_c)^2 V \approx 2.58 \cdot 10^{-9} \text{ J}. \quad (3.35)$$

To overcome this energy threshold one should dissipate sufficiently long, since the power is low. However, ^3He in the superfluid state is a good thermal conductor and to be sure that the liquid is only heated locally, one should pump the energy relatively fast into the system. In principle one could calculate how much voltage should be put over the tank circuit to dissipate enough power, but it is a complicated problem since the increasing voltage changes the parameters like the Q ¹¹ of the tank circuit. In practice one can easily notice when enough energy is dissipated, as one can see that the frequency of the absorption peak(s) shift back to the Larmor frequency.

Let us start from the situation at 6 bar (around 300 μK) with the usual spin waves, which correspond to the black curve in figure 3.14. From here the excitation is inflated

¹¹Higher voltage increases the current in the tank circuit. More current give more dissipation, and a new situation where heat in- and output are in equilibrium need to be established. For the usual excitations, the current is small enough that it is not the dominating dissipation factor, and no effects on the Q can be seen.

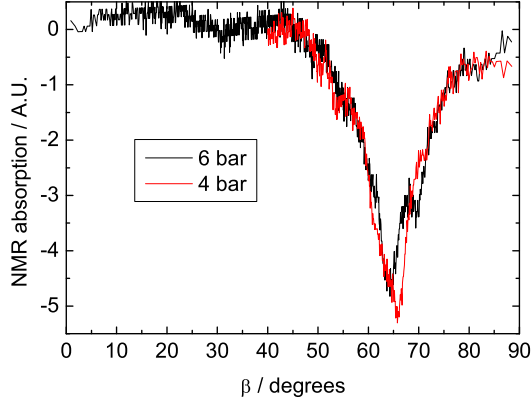


Figure 3.15: Absorption spectrum convert to β dependency. Here the data for 4 and 6 bar (at $300 \mu\text{K}$) are presented. The data show a Lorentzian behavior, for where the center is around 64.7° . FWHM is around 10.5° and is considered mainly due to surface roughness.

to $\sim 6.4 \text{ mV}$, which is 100 times more than in the usual NMR experiments. The result is the green curve, from which one can estimate ΔR ($4.57 \cdot 10^{-4} \Omega$). As described in section 2.4, one can calculate the current i through the coil ($2.24 \cdot 10^{-4} \text{ A}$). The average power dissipated is then $\bar{P} = 2.29 \cdot 10^{-11} \text{ W}$. The sweep through resonance takes about a minute, so the total amount of dissipated energy is $\sim 1.37 \cdot 10^{-9} \text{ J}$. If one compares this with the upper limit (3.35), it is certain that the amount of heat dissipated in the superfluid is enough to put it in the normal state. This is corroborated by the fact that the absorption peak jumps to the Larmor frequency, where the width is mostly determined by the inhomogeneity of the magnet.

To limit the total amount of heat input, the voltage is immediately reduced to its initial value if the jump to the Larmor frequency is observed. The local heated liquid starts to cool and the absorption peak moves uniformly to the left as the liquid becomes superfluid. The red curve in figure 3.14 shows the equilibrium result, when the liquid is cooled back to $300 \mu\text{K}$. The spin wave modes have disappeared, and the NMR absorption signal only shows a single peak, indicating that the superfluid is in a uniform texture. The total absorption (intensity) of both line shapes are equal, which is expected as the total amount of atoms is equal.

This procedure is repeated for several different pressures and all show the same behavior. Using equation (3.9), which gives the relation between the signal frequency and the angle β of the $\hat{\mathbf{n}}$ -vector with respect to \mathbf{B}_0 , we can plot the absorption spectrum as function of β . This is done for 4 and 6 bar in figure 3.15.

The curves show a Lorentzian behavior, whose center is around 64.7° with a

FWHM of 10.5° . The angle is sufficient close to the expected 63.4° . The deviation is most likely dominated by the imperfect alignment between cylinder axis and magnetic field. It seems reasonable that 1.5° difference, compared to perfect parallel alignment, is noticeable. So, we indeed see a uniform texture with the angle as expected from energetically arguments. The width of the peak is wide compared to the absorption peaks from the spin waves. As now the direction of the texture is completely determined by the cell wall, one would expect a full reflection of the roughness in the NMR spectrum. It is understandable that roughness broadens out the NMR signal, but it is hard to make a quantitative conclusion from the width, as different wall roughness can give the same width.

Once this new texture is created it seems to be a stable state as well, even if the superfluid is warmed up (of course one stays under the T_c of the superfluid), no transition is noticeable. However, we do see a change as the helium bath of the cryostat is refilled. The filling line (capillary) of the cell goes through the bath and there was no possibility to close this capillary near the cell. The pressure in the capillary is thus the pressure which pressurizes¹² the cell. At the moment we start filling the helium bath, (relative) warm gas flows over the capillary and later when the refilling continues liquid ^4He surrounds it. In other words the equilibrium situation is disturbed. At each liquid helium transfer, the fluctuation in the pressure gets enough that the liquid is warmed up to the normal phase. The moment the fluctuations are small enough that the system can be cooled again¹³, it grows into the flare-out texture.

The nuclear stage may warm up by vibrations¹⁴ created due to filling. It is considered to be a small effect, even in this case the temperature of the environment is already cold. However, the fact that the liquid as a whole had to be cooled again seems to be sufficient to let the texture grown into the flare-out configuration. We did not study systematically the influence of the cooling rate on the type of texture, as that was too difficult concerning the configuration of our cryostat.

3.10 Discussion

From what we have encountered in our experiments, we were able to create a stable flare-out texture till the lowest temperatures. From the energetically point of view it was a surprising effect, and as pointed out by the experiments of local heating, the cooling rate played an important role of the forming of the texture. The configuration of our experimental cell made it too difficult to do better quantitatively cool down experiments. Better cooling experiments should be achieved in cells such as the

¹²The pressures used in the experiments are such that no plug (solid) is formed in the capillary as in contrast with the melting curve thermometer.

¹³Our experience is that the warm gas through the transfer tube is responsible for the increase of the fluctuations. Once the transfer tube is cooled enough, so liquid ^4He is transferred, the fluctuations are reduced enough that the liquid in the cell cools again.

¹⁴Most dissipation induced by vibrations arises when the magnet and nuclear stage move with respect to each other, which creates eddy current heating.

Pomeranchuk cell.

It seems that the texture, where the order parameter is given enough time to grow into the flare-out configuration stretched over the sample, is incredibly stable. Using the knowledge we have of the magnetic healing length ξ_H , it is clear that other textural configurations must cost less energy. However, to go to this 'new' configuration there should be a transition between the two textures. A spontaneous transition to the uniform texture (as founded by local heating) will coincide with sharp jumps of the $\hat{\mathbf{n}}$ -vector, such transition which will definitely not be appreciated by the bulk-bending free energy, maybe a possible reason why the texture will stay in the flare-out configuration. The dynamics of transitions is in general hard, and in the case of static experiments not much is reported in literature.

The stable flare-out texture gives us a good opportunity to study spin waves over the whole temperature regime. The cylindrical geometry in combination with a diameter of 1 mm gives us a constant (transverse component) potential below temperatures of $0.7 T_c$. This constant potential¹⁵ made it possible to observe how spin waves grow in our sample. Also the relative intensities of the spin waves did not decrease for the higher spin modes, this in contrast with the reported spin waves in similar configurations. This effect is maybe desirable in experiments concerning the dynamics of vortices in such a cylinder, since now the higher modes have too bad signal to noise ratio and no information can be retracted of them.

The spin waves let themselves describe in good agreement as is derived from the spin dynamics in cylindrical symmetry. While we compare the data presuming we had a quadratic potential, which gave the advantage that the model was analytically solvable, we could reconstruct to a large extent the actual potential by comparing the data and theory. Naturally the two potentials did not differ too much, but we could note that (at least for big r) β is proportional with r . This would correspond with a gradually change of the $\hat{\mathbf{n}}$ -vector between the two boundary conditions, a scenario which seems imaginable as an extreme flare-out configuration.

The local heating experiment showed that it was possible to create the uniform texture in our cell, and not unimportant showed to have an average angle close to 63.4° . Good confirmation that the surface-field free energy has strong influence on this texture, and that it is in agreement with theory. This technique may be used to create two different textures close to each other, for which the dynamics or transition between them can be studied.

3.11 Conclusion

In conclusion, with the carefully chosen geometry in combination with low pressures and low magnetic fields, we could make a metastable $\hat{\mathbf{n}}$ -texture. The texture was

¹⁵Most spin wave experiments are done in cylinders with a diameter of few times ours, and often performed at higher pressures. Consequently the ratio between radius and magnetic healing length ξ_H is bigger than in our case, and thus the shape of the potential changes with decreasing temperature. In the analysis of those spin waves the change of ξ_H was considered the most important temperature effect, a temperature dependence we could exclude from our analysis.

3. *Spin waves in cylinder of 1 mm in diameter*

stable and unchanged for a significant part in the pressure and temperature ranges. It functions as a potential to create spin waves, which made it now possible for us to study them for several pressures in exactly the same texture (potential). As this potential (texture) is close to a quadratic one, and this is essentially a two dimensional system, the intensities of all spin wave modes are nearly equal. This is an excellent system to observe the grow of spin waves modes in our cell by increasing the pressure. The theory, which we adapted for our geometries and boundary conditions, could very well describe the found results, making our physical understanding of this phenomenon complete.

Finally we were able to make a textural transition to the in advance expected texture, for which we conclude that the metastable texture could be realized if the growing speed is sufficiently slow.

Chapter 4

Helium-3 in nanosized cylinders

4.1 Introduction

The spatial size of the Cooper pairs corresponds to its coherence lengths as given by equation (1.33) and (1.34). Sizes could be regulated by changing the pressure and/or the temperature of the liquid. Values of the coherence lengths for different pressures at zero temperature are given in table 4.1 [84]. If the dimensions of the experimental container are large compared to these lengths the superfluid phases are expected to be the same as in the bulk system. However, if one reduces the size of the container to a few times the coherence length, one can suppress the superfluid behavior. By reducing only one dimension of the container (to the size of a few coherence lengths), hence a slab geometry, one can make a quasi-2D system. This geometry is theoretically considered by several authors, for example [85], [86], [87] and [88], who predicted that the A- or planar-phase [89] is the most stable phase¹ for low pressures at zero temperature. Recent experiments [90] and [91] indeed showed that the found phase in such geometry was A-phase like.

If we consider a geometry with two dimensions reduced, for example a long cylinder with a radius a few times the coherence length, one can expect a quasi-1D system. In such a system the superfluidity is suppressed in two directions. So, the superfluid property is only expected to be in one single direction (in both spin and orbital space), for which the polar state is expected. This state will be described in detail in the next section. The aim of our research is to experimentally investigate if this polar state exists in such cylinders, see section 4.5.2.

¹Slab thickness should be around 300 - 700 nm.

P (bar)	ξ_0^* (nm)
0	50.1
3	32.8
6	25.1
9	20.7
12	18.0
15	16.0
18	14.4
21	13.3
24	12.3
27	11.5
30	10.9

 Table 4.1: Typical values of $\xi_0^*(P)$. $\xi_0^* = \sqrt{3/5} \xi_0$.

4.2 Polar state

The unique feature of the polar state (for the first time described in [72]) is, compared to the other inert states that it is without broken relative symmetry; meaning that \mathbf{S} and \mathbf{L} do not need to be fixed in any relative configuration to minimize the energy. However, as they both have a preferred direction, the broken symmetry of the system is $S_{\mathbf{L}}^2 \times S_{\mathbf{S}}^2 \times U(1)_\phi$. The remaining symmetry is then $U(1)_{S_z} \times U(1)_{L_z}$, for which the order parameter (see section 1.4) is given by

$$A_{\mu j} = e^{i\phi} \begin{bmatrix} 0 & 0 & 0 \\ 0 & 0 & 0 \\ 0 & 0 & 1 \end{bmatrix}. \quad (4.1)$$

The anisotropic energy gap of this state, see figure 4.1, is given by

$$|\Delta_{\mathbf{k}}| = \Delta_0 |\cos \theta_{\mathbf{k}}| = \Delta_0 |\hat{\mathbf{w}} \cdot \hat{\mathbf{k}}|, \quad (4.2)$$

where $\hat{\mathbf{w}}$ is the conventional notation ² of the preferred direction in orbital space of the polar state and Δ_0 the maximal value of the energy gap. At zero temperature the maximal value of the gap is $\Delta_0(0) \approx 2.02k_B T_c$. The average value of the gap is obtained by multiplying Δ_0 with a factor ³ of $\sqrt{2/3}$. The temperature dependence of this anisotropic energy gap is expected to be similar to the case of the A-phase. The maximal value of the energy gap in the case of the A-phase [92] has the same temperature dependence as the B-phase, which is described in section A.2.

²For the Polar state it is conventional to notate the preferred direction of the order parameter in orbital space as $\hat{\mathbf{w}}$, which is notated as $\hat{\mathbf{l}}$ in the A-phase.

³The square root of the average of $\cos^2 \theta$.

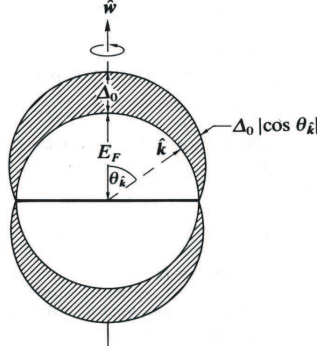


Figure 4.1: Scheme of the energy gap of the polar-phase in k -space indicated by the shaded area. The gap has rotation symmetry around \hat{w} and vanishes along the equator line. Ratio of Fermi energy E_F and the gap Δ_0 is not to scale. Figure is taken from [19].

4.2.1 Polar state in cylinders

Long narrow tubes would be an ideal candidate to expect a polar state. If the radius is limited to a few times the coherence length, two components of the order parameter are reduced enough that the polar state is energetically the expected phase. As in the polar state the energy is not determined by any relative position between the spin and orbital components, the preferred directions are determined by the geometry of the container and external magnetic field. In the case we deal with an external magnetic field parallel to the cylinder axis, we expect that the spins \mathbf{S} will align along the axis of the cylinder (magnetic field) and the orbital component \mathbf{L} perpendicular to the surface of the cylinder.

The (relatively) simple geometry makes it possible to predict in which conditions we would expect the polar state [86] [87] [93]. Barton and Moore calculated, for pores and cylinders with a radius R of the same order of magnitude as the coherence length, which phases could be expected. Two extreme conditions were considered: with complete diffuse scattering and with fully specular scattering boundary conditions. Cooling from the normal Fermi liquid phase, the following sequences are expected:

Diffuse scattering:

normal $\underline{2nd}$ polar $\underline{2nd}$ mixed axial $\underline{1st}$ transverse axial $\underline{1st}$ B-phase.

Specular scattering:

normal $\underline{2nd}$ polar $\underline{2nd}$ axial $\underline{1st}$ B-phase.

The order of each phase transition is indicated above the arrows. The variation of different phases is due to the competition of the terms in the free energy, which

Transition	α
normal \rightarrow polar	2.40
polar \rightarrow mixed axial	3.36
mixed axial \rightarrow transverse axial (highest estimation)	3.83
mixed axial \rightarrow transverse axial (lowest estimation)	6.04

 Table 4.2: Estimation values of α for different transitions.

consist of bulk, surface and strain energy terms. For glass cylinders one would expect to be in the diffuse scattering regime, for which the authors have calculated the transition temperature as a function of the radius of the pores. The general expression they found is given by

$$T = T_c \left(1 - \frac{3}{5} \left(\frac{\xi_0}{R} \right)^2 \alpha^2 \right), \quad (4.3)$$

where α is a dimensionless parameter depending on the phase, as listed in table 4.2. The mathematical complexity and increasing uncertainty of certain parameters at lower temperatures made it impossible for the authors to estimate one α corresponding to the mixed axial \rightarrow transverse axial transition, and they were unable to determine it for the transition between the transverse axial \rightarrow B-phase. However, as the coherence length is decreasing with further cooling, one expects to end in the (distorted) B-phase. By combining equation (4.3) and table 4.2 we can plot the expected transition temperatures as function of the ratio R/ξ_0 , see graph 4.2.

All these calculations were performed in zero magnetic fields. A sufficiently large magnetic field would change the phase diagram and their sequences. Than the first expected phase will not be the polar-phase, but the so called β -phase⁴. As we are interested to find the polar phase, we apply a relatively low field (as in the case of the experiments described in chapter 3) to probe the superfluid with our NMR techniques.

An alternative calculation for the phase diagram for small cylindrical channels comes from Li and Ho [86]. Their calculations are based on the studies of Fishmann and Privorotskii [94] and Muzikar [95]. They found that in the case of sufficiently small channels the state with a polar core is most favorable. Their phase diagrams are calculated for long cylindrical channels with a radius R of 300 nm. Here they considered axial symmetric states, as it is believed that one of those should be the most favorable state.

Two 'confined conditions' are considered: $R \gg \xi(T)$ and $R \approx \xi(T)$, which are referred as 'mildly' and 'strongly' confined limits, respectively. As one goes from the strong to the mild regime, a transition from A polar state to B-like state should occur. They also included in their calculations the two scattering regimes (boundary conditions), specular (ideal mirror) and diffuse reflection, for which they constructed the accompanying phase diagrams.

⁴In this phase only up-up pairs are non-zero.

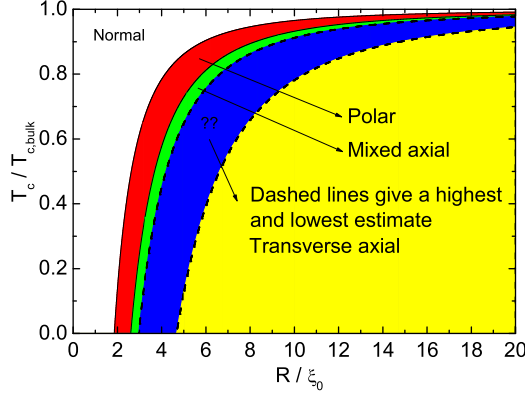


Figure 4.2: The reduced transition temperature of the expected phases in pores/cylinders as function of reduced radius. The red area indicates where the polar state is expected to be stable. The green area indicates the region where the mixed axial state is calculated to be the most favorable phase. Somewhere in the blue area the transition between mixed axial and transverse axial should occur. The transition temperature to the B-phase is unclear, but should happen at the lowest temperatures in the yellow area.

The boundary conditions are described in detail by Ambegaokar, deGennes and Rainer [89], who regard the spatial variations in the order parameter. Ambegaokar *et al.* consider the dominating term (quadratic term) of the gradient free energy density which is split into the longitudinal and transverse components (here the surface energy terms are neglected).

$$F_{grad} = \sum_p \left\{ \frac{1}{2} K_L |\nabla \cdot \mathbf{A}_p|^2 + \frac{1}{2} K_T |\nabla \times \mathbf{A}_p|^2 \right\}, \quad (4.4)$$

where the vector \mathbf{A}_p has components A_{pi} . K_L and K_T are two positive coefficients and are related to the coherence length:

$$K_T = \frac{3}{5} \xi_0^2, \quad K_L - K_T = \frac{6}{5} \xi_0^2. \quad (4.5)$$

From which we define the longitudinal coherence length ξ_L and transverse coherence length ξ_T :

$$\xi_L^2 = 3\xi_T^2 = \frac{9}{5} \xi_0^2 \frac{T_c}{T_c - T}. \quad (4.6)$$

These authors solved the specular scattering problem for a (xy) -plane, with the ^3He only at one side ($z > 0$). The transverse components are parallel and the longitudinal component perpendicular to the plane.

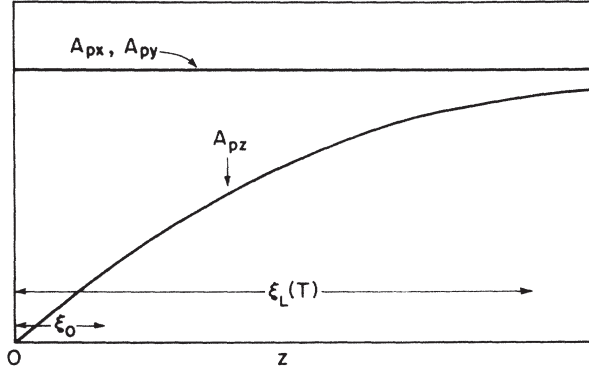


Figure 4.3: The transverse (A_{px} , A_{py}) and longitudinal (A_{pz}) components of the order parameter near a specular reflecting wall. Figure is taken from [89].

The most general solution at T_c is then:

$$A_{pi} = \text{const} \cdot (b_i + z) \quad (z \gg \xi_0), \quad (4.7)$$

which is asymptotically linear in z . For z near zero a more detailed calculation is needed to find the correct value of the extrapolation length b_i . If one considers the specular reflection at the wall, the solutions become:

$$A_{px} = A_{py} = \text{const}; \quad A_{pz} = \text{const} \cdot z. \quad (4.8)$$

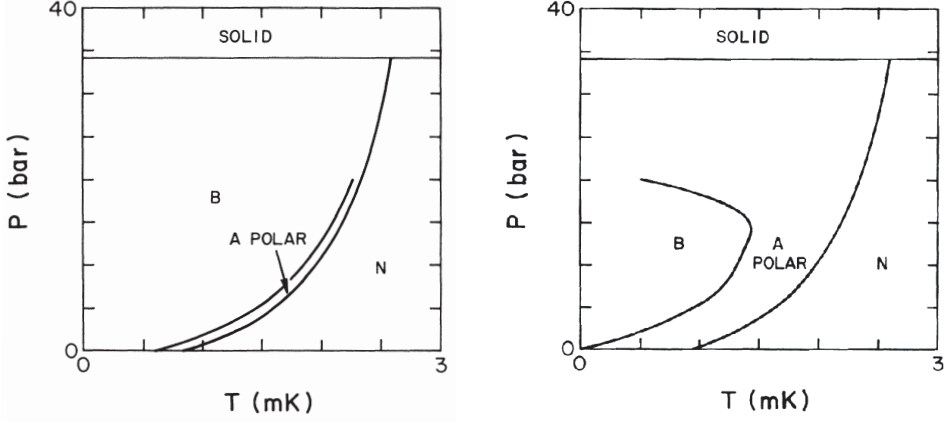
The transverse components stay constant in the container, while the longitudinal component disappears at the wall. Both characteristics are plotted in figure 4.3.

In the case of diffuse reflection, the (transverse) components are reduced by a factor of $\xi_0/\xi(T)$. Here the longitudinal component still vanishes at the wall. Different is that the transverse order parameter components, at (and near) the transition temperature (of bulk), are zero at the wall (giving the reduction of the bulk T_c). However, for lower temperatures the transverse components get a finite amplitude (at the walls) again.

While the behavior of the components of the order parameter are derived in a semi-infinite volume, for which one component (longitudinal) vanishes at the wall, the analogy for a long cylinder is equivalent, and as one can imagine, not one but two components will vanish at the wall.

The reduction of the components of the order parameter, for geometries with the dimension of the order of the coherence length (e.g. slab geometries or small cylindrical channels), makes the B-phase unstable. If all the components, except one, are reduced, one intuitively can understand that the order parameter of the B-phase (1.15) should change to the polar phase (4.1).

The calculated (by Li and Ho) phase diagrams for long cylinders of radius R of 300 nm are plotted in the figures 4.4(a) and 4.4(b), for both boundary conditions:



(a) The phase diagram of ^3He in a cylinder of radius $R = 300$ nm for diffusive boundary condition.

(b) The phase diagram of ^3He in a cylinder of radius $R = 300$ nm for specular boundary condition.

Figure 4.4: Figures taken from [86].

diffuse and specular, respectively. In contrast to slab geometries [86] the phase diagrams for the different boundary conditions are very different in the one-dimensional cylindrical geometry (the A-polar state exists in much wider region). In both cases the polar component is the most dominant part of the order parameter, which is mainly constant for specular scattering, but strongly suppressed for diffuse scattering. Also the temperatures at the phase boundary, separation between the normal and A-polar phase, is suppressed compared to the bulk situation for diffuse scattering. This suppression is given by:

$$T(P) = T_c(P)[1 - (\xi_0(P)/R)^2(1 + \pi^2/4)/(1 - 4/\pi^2)], \quad (4.9)$$

where T_c is the critical temperature of the bulk phase diagram. For specular boundary conditions the critical temperature is not reduced ($T(P) = T_c(P)$).

4.3 Photonic crystal fibers

To be able to measure a possible polar state one needs a cylinder with a diameter of roughly ten times the coherence length of the superfluid. In general it is not trivial to fabricate long cylinders with diameters of few hundred nanometers. To approach the semi one-dimensional geometry for superfluid helium-3, porous media have been used, see for example [96] and [97]. While it was possible to make pores with an average diameter of a few times the coherence length, the variance between them was rather high. Another problem is that the thickness of those samples was rather small (smaller than 1 mm). This made it impossible to perform a measurement which gives a direct and clean signal from the pores. Nevertheless, NMR, heat conducting, oscillation and sound experiments were performed on those samples, from which the signal of the pores needed to be extracted from the bulk signal. These indirect measurements and the fact that those semi one-dimensional samples were not isolated from the bulk, made interpretations not always easy and increase the uncertainty of the results.

In another branch of our physics community, namely optics, they started to produce photonic crystal fibers (PCF) [98] [99]. The PCF also known under the terms: holey fiber, hole-assisted fiber, microstructure fiber, or micro structured fiber, is an optical fiber which obtains its waveguide properties from an arrangement of very tiny and closely spaced air holes, which go through the whole length of fiber. These holes were made from larger capillaries of which, with stacking tube techniques, kilometer long capillaries could be produced with roughly equal holes (diameter) sizes over the whole length.

As in time the diameters of the holes (started in high micrometer regime) reduced, it became an interesting size for us when the group of Russell [100] was able to enter the nanometer regime⁵. It was the first time that long cylinders with inner diameters of ~ 540 nm could be made. Picture 4.5(a) shows a SEM⁶ image of the cross-section of the fiber as received by the manufacturer. Here we see the channels in the fiber surrounded by a coating with a total diameter of $100 \mu\text{m}$. In total every fiber has 324 channels, which are arranged in a honeycomb structure spaced $\sim 1 \mu\text{m}$ from each other. Their diameters vary between 250 to 950 nm, see the distribution function of the diameters in figure 4.6. Except of the holes at the corners of the honeycomb structure, the channels look very circular, see figure 4.5(c) for a close up. Also the axial direction of the channel, see cut through of the fiber in figure 4.5(d), looks very smooth and continuous on the resolution of the SEM (for more details about the roughness, see section 4.3.1).

⁵Initially the group of Russell provided us this fiber. Later on the procedure was commercialized and produced by a company in Denmark: Crystal Fibre A/S [101].

⁶All the SEM images were scanned by the FEI Nova 200 NanoSEM.

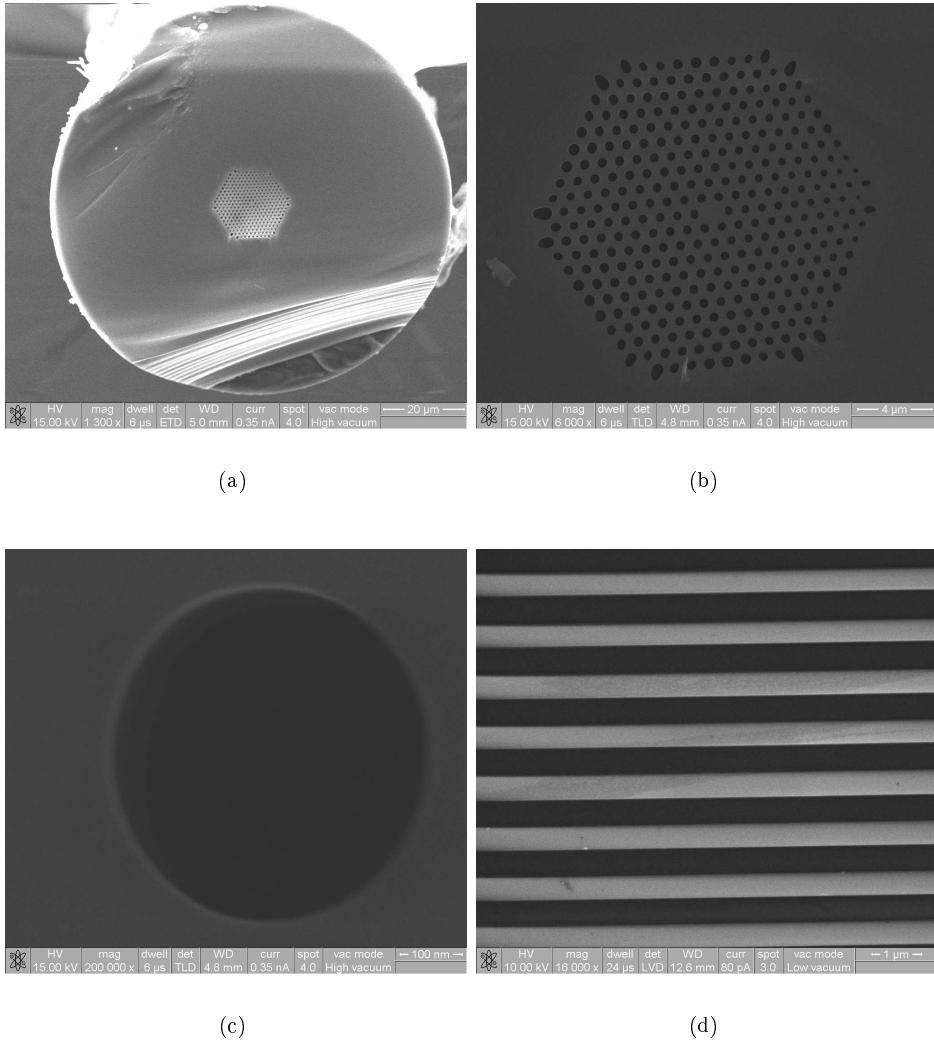


Figure 4.5: SEM images of the photonic crystal fiber, SEM images were scanned with the FEI Nova 200 NanoSEM. (a) Cross-section of the fiber, the total diameter (including glass coating) is $100\ \mu\text{m}$. The central core is $20\ \mu\text{m}$. (b) Zoom of the central core. Here the 324 channels are arranged in a honeycomb structure, with a distance of $1\ \mu\text{m}$ between them. The diameter of the channel is around $540\ \text{nm}$. (c) Cross-Section of one channel. The image looks very circular, for which the channels can be considered very cylindrical. (d) Cut through along the axis of the fiber; on the resolution scale of the SEM the channels look very straight without variation in the diameter.

According to the SEM results, it is clear that the channels in the fiber are very

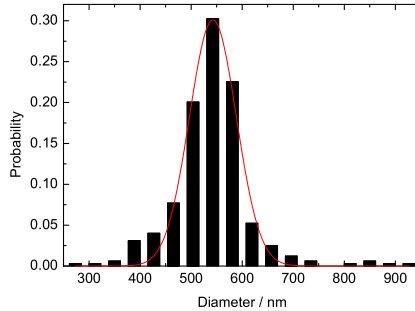


Figure 4.6: Distribution of diameters of the channels in one fiber. The distribution is fitted with a Gaussian (red line). The mean μ is 543 nm and the standard deviation σ is around 46 nm.

cylindrical. However, as is shown in figure 4.6 there is some distribution in the diameter of these channels. Desirable is that the standard deviation is as small as possible, but we are limited by the production process of these fibers. The mean μ (diameter) of the channels is 543 nm, with a standard deviation (σ) of 46 nm. As one will expect certain kinks in the resonance frequency shifts in the NMR spectrum (this will be described in the following sections), the distribution in the diameters will smoothen out these kink effects.

A more important issue is that one needs enough ^3He atoms to detect any NMR signal. As one can see from figure 4.5(a), the coating of such fiber is (relatively) enormous, which will result in a very low filling factor for the NMR experiment. The first concern was to etch as much coating as possible. The coating is made of quartz glass (SiO_2), which can be etched by hydrofluoric (HF) etching. The etching and the procedure was as follows:

- The photonic crystal fibers (PCFs) were cut into pieces of approximated 7.5 cm.
- Both ends of the PCFs were closed by the stycast 1260, were the capillary action sucks the stycast into the channels for maximally 5 mm.
- Fibers were etched with HF solution (HF:H₂O=10:1) for 30 minutes. Outside diameter of the PCFs was reduced to 30 μm . The stycast at the ends of fibers prevented any etching inside the channels.
- Etched PCFs were cleaned intensively with distilled water.
- The PCFs were dried in oven for 30 minutes at 100 °C.
- Ends of the PCFs were cut for 5 mm to remove the nanochannels filled with stycast 1260.

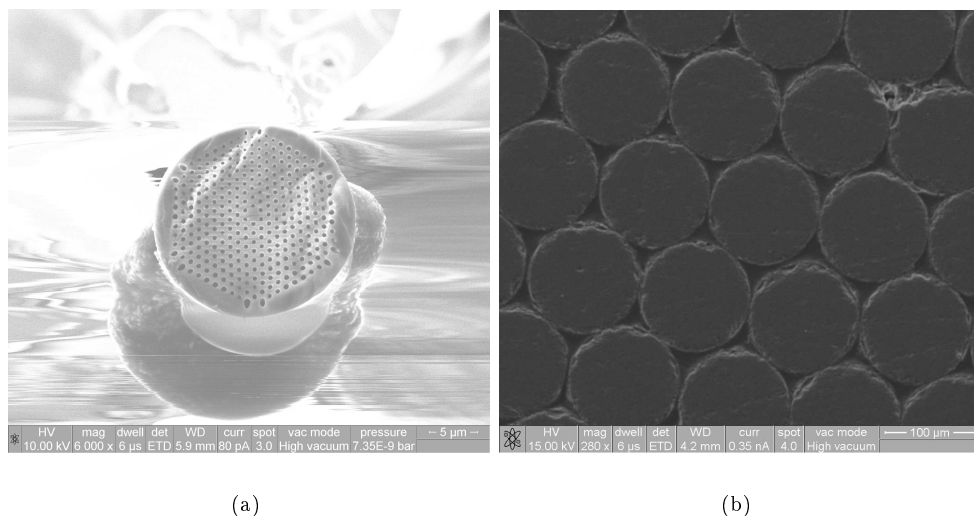


Figure 4.7: (a) Photonic crystal fibers after HF etching. In this particular case the diameter is reduced from 100 to 20 μm . (b) Bundle of fibers glued together with stycast 1260, the packed could be made so tight that is close to honeycomb structure.

The etching decreases the outside diameter significantly, as can be seen in figure 4.7(a). To increase the filling factor for the NMR experiments these fibers were bundled together. This bundle is formed inside a PEI cylinder with inner diameter of 1 mm (Figure 2.1, the red part). The procedure was as follows:

- The PCFs were cleaned in pure CH_3OH (methanol) under ultrasonic vibration, in the same time all of PCFs were sunk into the PEI cylinder. As the etching increases the static charge on the fibers, the methanol helped to shuffle them into the PEI cylinder.
- To evaporate all the CH_3OH (in the channels and between the PCFs) the PEI capillary was put in an oven for 24 hours at 100 $^\circ\text{C}$.
- To fill the spaces between the fibers some drops of stycast 1260 were put on the PCFs in the PEI capillary. Again the capillary action sucks maximally 5 mm into the nanochannels. However, the rest of the stycast was, due to the surface tension forces, sucked into the spaces between fibers.
- The bundle was dried at room temperature for 24 hours, after that another full day in the oven at 70 $^\circ\text{C}$.
- Both ends of the bundle were cut for 5 mm and examined in SEM. The results showed that the nanochannels were opened and distributed (close to) in honey-

comb structure, see figure 4.7(b). No open space was visible between the fibers or between the fibers and the surface of the PEI cylinder.

- Flow rates were measured (with helium and leak detector) to confirm the total cross-section of the channels of the bundle.
- Place (glue) the PEI (including bundle of fibers) in the experimental cell (see figure 2.1), and close the top part of the bundle with stycast 1260.
- Final leak tests were done at liquid nitrogen and liquid helium temperatures.

Despite the effort to put as many channels (fibers) together, the total volume is still very small. The total volume of the channels is around 1.5 % compared to the empty PEI cylinder with inner diameter of 1 mm. Then the total amount of ^3He atoms which we could detect with our NMR probes should be around 1.4 μmole . This amount, in combination with our weak coupling read-out system (see section 2.4), should be sufficient to get NMR signals with sufficient SNR at our desirable magnetic field (\mathbf{B}_0) and bandwidth.

4.3.1 Roughness

The roughness of the channels is important to know how diffuse or how close one is to the specular boundary conditions. The SEM images already exposed that the roughness of these channels is smaller than the resolution of the SEM (~ 5 nm), and for better resolution the surface roughness measurements were performed with an atomic force microscope (AFM). A method was invented to cleave the PCF along the axis without damaging the surface structure inside the nanochannels, allowing us to characterize the morphology of the nanochannels in the PCF. A multi-wall carbon nanotube (MWCNT) mounted at a commercial AFM probe and a super sharp silicon tip were used to characterize the wall roughness in the nanochannels.

Introduction

In order to perform roughness measurements one should first consider two key problems: how to describe a rough surface accurately and how to detect and measure a rough surface. A (close to) random rough surface can be described mathematically. If a surface roughness can be described by a (Gaussian) random process, then the statistical parameters describing the surface height variation can be completely defined based on its height distribution and autocorrelation function, that is, the surface is totally determined in a statistical sense. A lot of work has been done to derive surface roughness descriptions that can be practically used for both one dimensional ($1D$) and two dimensional ($2D$) situations [102], [103], [104], [105], [106], [107], [108]. Gaussian distributions have been experimentally shown to be valid for many engineering surfaces [108]. An alternative assumption is that the autocorrelation function has an exponential form, which has also been verified experimentally [104], [105], [106]. It is well known that both height parameters and spatial functions are needed to describe the height distribution and textures of rough surfaces [109]. Autocorrelation function and autocorrelation length (λ_0) have been widely used in surface-related studies [110], [111], [112], [113], [114] to provide spatial information in addition to amplitude parameters, such as root mean square (RMS) roughness.

The mathematical tools used for the analysis of a random rough surface, which can be described mathematically as $z = z(x, y)$, where z is the surface height of a rough surface with respect to a smooth reference surface defined by a mean surface height and \mathbf{r} is the position vector on the surface. One of the main characteristics of a random rough surface is the distribution function (one dimensional distribution function), $p(z)$. The meaning of $p(z)$ is that the probability of a surface height between z and $z + dz$ at any point on the surface is $p(z)dz$. The distribution $p(z)$ is a non-negative function of z and is normalized such that

$$\int_{-\infty}^{\infty} p(z)dz = 1. \quad (4.10)$$

The height distribution function provides a complete specification of the random variable $z(\mathbf{r})$ at a position $\mathbf{r} = \mathbf{r}(x, y)$. Although different rough surfaces may have different height distributions, the most generally used height distribution is the Gaussian

height distribution,

$$p(z) = \frac{1}{\sqrt{2\pi\sigma^2}} e^{-\frac{z^2}{2\sigma^2}}, \quad (4.11)$$

due to its mathematical simplicity and its place in the central limit theorem of the sum of large amount of random variables, where σ is the RMS deviation. The σ describes the fluctuations of surface heights around an average surface height. Larger σ means a rougher surface, under the condition that other roughness parameters stay the same. Sometimes the average roughness σ_{avg} is used to describe surface roughness and is defined as the arithmetic average of height z ,

$$\sigma_{avg} = \int_{-\infty}^{\infty} |z - \bar{z}| p(z) dz. \quad (4.12)$$

Usually people do not consider higher-order moments, because the 1st order moment \bar{z} and the 2nd order moment σ^2 are sufficient to characterize surface roughness for most purposes. However, higher order moments can give more information about the surface height distribution, and sometimes one needs higher order moments to differentiate the surface in more detail. The most important higher order moments are the 3rd and 4th order moments. The third order moment defines the skewness of surface height S_{sk} ,

$$S_{sk} = \frac{1}{\sigma^3} \int_{-\infty}^{\infty} z^3 p(z) dz. \quad (4.13)$$

Note that the S_{sk} is dimensionless in contrast to the RMS roughness, which is in units per length. The 4th order moment defines the kurtosis of surface height S_{ku} ,

$$S_{ku} = \frac{1}{\sigma^4} \int_{-\infty}^{\infty} z^4 p(z) dz. \quad (4.14)$$

Kurtosis is also a dimensionless quantity.

The height distribution function only describes the statistical properties of random variables of a random field at individual positions. Different rough surfaces can have the same height distribution $p(z)$ and σ . In order to differentiate the spatial differences, one needs to know the connection of the random field $z(\mathbf{r})$ at positions \mathbf{r}_1 and \mathbf{r}_2 . To do that, the joint distribution probability density function $p_j(z_1, z_2; \mathbf{r}_1, \mathbf{r}_2)$ of $[z(\mathbf{r}_1), z(\mathbf{r}_2)]$ is introduced, and it satisfies:

$$\int_{-\infty}^{\infty} \int_{-\infty}^{\infty} p_j(z_1, z_2; \mathbf{r}_1, \mathbf{r}_2) dz_1 dz_2 = 1, \quad (4.15)$$

$$\int_{-\infty}^{\infty} p_j(z_1, z_2; \mathbf{r}_1, \mathbf{r}_2) dz_1 = p(z_2), \quad (4.16)$$

$$\int_{-\infty}^{\infty} p_j(z_1, z_2; \mathbf{r}_1, \mathbf{r}_2) dz_2 = p(z_1), \quad (4.17)$$

where $p(z_1)$ and $p(z_2)$ are called the marginal distribution of $p_j(z_1, z_2; \mathbf{r}_1, \mathbf{r}_2)$, and for a homogeneous random field, $p(z_1) = p(z_2) = p(z)$. In general, $p_j(z_1, z_2; \mathbf{r}_1, \mathbf{r}_2)$ is not only related to the height distribution, but also to the correlation of heights between two separated positions.

The most important statistical characteristic of a joint distribution $p_j(z_1, z_2; \mathbf{r}_1, \mathbf{r}_2)$ is the auto-covariance function,

$$G(\mathbf{r}_1, \mathbf{r}_2) = \int_{-\infty}^{\infty} \int_{-\infty}^{\infty} z_1 z_2 p_j(z_1, z_2; \mathbf{r}_1, \mathbf{r}_2) dz_1 dz_2, \quad (4.18)$$

or the autocorrelation function,

$$R(\mathbf{r}_1, \mathbf{r}_2) = \frac{G(\mathbf{r}_1, \mathbf{r}_2)}{\sigma^2}. \quad (4.19)$$

For homogeneous isotropic rough surfaces we consider $G(\mathbf{r}_1, \mathbf{r}_2)$ and $R(\mathbf{r}_1, \mathbf{r}_2)$ only depending of the distance between \mathbf{r}_1 and \mathbf{r}_2 , hence

$$G(\mathbf{r}_1, \mathbf{r}_2) = G(|\mathbf{r}_1 - \mathbf{r}_2|) = G(\rho), \quad (4.20)$$

and

$$R(\mathbf{r}_1, \mathbf{r}_2) = R(\rho), \quad (4.21)$$

where, $\rho = |\mathbf{r}_1 - \mathbf{r}_2|$. The quantity is the translation and sometimes is called a lag. The autocorrelation function $R(\lambda)$ has the following properties:

- $R(0) = 1$
- $R(-\lambda) = R(\lambda)$
- $|R(\lambda)| \leq R(0)$
- $z(r)$ and $z(r + \lambda)$ are independent from each other for the limit $\lambda \rightarrow \infty$; for the limit for $\lambda \rightarrow \infty$ $R(\lambda) = 0$

The autocorrelation length λ_0 of an autocorrelation function is usually defined as the value of the lag length at which the autocorrelation function drops to $1/e$ of its value with respect to zero lag, i.e. $R(\lambda_0) = 1/e$. For a random rough surface, the information of the correlation functional represents a good description of surface morphology.

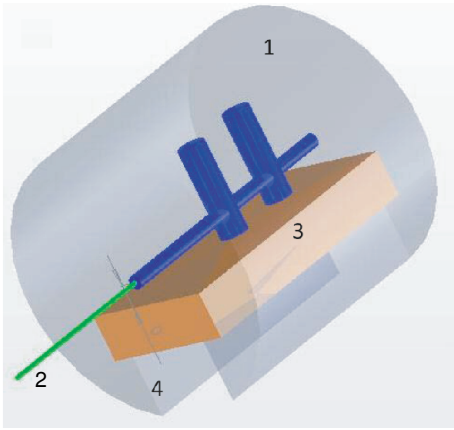
Preparation

In order to open the channels along the axis of the fiber, the fiber was glued into the holder, see figure 4.8(a). The whole holder was immersed in liquid nitrogen, and after thermalisation the holder was quickly taken to room. The difference in thermal expansion between the grey Araldite and metal and the predefined groove breaks the cylinder along the axis. This result made it possible to perform AFM and SEM measurements on the inside of the fiber.

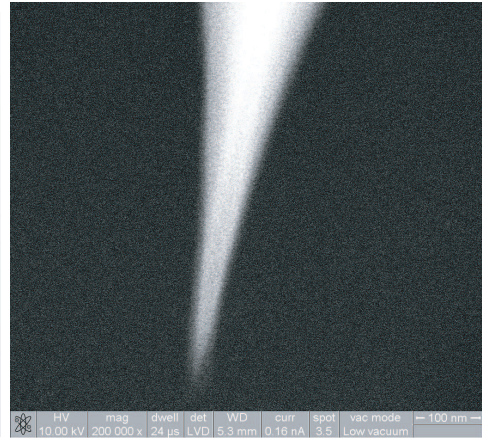
As the open PCF samples are not (relatively) flat (curvature of the cylinder), conventional commercial silicon nitride AFM tips would not be suitable. These tips are too wide compared to their length, and for this reason would not be suitable to obtain a good profile from inside the channels. This concern made us use two different kind of AFM tips, the super sharp silicon tip and multi-wall carbon nanotube tip. Both are relatively long compared to their width, and their results are compared with each other. The used atomic force microscopy was the: Nanoscopy III Multimode AFM, Digital Instruments/Veeco Instruments. The AFM measurements were performed in contact and/or the non-contact/tapping mode.

The super sharp silicon non-contact/tapping mode AFM probe [115] is shown in figure 4.8(b). The tips have a high aspect ratio, its radius of curvature is 2 nm, the half cone angle at 200 nm from the apex is smaller than 10° , and the typical aspect ratio at 200 nm from the tip apex is of the order 4:1. As shown in the Figure 4.8(b), the length from the apex of the tip to the point with a radius less than 100 nm and is longer than 400 nm, so that the apex of the tip can reach to the bottom of the channel.

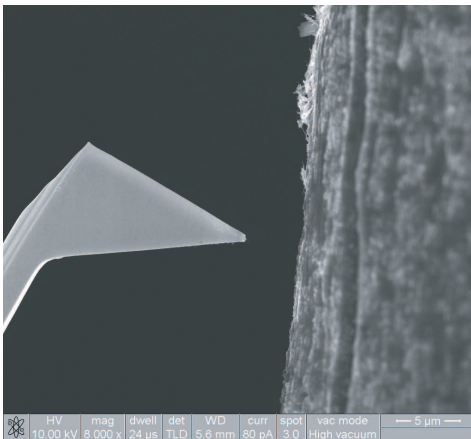
The used multi-wall carbon-nanotube (MWCNT) AFM tip was home made by the group of Frenken, Oosterkamp and Rost [116]. First the multiwall carbon nanotube must be placed on the end of silicon AFM tip by using a custom-built nanomanipulator assembly inside a scanning electron microscope (FEI Nova 200 NanoSEM). This method allows retrieving a single MWCNT from an electrode covered with MWCNTs and attached (by gold coating), see figure 4.8(c), to a commercial AFM probe (Olympus AC240TS, nominal resonant frequency 80 kHz, sputter coated with 5 nm of Molybdenum-Germanium followed by 70 nm of Gold). The fabricated multiwall carbon nanotube AFM probe, see figure 4.8(d), had a length of 320 nm, and a diameter of 30 nm with an apex less than 5 nm.



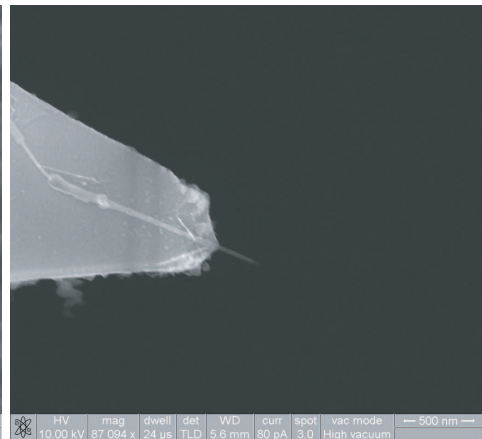
(a) Holder to break the cleaved fiber along the axis of photonic crystal fiber. (1) Grey araldite. (2) Position to cleave the photonic crystal fiber by thermal expansion. (3) Metal bar. (4) Pre-crack groove.



(b) Super Sharp Silicon Noncontact Tapping mode - High Resonance Frequency Commercial atomic force microscope probe.



(c) Mounting multi-wall carbon nanotube on the top of the AFM probe.



(d) Homemade AFM carbon nanotube probe used for visualization and characterization of channel wall roughness of the photonic crystal fiber.

Figure 4.8:

Results and discussion

Atomic force microscopy (AFM) made it possible to create high resolution images of non-conductive surfaces. In contact AFM a cantilevered probe is slid over the surface of the sample. The deflection of the cantilever is a measure of the force working on the probe. A laser beam bounces from the back of the cantilever to a photodiode enabling the determination of the deflection while a piezo moves the sample under the tip so that it slides over the surface. Contact mode is mostly done using silicon nitride tips. In tapping mode AFM the cantilevered probe oscillates close to its resonant frequency tapping the surface with the probe at the lowest point of the oscillation. The oscillation of the cantilever is monitored while a piezo moves the sample under this oscillating probe. A feedback loop ensures that the oscillation of the cantilever is kept constant and thereby the tapping force. The resolution of the AFM is 0.1 to 0.2 nm laterally, and 0.1 nm vertically.

An example of the AFM image, which mapped the whole curvature of the channel, is shown in picture 4.9. However, as we are interesting to find the roughness and correlation lengths of such a channel, scan sizes this size are not suitable for analysis. First of all, while both tips have the right shape to scan at the bottom of these channels, it can give problems when we scan close to the edges. Secondly, step sizes of the AFM are digitally controlled. The step sizes are determined by a 2×12 bit system⁷ (for the X and Y direction), meaning that long scan ranges will increase the step sizes. This can obscure the interpretation of the roughness of the channel, and/or can miss the existence of a (short) coherence length. For these two reasons scans are made in the middle of the channel, and are kept relatively small (100 to 200 nm) in one direction (perpendicular to the axis of the channel). The scan direction along the axis of the channel was varied between 100 to 1600 nm, so that any coherence length at different length scales can be studied.

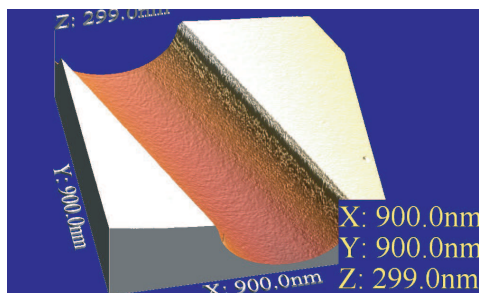
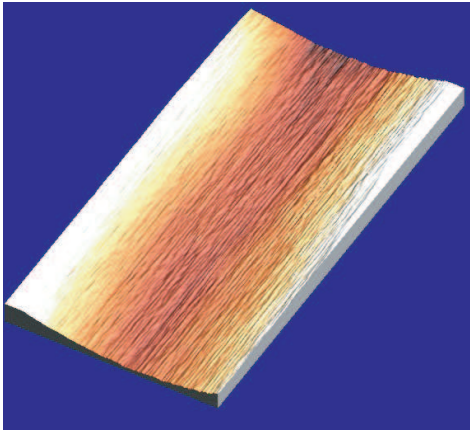
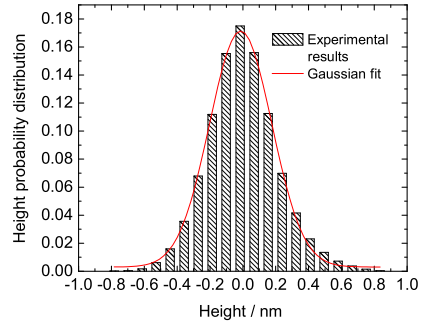


Figure 4.9: AFM images measured by a silicon super sharp tip. Scan size of $900 \times 900 \text{ nm}^2$.

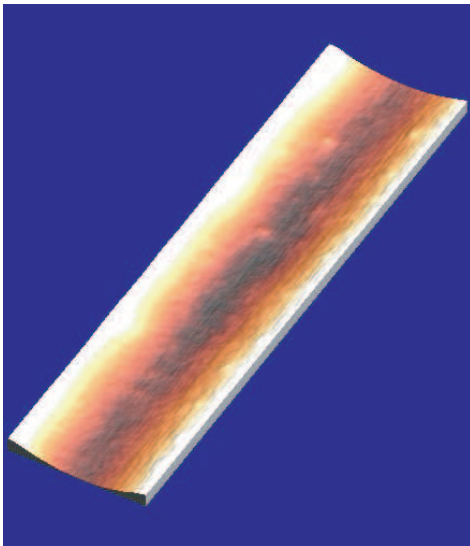
⁷The XY position is constructed by 512×512 matrix (9 bits in each direction). Leaving 3 bits for the Z coordinate.



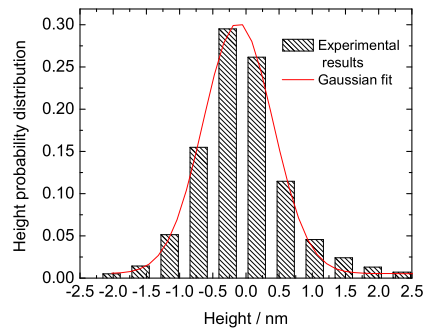
(a) Example of an AFM image of the inside of a photonic crystal fiber with a silicon super sharp tip. Scan size is $200 \times 100 \text{ nm}^2$.



(b) Height probability distribution function made of one of the surface profiles taken from figure 4.10(a).



(c) Example of an AFM image of the inside of the photonic crystal fiber with a multi-wall carbon nanotube tip. Scan size is $800 \times 200 \text{ nm}^2$.



(d) Height probability distribution function made of one of the surface profiles taken from figure 4.10(c).

Figure 4.10:

Probe type	Scan size nm × nm	2σ nm	$2\sigma_{avg}$ nm	S_{ku}	S_{sk}	λ_0 nm
Multi-wall carbon nanotube tip	1600 × 200	0.95	0.61	22.90	2.88	25.76
	800 × 200	0.89	0.63	10.61	1.84	22.88
	400 × 200	0.73	0.52	5.75	0.57	23.76
	200 × 200	0.62	0.43	5.67	0.56	12.69
Super Sharp Silicon tip	100 × 100	0.82	0.56	8.16	-1.56	2.95
	200 × 50	0.75	0.56	4.89	0.37	16.14
	200 × 100	0.34	0.26	4.80	0.31	12.91
	200 × 200	0.86	0.65	8.70	0.22	16.27
	800 × 100	0.81	0.62	4.91	0.64	26.76

Table 4.3: Statistical roughness parameters of the channels, for different scan ranges and AFM tips.

Typical results of AFM scans of both tips are plotted in figure 4.10 together with one of the height probability distribution functions corresponding with the surface profiles, which are represented by a Gaussian. For both tips and all different scan ranges the statistical parameters are obtained according to equations (4.11), (4.12), (4.13), (4.14), (4.18) and (4.19). The acquired parameters are listed in table 4.3, and are averaged from several measurements at different places from the same sample. Comparing the parameters we observed that the amplitude of the roughness (σ) in all cases is smaller than 0.5 nm. As one can already see by eye in figures 4.10(b) and 4.10(d) the height distribution has a Gaussian form, meaning that the roughness is close to a homogenous (random) distribution. This is confirmed by the value of the kurtosis S_{ku} , a perfect random surface has an S_{ku} of 3. Our values are still reasonable close to that number, however as they are larger than 3, it indicates a leptokurtic distribution (more peaked than a normal distribution). This is also seen back in the skewness S_{sk} , which should be zero in the case of a perfect Gaussian distribution function. While the values of the parameter are relatively close to zero, they are almost all positive which indicates (again) to peakness in the channel. However, it is questionable if the roughness is really more peaked than dipped. Reasonable is to believe that it can be a feature of the measurement. Namely, it is always harder for a tip to reach the bottom of a valley than the top. Nevertheless, we consider our channels pretty homogenous with a roughness amplitude smaller than 0.5 nm, as is shown by the performed measurements of all scan sizes, and this result seems independent of the used tip.

Another phenomenon observed in the measured data, which is most probably not a real feature, is that for the longer scan ranges the kurtosis and skewness seem to increase. The feedback mechanism works in all circumstances (scan sizes) with the same speed, meaning that for longer scan ranges the feedback gets relatively slower. This was problematic for the super sharp silicon tip, often the tip broke

as the feedback could not prevent touching/smashing⁸ the tip into the surface, the reason why the longest scan sizes are not performed with this tip. As the multi-wall carbon nanotube is a bit smaller and less fragile, longer scan sizes could be performed, however the problems in the feedback mechanism for such 'long' scans were the same. This made us believe that some artificial results are crept in our data for the longer scan sizes. On the other hand it should be mentioned that significantly less scans are made on these scales (once more because of the difficulties it brings with them), for which the error in the (average) value is also higher.

Concerning the correlation length λ_0 , one should realize that some curious features with regard to the autocorrelations function for finite samples can occur. As is pointed out by the authors Ogilvy and Foster [117]: The full exponential height correlation function of a surface profile will only be measured if the sampling interval is less than one tenth of the correlation length λ_0 , and for best rough surface statistics the ratio of surface extent to correlation length must be 60 (or bigger). This is in our case not trivial, as we are always wrestling with the sample interval vs. total scan length. However, our correlation functions, from which we obtained the correlation length, have an exponential behavior. So the acquired (average) coherence length λ_0 , as is put in table 4.3, are obtained by exponential fits. From here it seems that the coherence lengths get longer for increasing scan lengths⁹, which is an indication that we did not scan over long enough distances to extrapolate the real size of the coherence length from the data. However, when we put all data in one graph, see figure 4.11, the coherence length seems to approach a plateau for long enough scan ranges. The phenomenon that one comes closer¹⁰ to the 'real' coherence length of a system by increasing the scan lengths is known, and for example well described in the book of Meakin [118]. The used fit function, the exponential growth¹¹, is given by

$$\lambda_0(x) = -26.49 \exp(0.0038x) + 26.49. \quad (4.22)$$

The data of both tips seem to correspond with each other, and it seems to approach the value close to 26.5 nm. The longest scan range is already close to this value, and as the scan conditions¹² are very close to the condition as determined by Ogilvy and Foster, it is an extra indication that this may indeed be the 'real' value of the coherence length in the channels. This coherence length is most likely induced by the method of production of these fibers and the surface tension of SiO_2 . If any coherence

⁸Except of position problems, the feedback could also bring the tip in oscillation introducing obscure results in the measurements.

⁹Correlations lengths are searched in the directions along the channel axis.

¹⁰In the situation one starts with scan sizes which are not long enough to preview to 'real' coherence length.

¹¹The preference of an exponential growth seems reasonable concerning the behavior of the data, which is supported by the theoretical explanation that such scaling is linear on log-log scales.

¹²If one assumes that the coherence length of 26.5 nm is a 'real' coherence length in our system, then our scan size is more than 60 times the coherence length in case we scan 1600 nm. Also the interval is $1600/512 = 3.125$, which is very close to the one tenth of correlation length ($3.125/26.5 \approx 0.12$). It means that we are very close to the condition to observe the coherence length of the system.

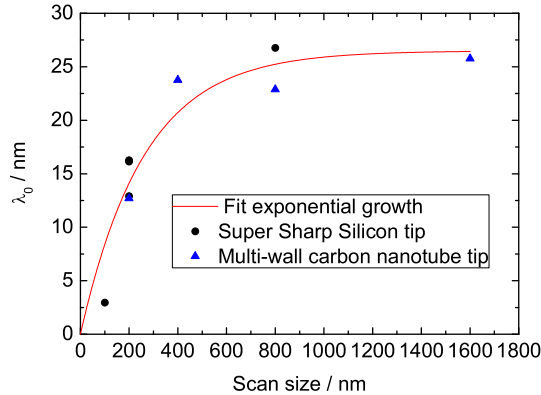


Figure 4.11: Correlation lengths λ_0 as founded by the autocorrelation function as function of scan size. Black circles are correlation lengths obtained from the data with super sharp tips, the blue triangles are obtained with the multi-wall carbon nanotube. Data could be fitted with an exponential growth, and seems to approach a maximal correlation length of 26.49 nm.

at longer scales is present in our systems, then those values will not be detected with our used techniques (limitation of scan size).

Interesting is that both tips describe more or less the same statistical parameters. As all measurements are a deconvolution between tip and sample, it makes the information about the channel more reliable as it is confirmed by two different kinds of tips. It is also, by our knowledge, the first time that roughness measurements are performed on the holes inside the photonic crystal fibers.

4.4 Expected NMR 'fingerprint' in narrow cylinders

4.4.1 A-phase

For educational purposes first the resonance frequency shifts in the bulk A-phase are described. One can derive these shifts in an equivalent way to what was done for the B-phase in section 3.2. The full derivation we will omit, because the results are perfectly described in Leggett's paper [21], from which we quote the solutions of (3.3) as:

$$\Omega_{xx}^2 = 0, \quad (4.23)$$

$$\Omega_{yy}^2 = \Omega_{zz}^2 = \frac{6}{5} \frac{\gamma^2}{\chi_A} g_D(T) \equiv \Omega_A^2. \quad (4.24)$$

The A-phase is very interesting in that it has a *transverse* resonant frequency shift:

$$(\omega_{\perp}^A)^2 = \omega_L^2 + \Omega_A^2, \quad (4.25)$$

and a *longitudinal* resonant frequency¹³:

$$\omega_{\parallel}^A = \Omega_A. \quad (4.26)$$

The (transverse) resonance frequency shift was already observed [35] before the theoretical understanding, and actually started the intensive theoretical studies to anisotropic susceptibility of superfluids.

In the bulk A-phase¹⁴ the dipole energy is minimized when the preferred direction in spin space $\hat{\mathbf{d}}$ is perpendicular to the magnetic field¹⁵ \mathbf{B}_0 (the magnet field of the NMR magnet), but aligned with $\hat{\mathbf{l}}$. The vectors $\hat{\mathbf{l}}$ and $\hat{\mathbf{d}}$ parallel or anti-parallel is referred as dipole-locked, for which (4.25) is the solution. The more general solution, valid for the dipole unlocked regions due to surface and/or topological defects, is given by [22]:

$$\omega = \omega_L + \frac{\Omega_A^2}{2\omega_L} \cos(2\Theta(\mathbf{r})), \quad (4.27)$$

with $\Theta(\mathbf{r})$ the angle between the $\hat{\mathbf{l}}$ and $\hat{\mathbf{d}}$ vector.

4.4.2 Polar-phase

As in the polar-phase the orbital space $\hat{\mathbf{w}}$ and spin space $\hat{\mathbf{d}}$ have only one preferred direction, and in absence of any spin-orbit interaction the vectors do not need to be in any fixed relative configuration to minimize the energy, the dipole energy does not lift the degeneracy [119]. Consequently the $\hat{\mathbf{w}}$ - and $\hat{\mathbf{d}}$ -vector can be parallel or perpendicular or have any other configuration.

Any relative orientation may not be energetically favorable, but as shown by [21] and [120], determines whether the superfluid NMR signal has a longitudinal or transverse frequency component. In the case that the vectors $\hat{\mathbf{w}}$ and $\hat{\mathbf{d}}$ are aligned parallel there is no transverse resonance frequency shift, but a longitudinal resonance can be found at the frequency of

¹³Strictly spoken these solutions are only valid in the so called high field limit, $\mathbf{B}_0 \gg 3$ mT, which is fulfilled in a general NMR experiment.

¹⁴As the A-phase is not mentioned in this thesis before: The preferred direction in spin space $\hat{\mathbf{d}}$ and orbital space $\hat{\mathbf{l}}$ are macroscopically ordered independent from each other, this in contrast with the B-phase where the orientation is relative from each other. However, in the case of a pure A-phase (without surface effects and magnetic fields) the dipole energy is minimized if both vectors $\hat{\mathbf{d}}$ and $\hat{\mathbf{l}}$ are parallel.

¹⁵Technically this would be the A₂-Phase. Here $\Delta_+ > \Delta_-$, but the dipole energy is still minimized if $\hat{\mathbf{d}}$ is along the $\hat{\mathbf{l}}$ -vector.

$$\omega_{\parallel}^2 = 2\Omega_A^2. \quad (4.28)$$

Here the longitudinal frequency is expressed in the longitudinal frequency component of the A-phase.

In the case that $\hat{\mathbf{w}}$ and $\hat{\mathbf{d}}$ are perpendicular, there should be no longitudinal resonance. However, a transverse resonance frequency shift is expected, behaving as:

$$\omega_{\perp}^2 = \omega_L^2 + 2\Omega_A^2. \quad (4.29)$$

If one compares this with equation (4.25), a shift twice the shift in the bulk A-phase is expected. So, the longitudinal or transverse frequency components are determined by the relative orientation of $\hat{\mathbf{w}}$ and $\hat{\mathbf{d}}$, and in general one can say that the longitudinal and transverse resonance frequencies are given by:

$$\omega_{\parallel}^2 = 2\Omega_A^2 \cos^2 \gamma \quad (4.30)$$

$$\omega_{\perp}^2 = \omega_L^2 + 2\Omega_A^2 \sin^2 \gamma, \quad (4.31)$$

where γ is the angle between $\hat{\mathbf{w}}$ and $\hat{\mathbf{d}}$.

4.4.3 Axial state

If an A-phase-like-state (axial state) is realized in a confined geometry, one creates (as in the case of the B-phase) textures inside the container. In this case the boundary conditions require that the $\hat{\mathbf{l}}$ -vector is perpendicular to the surface [89]. If the radius R of the cylinder fulfills the condition: $\xi(T) \ll R \ll \xi_D$, $\hat{\mathbf{l}}$ and $\hat{\mathbf{d}}$ are uncoupled¹⁶. A magnetic field parallel to the cylinder's axis will orient $\hat{\mathbf{d}}$ into the plane perpendicular¹⁷. In this situation the most likely textures are the Mermin-Ho (MH), radial-, and circular disgyration, see figure 4.12. In static conditions, for radii $R/\xi(T) \geq 10$ the MH-texture is stable.

For narrow cylinders with $R/\xi(T) < 10$, the disgyration-type of textures become the stable ones. This condition can be reached as well, since the coherence length is tunable with temperature and pressure. In general one can say that close to the transition temperature T_c ¹⁸ the radial disgyration has the lowest energy of the three textures¹⁹.

As NMR potentially provides the best clarification which texture is present in the narrow channel, it is important to know how the frequency will shift. In the conditions of narrow cylinders, $\xi(T) \ll R \ll \xi_D$, then Takagi's prescription [122] yields for the longitudinal and transverse resonance frequencies:

$$\omega_{\parallel} = R_{\parallel} \Omega_A, \quad (4.32)$$

¹⁶If the dipole coherence length ξ_D is much longer than the radius R it can be considered as a dipole free situation, for which the vector $\hat{\mathbf{d}}$ can be considered uniform in the container.

¹⁷The reader is reminded that $\hat{\mathbf{d}}$ is perpendicular to the spin angular momentum of the cooper pairs \mathbf{S} ; $\hat{\mathbf{d}} \cdot \mathbf{S} = 0$.

¹⁸Here the coherence length is relatively long, since $\xi(T) = \xi_0(1 - T/T_c)^{-1/2}$.

¹⁹As calculated in the dipole free situation.

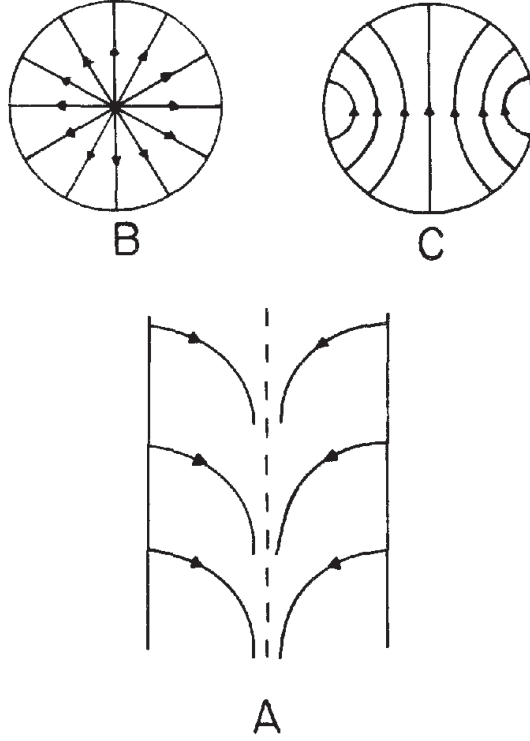


Figure 4.12: The three textures. The arrows indicate the $\hat{\mathbf{l}}$ -vector direction. (A) Side view of the MH-texture; (B,C) top views of the radial- and circular disgyration texture, respectively. Figure is taken from [121].

$$\omega_{\perp}^2 = \omega_0^2 + R_{\perp}^2 \Omega_A^2, \quad (4.33)$$

where R_{\parallel} and R_{\perp} are scaled frequency shifts for the longitudinal and transverse components, respectively. R_{\parallel} and R_{\perp} contain the (average) orientation of the $\hat{\mathbf{l}}$ components in the cylinder. In the local-oscillator model Bruinsma and Maki [121] calculated the frequency shifts of each texture for cylinders with a radius of $1 \mu\text{m}$, the results are put in table 4.4. As the $\hat{\mathbf{l}}$ has cylindrical symmetry (around the axis of the cylinder) for the MH- and radial disgyration textures, one does not expect a longitudinal resonance mode. The transverse resonance shift comes from the (average) difference between the $\hat{\mathbf{l}}$ components in the plane perpendicular to the axis of the cylinder, hence $R_{\perp} = \sqrt{\langle l_x^2 \rangle - \langle l_y^2 \rangle}$.

On the other hand, as for example is shown by [123], if we have a sufficiently small ratio of R/ξ_0 ²⁰, the radial disgyration texture is most favorable. Here the

²⁰In the calculation of Bruinsma and Maki the ratio was around $R/\xi_0 \approx 50$. In ref [123] the ratio

	Mermin-Ho texture	Radial disgyration	Circular disgyration
R_{\parallel}^2	0	0	0.70
R_{\perp}^2	0.20	0.50	0.85

Table 4.4: R_{\parallel}^2 and R_{\perp}^2 as calculated by Bruinsma and Maki [121] for cylinders with a radius of 1 μm .

angle between the $\hat{\mathbf{l}}$ - and $\hat{\mathbf{d}}$ -vectors²¹ rotates by 360 degrees when it goes around the center of the cylinder. In this configuration the regions $\hat{\mathbf{d}} \parallel \hat{\mathbf{l}}$ and $\hat{\mathbf{d}} \perp \hat{\mathbf{l}}$ are equal, see figure 4.12B. The region $\hat{\mathbf{d}} \parallel \hat{\mathbf{l}}$ will give a positive frequency shift $\omega_{\perp} = \sqrt{\omega_L^2 + \Omega^2}$ and the region $\hat{\mathbf{d}} \perp \hat{\mathbf{l}}$ will give a negative frequency shift $\omega_{\perp} = \sqrt{\omega_L^2 - \Omega^2}$. Here the two opposite shifts will cancel each other, which gives a net transverse resonance shift of zero. In other words, the scaled frequency shift R_{\perp} has no net value, hence $R_{\perp} = \sqrt{\langle l_x^2 \rangle - \langle l_y^2 \rangle} = 0$. Of course also no longitudinal mode is expected here, as the $\hat{\mathbf{l}}$ -vector has rotational symmetry around the axis of the cylinder.

One property of the axial state should be emphasized. This is an equal spin pairing state, for which the susceptibility should be constant (to first order) as function of temperature [12] [21] regardless of any frequency shift.

4.4.4 B-phase

As the coherence length decreases by lowering the temperature or increasing the pressure, see equations (1.33) and (1.34), the ratio between R/ξ increases. By enough reduction, meaning the ratio of R/ξ becomes significantly large (see figure 4.2), the container can be considered more like a bulk system. Concerning these narrow fibers, we do expect to see the (distorted) B-phase for low enough temperatures (or/and high enough pressure). Of course, as now $\xi_H \gg R$, the wall of the cylinder will play a dominating role in the distribution of the $\hat{\mathbf{n}}$ -texture over the sample, as explained in sections 3.3 and 3.4.

It is not completely clear how the $\hat{\mathbf{n}}$ -vector would behave in such small cylinders with $R \ll \xi_H$, but as shown in the case of diameters of 1 mm, see sections 3.8 and 3.9, it is most likely to act similarly to one of those textures. Meaning that, in the case the wall completely dominates the spatial distribution of the texture, the transverse NMR shift would behave as in equation (3.9) with $\beta = \cos^{-1}(1/\sqrt{5}) \approx 63.4^\circ$. In the alternative configuration, the $\hat{\mathbf{n}}$ -vector gradually changes from the boundary conditions at the wall to the boundary condition at the center of the cylinder, resulting

was considered to be $R/\xi_0 < 5$, which is energetically more favorable for the radial disgyration, and more applied to the conditions of our experiment, as our radius is around 270 nm and the coherence length ξ_0 around 50 nm.

²¹The $\hat{\mathbf{d}}$ -vector is assumed to rotate rigidly in the presence of an external radio frequency field \mathbf{B}_1 , and lies in the xy -plane.

in a broader NMR absorption line shape ²² (compared to the A- or normal phase), which coincides with $\beta(r)$ varying over the sample between zero and approximately 63.4°. In this case the NMR spectrum is given by equation (3.10).

In previous experiments the ratio between the amount of ³He atoms at the surface and in the liquid was so small, that any (few) layer(s) of ³He atoms adsorbed at the surface of the container's wall hardly had any influence on the obtained NMR signals. However, in this confined geometry the ratio between the atoms positioned at the surface/volume is around 1 ‰. Although the total number of adsorbed atoms may still be a small fraction of all the atoms in the channel, they do act as a solid layer, for which the Curie-Weiss susceptibility is considerable larger than that of the Fermi liquid, and cannot be ignored. The Curie-Weiss law is given by:

$$\chi = \frac{C}{T - \theta}, \quad (4.34)$$

where θ is the Curie-Weiss constant, which is around 0.5 mK for solid layers, see for example [124]. The constant C is referred to as the Curie constant and for spin $\frac{1}{2}$ systems is given by

$$C = \frac{\mu_0 N_A (\frac{1}{2} \gamma \hbar)^2}{k_B}, \quad (4.35)$$

where N_A is Avogadro's number.

It is known that there is a rapid exchange rate between the liquid ρ_1 and the solid ρ_2 , and if one use magnetic resonance frequencies small compared to this exchange frequency a single NMR line will be observed [125]. As described by the paper of Hook and Kaplinsky [126] about the B-phase, in the absence of driving forces and dissipation, the spin angular momentum densities \mathbf{S}_1 and \mathbf{S}_2 of respectively the liquid and solid atoms satisfy ²³

$$\ddot{\mathbf{S}}_1 = \dot{\mathbf{S}}_1 \times \omega_L - \Omega^2 \cdot \sigma_1 - \rho_1 \dot{\mathbf{S}}_1 + \rho_2 \dot{\mathbf{S}}_2. \quad (4.36)$$

From here the NMR frequencies can be deduced and are given by

$$\omega_0^2 = \frac{1}{2}(\omega_L^2 + \mu\Omega_B^2) + \sqrt{\frac{1}{4}(\omega_L^2 + \mu\Omega_B^2)^2 - \omega_L^2 \mu\Omega_B^2 \cos^2 \beta}, \quad (4.37)$$

this differs only from the bulk result by the substitution of $\mu\Omega_B^2$ for Ω_B^2 in equation (3.9). In the limit of $\mu\Omega_B^2 \ll \omega_L^2$ ²⁴ equation (4.37) can be rewritten as

$$\omega_0 \approx \omega_L + \frac{\mu\Omega_B^2}{2\omega_L} \sin^2 \beta, \quad (4.38)$$

²²In this configuration we do not expect to see any spin waves. The radius of the cylinder is considerable smaller than in case of section 3.8, consequently the characteristic length L_1 of equation (3.32) is so small that the energy levels between of the spin wave modes will be so large that even the lowest spin wave mode cannot exist in such a confined geometry.

²³Here the isotropic susceptibility of the B-phase is already taken into account. For derivation of the A-phase one should start from the more general expressions.

²⁴As is the case in our experiments.

where $\mu = M_{liq}/(M_{liq} + M_{sol})$. M_{liq} and M_{sol} are the total magnetization of the liquid and solid, respectively (see also [127]).

Another important feature of the B-phase is that its susceptibility should decrease as is explained in section A.3.

4.5 NMR results of the channels

4.5.1 Normal state

The channels, to perform NMR on it, were installed at the position as is illustrated in the red part of figure 2.1. The ratio of the signal from the coil around the channels compared to the signal from the coil around the 1 mm cylinder (blue part of figure 2.1), of course in the same conditions (pressure and temperature) and in the normal state, was close to 0.01. This would indicate that the total cross sectional area of the ^3He in the fibers is 1 % of that in the cylinder, which is reasonably close to the estimated ²⁵ 1.5 %. Upon cooling the observed susceptibility seems to saturate at 50 mK, as is expected in the Fermi liquid theory (FLT) (see section 1.1). Thus we confirmed that there is ^3He liquid ²⁶ in the channels. Another indication is that the NMR signals ²⁷ increased as function of pressure as expected in the FLT (densities get higher and more quasi-particles can be 'seen' in the same volume); the susceptibility should change as described by equations (1.5) and (1.6), which was in good agreement with the measurements.

Only a few measurements are performed on the ^3He in the fibers in the normal state, mainly in preparation for cooling to the lowest temperatures, nevertheless they did confirm that the channels were filled with liquid helium. This result by itself is already an achievement, and proved that our weakly coupled transformer technique is able to detect one μmole ^3He in low magnetic field (15 mT) with a bandwidth of 2.6 Hz.

4.5.2 Channels cooled down to the lowest temperatures

Initially the channels were filled with liquid ^3He near zero pressure, for which the coherence length is the longest (see table 4.1) and non-bulk superfluid properties would be more significant. However, even by cooling to the lowest available temperature (down to 100 μK) no transverse NMR shifts ²⁸ were observed. Although it is possible

²⁵In our estimation we assumed that average diameters of the channels were 540 nm, which is clearly not true as we can see from figure 4.6. However, as we are not sure that all used fibers have the same distribution in diameter, we used this average number. Surely, it would give an additional error, but as it is only to compare the order of magnitude, it should not be a problem.

²⁶As for example the helium would have been solidified, we should have seen the Curie-Weiss behavior.

²⁷If for some reason we mainly observed solid ^3He , we would hardly see any pressure dependency.

²⁸The raw data did show a small shift. The reason is that still some stray field of the demagnetization magnetic is observed at the experimental setup and that the magnetization of the solid (adsorbed ^3He at the walls) is visible in these small channels. Both effects are noticeable far for any

that a phase transition to the axial and/or polar phase has occurred, as explained in section 4.4.2 and 4.4.3, since it is possible that these phases have no transverse resonance frequency shift, it is still remarkable that no (distorted) B-phase properties were visible at the lowest temperatures. It could be that the coherence length of the Cooper pairs is still too large compared to the diameter of the narrow channels (or too much diffuse scattering) to form a superfluid (at any temperature). For this reason we increased the coherence length (by increasing the pressure), but never a transverse resonance frequency shift was observed. Eventually the pressure was increased ²⁹ to 10 bar, which reduced the coherence length more than twice, see table 4.1. Nevertheless, we did not observe any shifts, not to mention any observation of a transition to the B-phase.

The observed signals were obtained at the original position of the rf-coil in figure 2.1, or as pointed out in detail in figure 4.14(a). An example of the absorption signal is plotted in 4.13(a), which is an average of 238 measurements at 10 bar near 500 μK .

T_c (Bulk), and after subtraction of both effects no net shift was observed.

²⁹We did not dare to go higher in pressure, as we were afraid that the glued parts will not hold it, and eventually would explode our cell.

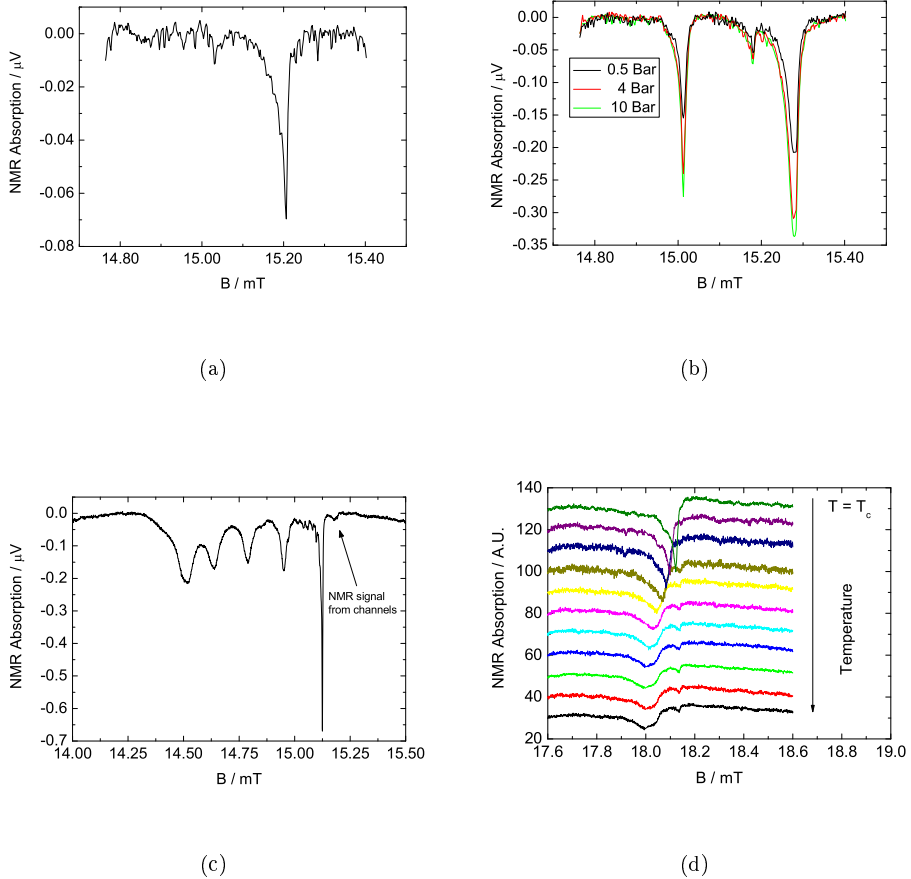


Figure 4.13: (a) NMR signal of the ^3He in the channels, with the tank coil positioned as illustrated in figure 4.14(a). Here the ^3He is at 10 bar and 500 μK and the signal is averaged over 238 sweeps. This signal consists of a single absorption line which does not show any transverse resonance frequency shift at any temperature. (b) NMR signal of the ^3He in the channels, with the tank coil positioned as illustrated in figure 4.14(b). Here the data is plotted for 0.5, 4 and 10 bar, where the temperature is just above the bulk T_c corresponding to that pressure. The small middle peak corresponds to the ^3He inside the channels, the two side peaks most likely originate from the ^3He in the open spaces between the fibers. We treat this in detail in section 4.5.4. (c) NMR signal of the ^3He in the channels and in the 1 mm cylinder, with the tank coil positioned as is illustrated in figure 4.14(c). The temperature is around 300 μK and the pressure is 6 bar, while the signal is averaged 52 times. In the total line shape we see the existence of spin waves in the cylinder part, and the remaining part (at the Larmor frequency) is believed to be the signal from the channels. (d) NMR signal of ^3He in the channels immersed in 'bulk' ^3He as illustrated in figure 4.14(d). The 'bulk' part undergoes a phase transition into the B-phase (at the expected T_c). The part of the line shape from the ^3He in the channels stayed in resonance at the Larmor frequency, for the whole temperature range. Here data is shown for 2.1 bar (typically averaged for 80 times) at temperatures between $0.4T_c$ and T_c . Resonances are here at higher magnetic fields (Larmor frequency coincides with 18.12 mT) as the used tank circuit had a resonance frequency of 588 kHz.

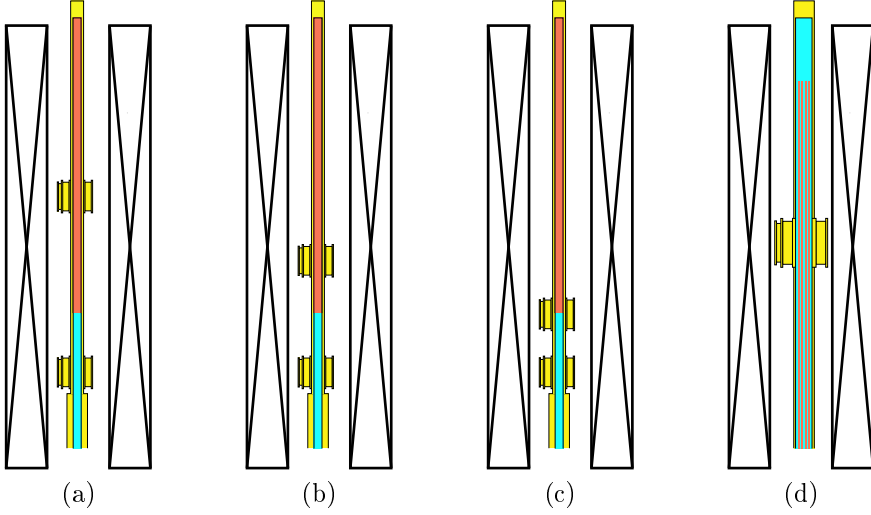


Figure 4.14: The various configurations of the experimental setup, showing the different positions of the tank coil around the channels relative to the interface of the bulk liquid in the 1 mm cylinder.

Since the behavior of the observed signals in the channels in configuration 4.14(a) contradicted our expectation and the physical intuition, we considered the possibility that spurious heat released from the quartz glass and the stycast 1260 (still stored and/or created due to NMR) was sufficient to prevent the liquid in the channels to cool below the critical temperature. While this was estimated³⁰ to be not the case, we wanted to corroborate this by reducing half the distance between the coil position and the interface between channels and the 1 mm cylinder, as illustrated in figure 4.14(b). The NMR result of this configuration is plotted in figure 4.13(b).

³⁰All heat created/stored in quartz/PEI (This will be discussed in more detail in the following paragraphs of this section), which wants to be released in the ^3He of the channel should overcome the Kapitza resistance between the liquid helium and the SiO_2 . This Kapitza resistance is determined by the acoustic mismatch theory, which describes the boundary resistance as: $R_K = \Delta T / \dot{Q} = 15\hbar^3 \rho_s v_s^3 / (2\pi^2 k_B^4 T^3 A \rho_h v_h)$. The resistance was calculated for 1 mK, for which the density of ^3He $\rho_h = 0.082 \text{ g cm}^{-3}$ and the sound velocity is 194 m s^{-1} [128]. The total estimated surface area of all the channels was 40 cm^2 . The quartz has a density of $\rho_s = 2.66 \text{ g cm}^{-3}$ and a sound speed of $v_s = 5570 \text{ m s}^{-1}$. This will give a 'Kapitza conductance' of $\dot{Q} / \Delta T \approx 8.3 \cdot 10^{-11} \text{ W K}^{-1}$. This should be compared to the thermal conductance through the ^3He in the channels, using the thermal conductivity κ of ^3He at 1 mK, $\kappa \approx 2 \text{ mW cm}^{-1} \text{ K}^{-1}$ [31]; and as the fibers are roughly 6.5 cm long, the thermal conductance through the channels filled with helium could be calculated to be $\dot{Q} / \Delta T = -\kappa A / \Delta x \approx 2.5 \cdot 10^{-8} \text{ W K}^{-1}$. If the heat transferred over the Kapitza resistance has any significant influence on temperature of ^3He inside the channels, then the conductances should have the same order of magnitude, meaning that the temperature gradient over the Kapitza resistance should be 3 orders of magnitude higher than over the ends of the channels. It is not likely that such a high temperature is build up in the cylinder, as the thermal radiation would not allow such high temperatures on the outside of the cell and for such high gradients the thermal conductivity (κ of quartz is $1 \cdot 10^{-5} \text{ W cm}^{-1} \text{ K}^{-1}$ at 50 mK) through the glass/PEI down to the experimental space is better than over the Kapitza resistance.

(still in the normal state), which has the most remarkable feature that we observe 3 absorption lines instead of one. We believe that the two peaks away from the Larmor frequency originate from unclosed spaces between the fibers (somehow the stycast was not able to fill all the spaces there), the middle peak fits the right frequency/field and amplitude to correspond to the ^3He in the channels. When the liquid is cooled below T_c the two side peaks seems to undergo a phase transition, which we will describe in detail in section 4.5.4. In the remaining part of this section we will focus ourselves on the signal coming from the channels only.

As the ^3He in the channels are positioned closer to the interface between fibers and cylinder, and one consider the heat release from the quartz to liquid helium a problem, then the temperature gradient (from interface to position of tank coil) should definitely be smaller compared to the initial situation. However, when we repeated the measurement ³¹, as in the case of the initial measurements, no transverse resonance frequency shifts were observed (or change in the susceptibility).

As these results correspond to the previous measurements, we were willing to put the tank coil even closer to the interface. As a matter of fact we put the tank coil at the position ³² of the interface, which is illustrated in figure 4.14(c). In this position the signal is observed from both the channels and the cylinder, and in the normal state no difference between the signals can be made as they both overlap at the Larmor frequency ³³. As we cool down from this position, the spin waves in the cylinder are created as explained in chapter 3, and as all modes of this spin waves shift away from the Larmor frequency, it is possible to separate the two signals. In figure 4.13(c) the NMR results at the interface are shown at a temperature of approximately 300 μK and 6 bar; the results are averaged 52 times. Here it is believed that the remaining absorption line at the Larmor frequency is the signal from the channels. This believe becomes stronger as the total ratio between the absorption signals is (approximately) proportional to the volumes and taking into account that the susceptibility of the ^3He inside the cylinder is reduced by a factor $\frac{1}{3}$. As the temperature gradient between the inside of the channels and the interface should now be rather small, it is curious that even in this conditions (300 μK and 6 bar) no transverse resonance frequency is observed, and hard to believe that the temperature (inside the channels) is too high to form the B-phase.

³¹Again from zero to 10 bar.

³²Actually only 1.5 mm of the tank coil was put over the channels and the rest over the cylinder.

³³The side peaks as observed in figure 4.13(b) can be observed as they are far enough from the Larmor frequency, and their amplitude is roughly a factor two smaller compared to the previous position.

If sufficient heat was generated in the quartz or the stycast due to the rf-field (which is unlikely ³⁴) or stored heat was released over time ³⁵, one can imagine that it will influence the thermal equilibrium too much. However, these heat sources were considered to be too small to be harmful. Nevertheless, it was decided (by the lack of any evidence of a B-phase transition) to analyze NMR results of unglued fibers. Meaning that we have still a PEI cylinder full of these fibers, but without any stycast (enormous reduction of hydrogen in the system, plus no direct contact between fibers and PEI). This PEI cylinder had a 2 mm inside diameter, in which the fibers are 'freely' spaced. The total volume of channels compared to the volumes between the fibers was estimated to be 15 %. As the spaces between the fibers are relatively large, the ³He should behave nearly as in bulk, meaning that it will undergo the normal \rightarrow B-phase transition. An overview of this configuration can be seen in figure 4.14(d). Results of the measurements on this cell are plotted in figure 4.13(d). Here the pressure was 2.1 bar, and the was cooled below $0.4 T_c$. Below T_c we see that the 'bulk' liquid undergoes the phase transition to the B-phase, the susceptibility reduces an \hat{n} -texture is formed. Consequently, the resonance frequency shifts ³⁶ away from the Larmor frequency. For low enough temperatures we can distinguish the remaining absorption peak at the Larmor frequency. This signal correspond to the 15 % (volume ratio) compared to the bulk signal in the normal phase. We are convinced ³⁷ that the signal is from the liquid in the channels. Again we observe the familiar result that the signal in the channel seems to be unchanged as function of temperature (or pressure). Here a significant part of the hydrogen atoms are removed and is surrounded by liquid ³He, for which the heat can be drained off much better. Again

³⁴Heat is of course generated (other sources than in the ³He) due to NMR measurements in the stycast/PEI, mostly because of the hydrogen in the polymer. However, the experimental sweeping scans are around the magnetic fields corresponding to the resonance frequencies of ³He, for which the hydrogen tail is far away (see for example figure 2.18). Technically oxygen and silicon (from the quartz glass) do have isotopes with a net nuclear spin, however their natural abundance is small 0.038 % and 4.6832 %, respectively. Besides, their tails (as they are further away) are even smaller, for which the total heat generated by those spin is considerable smaller. The heat generated in the hydrogen (around the channels and for used sweeps values) was estimated 3 times more than in the ³He inside the channels, where the total generated power was calculated to be $1 \cdot 10^{-16}$ W. To estimate the upper limit of a temperature gradient created in these channels, we assumed that all heat was released into the top of the channels. The thermal conductivity κ in ³He at 1 mK is about $2 \text{ mW cm}^{-1} \text{ K}^{-1}$ [31], and as the fibers were roughly 6.5 cm long, the thermal heat transported through the channels filled with helium could be calculated by $\dot{Q} = -\kappa A \Delta T / \Delta x$. The estimation showed that an incredibly small gradient ΔT of 4 nK is needed to conduct all this heat, which seems to be practically unharful for the experiment.

³⁵These problems are known as for example is notified by Pobell [31]. However, the heat releases are small and are approximately 0.1 nW g^{-1} at 1 K, and decrease exponentially over time. This half life time may be around a day, which is relatively short compared to the total time the dilution fridge was performing at the lowest temperatures (weeks, sometimes months). Hence these heat releases should be negligible overtime, if not already from the start. Also no differences over time are seen.

³⁶As the geometry of this cell, cylinder filled with 'free' fibers, is rather complicated, we did not put much effort to understand what kind of textures will be formed, or how that will shift the NMR frequency. Of course it is intuitively understandable that the \hat{n} -vector will bend over the sample, which will coincide with a shift in the transverse resonance frequency (see equation (3.9)).

³⁷An other candidate will be adsorbed/solid ³He, however the signal is considered to be too large, and one should expect to see an increase of the susceptibility, as it has an Curie-Weiss behavior.

it seems that the heating concerning the hydrogen atoms is of no influence on the effects we observe. The only heating source, which cannot be eliminated, is the quartz glass itself. However, as all heat, created or released, due to the SiO_2 in the quartz glass was estimated much smaller than in the case of the hydrogen atoms, we considered it to be unlikely to warm up the liquid to a significant level.

4.5.3 Discussion

As is reported in the previous section, no NMR shifts are observed of the ^3He inside the channels. One may think that it is reasonable to assume that the liquid is still in the normal state and no phase transition has occurred at all. If the liquid is still in the normal state, it can be of two reasons.

- The suppression of the superfluid transition in these geometries is much stronger than theoretically is calculated. The phase diagrams as calculated by Li and Ho, see figures 4.4(a) and 4.4(b), are for cylinders with a radius ³⁸ of 300 nm. Additional suppression should than be more than a *millikelvin*, a scenario which seems to be unlikely.
- Another scenario can be that the liquid inside the channels is not cooled into the submillikelvin regime. The test of several different configurations, to reduce temperature gradients and heat sources, did not show any changes in the NMR results. This is unexpected as the temperature gradient of some configuration (especially at the interface) should be nil. Also heat transport calculations showed that the liquid inside the channels should have been cooled into the submillikelvin regime, overall an unlikely scenario as well.

At this point it should be emphasized that we have never observed a transition into the B-phase. However, we cannot exclude that a phase transition has happened. The B-phase should have been the easiest to detect, even without any shift in the resonance frequency, because the susceptibility should decrease. One important remark should be made about earlier measurements in slab geometries. Freeman and Richardson [129] also never observed the A-B phase boundary in their 300 nm slab geometry, which is also in contrast with theoretical calculations, see for example [130, 86]. It may be that the absence of the B-phase has the same basis for both geometries, and that for unknown reasons the theoretical calculations are too optimistic. Only when slab geometries become bigger, for example by Bennett *et al.* [91], the A-B phase boundary is observed. In this particular case the slab geometry is around 600 nm.

For the polar or any axial states, which are equal spin pairing states, we do not expect (at least till second order) changes in the susceptibility. We will now discuss their expected resonance frequency shifts for our geometry.

Axial states If any axial state would have been formed then, as explained in section 4.4.3, calculations showed that no net resonance frequency shift for small cylinders

³⁸Our average radius is around 270 nm, which is close enough to expect similar phase diagrams.

should occur. Small is here considered when $R/\xi_0 < 5$ ³⁹, which is definitely the case in most conditions of our experiments. Only for the highest pressures we do not fulfill this criteria, maximally the ratio was $R/\xi_0 \approx 10$, however even for these ratio's the most likely texture must be the radial digyration⁴⁰ for which the net transverse resonance frequency shifts will be zero. So, if we would have had an axial state in our channels it would have been unnoticed by our transverse NMR experiment. Longitudinal experiments are also not suitable for clarification of this state, as the symmetrical symmetry of the $\hat{\mathbf{l}}$ -vector in the radial digyration texture will not have any net components for longitudinal NMR shifts either.

Polar states The NMR shifts of the polar state are determined by the angle γ between the vectors $\hat{\mathbf{w}}$ and $\hat{\mathbf{d}}$, as described in section 4.4.2. Concerning our geometry, we would expected that the $\hat{\mathbf{d}}$ -vector is perpendicular to the axis of the cylinder (magnetic field is parallel to the axis of the cylinder), and that $\hat{\mathbf{w}}$ is perpendicular to the wall⁴¹ of the cylinder. In this case we would only have a longitudinal frequency shift. It should be mentioned that Takagi said [123], concerning the B-phase in confined pore geometry, the symmetry axis of the orbital components is parallel to the magnetic field, which is a consequence that some components of the order parameter are suppressed at the wall of the B-phase (leaving the Polar phase). It is this possibility we had taken into consideration. If this configuration would be realized, then it is not the longitudinal component which will be measured, but the transverse resonance frequency shift.

Reasons to perform transverse NMR experiments around the channels were to unravel how the relative orientation of the $\hat{\mathbf{w}}$ and $\hat{\mathbf{l}}$ -vector was configured in such a small cylinder. It would also be a good method to observe if any characteristic time scale (T_1 or T_2) would change in this superfluid. Also, as is pointed out by Barton and Moore, the phase transitions could be 1st and 2nd order, which could be clarified by hysteresis experiments.

However, the observation of the B-phase failed to occur, and by the lack of this orientation point made the performing of the above ideas hard. The problem now is that the existent of the two others states can not be excluded/included by our performed experiments. It means that our cell configuration should have serious modifications to prove if any of these states exist inside the channels. The following points should definitely be considered:

- Experiments at higher pressures: The cell should be strengthened so that experiments at higher pressures can be performed. Initially the use of low pressures was desirable, as here the coherence length ξ_0 is the largest and non-bulk properties would have been expected for these conditions. However, the lack of

³⁹The calculations of Takagi [123] were done in this regime.

⁴⁰Energy calculations excluding superfluid mass and spin currents showed that the radial digyration texture should be the most stable one if $R \leq 10/\xi(T)$.

⁴¹As in the case of the $\hat{\mathbf{l}}$ -vector in the axial state.

observing any B-phase transition makes it desirable to even decrease the coherence length more. As this coincided with increasing pressure, one should be sure that the cell should be able to withstand it.

- The possibility to perform longitudinal NMR: This can be accomplished when an oscillating field is applied along the external magnetic field. In this configuration the $\hat{\mathbf{d}}$ -vector tends to rotate (at resonance) in the plane normal to the magnetic field, which will be observed by the probe. However, this experiment is far from trivial ⁴², and is definitely not easy as the expectation of the polar state only exist in a small fraction of the phase diagram, see figures 4.2, 4.4(a) and 4.4(b).
- Perform an experiment with an angle γ between the cylinder axis and the externally applied magnetic field. This is presumably a better alternative than the longitudinal experiment. If we have an angle γ (say 45°), we will create both a finite transverse and longitudinal component, in case we deal with the polar phase. Here the transverse component is easier to detect than the longitudinal component. The axial state will probably be a bit harder to interpret in this condition, and it should be re-estimated/recalculated which shifts can be expected. Also the bore of the magnet should be increased, to be able to make a configuration with large enough angle between the magnetic field and the cylinders axis.
- Heat transport measurement through the channels: This method should help to probe the gap structure of the superfluid, possible allowing to reconstruct the phase. However, this method cannot determine the symmetry of the order parameter.
- Torsional oscillator: Alternative method to determine if any mass decouples from the system, a method to indicate if any superfluid is formed in the channels.

At least in this stage it cannot be said with any certainty if a superfluid or not is formed inside the channels. It should be emphasized that experiments in real long cylinders with diameters of a few times the coherence length were never performed before. There is still the possibility that a deeper physical cause excludes a (quasi) one-dimensional superfluid ⁴³. However, there are some cautious and reserve claims that the polar phase has (indirectly) been seen in small pores and aerogel, see for instance [131] and [96]. Even if the polar phase really existed in these confined geometries it is not with the same boundary conditions. The (average) radial direction may be of

⁴²To quote D.D. Osheroff about his longitudinal experiments in the A-phase [10]: *"I searched hard and long for such a mode, but found nothing. In the end, I gave up the idea that the mode would be sharp, and assumed instead that it would be very broad. In this case, one could not detect it by sweeping the NMR frequency, since one would then sweep over the broad Q of the NMR tank circuit. I decided to hold the frequency fixed and sweep the temperature, thereby sweeping the longitudinal resonance through my probe frequency. This strategy worked quite well, and the resonance was very broad."*

⁴³Compare one dimensional crystals, where (quantum) fluctuations are not damped by the lack of long range order and make these crystals unstable.

the same order, but the axial direction is small. As these geometries are surrounded by bulk liquid, it may be that the superfluid state inside such a pore is influenced by the bulk superfluid B-phase (proximity effect).

4.5.4 NMR shifts influenced by the adsorbed helium-3 at the wall

As already mentioned in section 4.5.2, the NMR signals, as we position the tank coil closer to the interface, reveal two additional absorption lines, see figure 4.13(b). It is clear that the signal cannot originate from the ^3He inside the channels, as their amplitude is too large and these absorption peaks are not observed for distances far enough from the interface⁴⁴. However, we definitely observe two additional peaks, of which the resonance frequencies do not overlap with the ^3He inside the channels or themselves. One can imagine that some spaces between the fibers or between the fibers and the PEI wall are not totally filled with stycast, which would leave some open spaces that will be filled with liquid ^3He .

As it is believed that the additional signals (absorption lines) are coming from open spaces between the fibers and/or fibers and the PEI wall, it is strange that all those signals do not overlap, as the gyromagnetic ratio for all ^3He atoms is the same. Differences in magnetic fields of the order of the inhomogeneity ($\Delta H(\mathbf{r})/H = 5.4 \cdot 10^{-4}$) would somehow be helpful to explain this phenomenon. However, even then the signal should be a broad absorption line and not concentrated around three different resonance frequencies. In addition the difference between the two outer peaks is around 0.27 mT⁴⁵, which is over an order of magnitude more than the inhomogeneity of the magnet. Another interpretation could be that locally the solid (adsorbed helium at the walls) gives, due to its magnetization, a slightly different field. However, as the magnetization is approximately proportional to $1/T$, see equation (4.34), the absolute distance between the absorption lines should change as the temperatures is swept. If we compare our NMR signals from 100 mK to T_c (~ 1 mK), we do not see any change in the (magnetic) separation of the peaks, from which we exclude any solid to be the source of the magnetization. The only differences in separation we have observed were when we compared the data of different runs⁴⁶. The differences were always small, but maximally an additional separation of 0.026 mT was observed between the furthest peaks. It is clear that the ^3He atoms, corresponding to each peak, must locally experience a different magnetic field (as function of \mathbf{B}_0), and as any additional magnetization/magnetic field or inhomogeneity of the magnet failed to explain it, we wondered if the magnetic field lines are homogeneously distributed in the cell. If for any reason the magnetic field lines are not completely homogeneously distributed,

⁴⁴If ^3He enters the channels, they should fill the whole length of the channels.

⁴⁵If one compares this with the chemical - or Knight shift, caused by the electrons that locally deform the magnetic field, is typically 1 ppm compared to the Larmor frequency. In our case the shift is $1 \cdot 10^{-2}$, which is (relatively) huge.

⁴⁶In the same run, which means the period the cryostat was cooled (below 4 K) till it was warmed up, no changes in separations were observed even not if the cell was pressurized to different pressures.

but may have preferences for spaces with certain solid/liquid ⁴⁷ ratios, then it would explain why certain volumes 'see' slightly different fields. Nevertheless, it cannot be said that this feature is understood at all, especially because of the largeness of the separation between the absorption lines.

While the phenomenon of having three separated peaks for the ³He atoms is unexplained, it is very convenient since their isolation allows a careful study of each of them. The absorption spectrum above T_c is illustrated in figure 4.13(b). We know, as explained in section 4.5.2, that the middle peak is from the atoms in the channels. The two outer absorption lines, which we will call from now on the left and right peak (corresponding with the lowest and the highest current in figure 4.13(b), respectively), are suggested to correspond with ³He in the open spaces between the fibers and fibers/PEI. The most important difference between these open spaces is the liquid to solid (adsorbed of ³He at the wall) ratio. Taken into account how the fibers are bundled, we know that possible open spaces will have a kind of axial symmetry for which the radial direction can have a width (if completely open) of a few micrometers. These open spaces are perfect to study ⁴⁸ the behavior of the B-phase for these dimensions. It is a bit surprising for the author, that not much data is published for cylindrical structures corresponding with these sizes *at low pressures*.

An example of what is observed in our NMR spectrum when we cooled the liquid below T_c , is plotted in figure 4.15. Here the pressure was 4 bar and the results are presented as if the liquid is cooling ⁴⁹ from 1.39 mK (is T_c) to 0.64 mK. Once more it is illustrated that the middle peak (signal in channels) does not show any shift or reduction in the amplitude (susceptibility). The other two peaks undergo a phase transition ⁵⁰ from the normal to the B-phase, both at the same temperature and at the bulk T_c (it must be said that any small suppression would not be detected as the temperature sweep rate (0.31 mK h⁻¹) was too fast for it). For both absorption signals, a reduction of the susceptibility is measured, characteristic for the B-phase. Also the absorption peaks get wider, as the \hat{n} -vector bends over the sample. It results in an (average) frequency shift to the left, as is explained in chapter 3 and section 4.4.4. The right peak seems to move roughly 1.5 times faster than the left peak, and for low enough temperatures it even shifts through the Larmor line of the ³He inside the channels. Eventually the absorption lines get very broad, which makes the SNR very small, and practically (with our used bandwidth) unable to follow anymore.

If one analyze the frequency shift, it is noticed that the shift is less than indicated by equation (3.9), because in this configuration the rapid exchange between the solid and liquid atoms cannot be neglected. As we wanted to determine the ratio between solid/liquid we should know the value of the μ parameter in equation (4.38), and

⁴⁷The adsorbed ³He atoms at the wall are 1 or 2 atomic layers thick, which can be (in average) slightly different in every run, and would be a possible explanation for different separations for certain runs.

⁴⁸At least in our configuration where the absorption lines are clearly distinguishable. Would they have overlapped, it would become very unclear.

⁴⁹Actually, for better thermal equilibrium, the data is obtained by heating the liquid.

⁵⁰Well there was never really doubt about it, but this phase transition ones more proves that the absorption signals were also coming from ³He atoms.

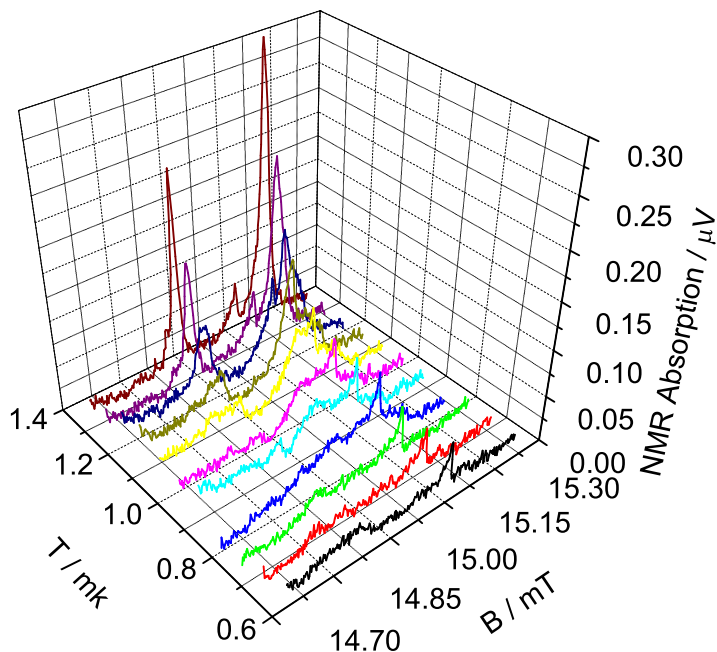


Figure 4.15: NMR absorption scans of ^3He as observed in the configuration of figure 4.14(b) at 4 bar, for various temperatures. The absorption is expressed in μV , which is the signal measured with the pick-up coil. The temperature range is between 0.64 mK and T_c (1.39 mK). At the transition temperature the 3 absorption peaks are in resonance at the Larmor frequency. The left and right absorption peaks come from the helium atoms in open spaces/pores between the fibers, the middle peak is the signal obtained from the atoms inside the channels. Lower temperatures show that the left and right peaks undergo a transition from the normal to the B-phase. The liquid inside the channels does not show any frequency shift or reduction of the susceptibility.

as the magnetization is proportional to susceptibility and field ($M = \chi H$), we can express μ in terms of susceptibilities, see equations (1.5), (1.6)⁵¹, (4.34) and (4.35), where we should also take into account that the susceptibility of the B-phase χ_B is temperature dependent, as is described in appendix A.3.

⁵¹This equation is expressed in CGS units, and should be converted to SI units by multiplying with the permeability μ_0 . Not to be confused with the magnetic moment.

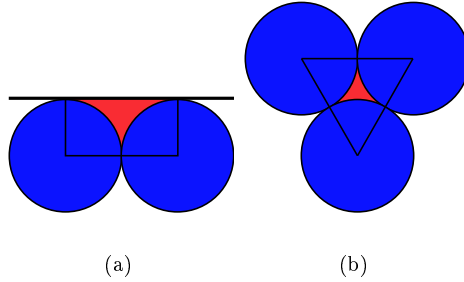


Figure 4.16: An ideal cross section of the possible open space between our fibers. In both pictures the blue circles are the cross section of the fibers (the channels inside the fibers are not illustrated), which have approximately a diameter of $30 \mu\text{m}$. The red area indicates the possible open space, due to the packing of the fibers. (a) The fibers against the (PEI) wall. Here the curvature of the wall is neglected as the diameter of the fibers is much smaller than the circumference of the PEI cylinder. The open spaces are in this configuration formed between the wall and the fibers. (b) Here the fibers are packed in a honeycomb structure, which leaves room for possible open spaces.

$$\mu = \left(1 + \frac{n_{sol}}{V_{liq}} \frac{N_A}{N_F} \frac{(1 + F_0^a)}{k_B(T - \theta)} \left(\frac{\chi_B(T)}{\chi_N} \right)^{-1} \right)^{-1}, \quad (4.39)$$

Here n_{sol} is the amount (in mole) of atoms adsorbed to the wall, and V_{liq} the volume of the liquid. This formula has only two fit parameters, namely the ratio n_{sol}/V_{liq} and θ . The other parameters are constants, pressure or temperature dependent, but all theoretically known (see appendices). The parameter θ is known to be close to 0.5 mK, but if necessary the exact value can be obtained by fitting the data. We like to start by estimating the fit parameter n_{sol}/V_{liq} . The possible open spaces in our cell are considered to be between the honeycomb spaced fibers, and between the fibers and the wall (PEI), for which a sketch is illustrated in figure 4.16.

Given these ideal geometries, the open space (area) can be calculated. The amount of adsorbed ^3He atoms at the wall (the solid) must be estimated. We do know that only the first two layers will be immobile⁵² and will be considered to form a triangular lattice⁵³ with an atom to atom distance of approximately 3 ångström.

⁵²Only the first two layers experience an effective pressure (potential) higher than at melting curve.

⁵³This is an assumption and mostly determined by the surface structure. Good atomically flat substrates have shown a hexagonal lattice for the solid layer. This is in our situation clearly not the case as the fibers are etched, but effectively we will assume a close packed hexagonal structure.

Open space between fibers and wall. The area is equal to the rectangle, as illustrated in 4.16(a), subtracted by two times a quarter of a circle.

$$A_{liq} = (A_{\square} - 2 \cdot 1/4 \cdot A_{\circ}) = (2r \cdot r - 2 \cdot 1/4 \cdot \pi r^2) \approx 96.57 \cdot 10^{-12} \text{ m}^2.$$

V_{liq} is the area times the length, hence $V_{liq} = A_{liq} \cdot l$.

The amount of atoms N at the surface of this open space, where we assumed that the atoms per layer form a regular arrangement with the highest packing coefficient⁵⁴ (hexagonal packing), is given by:

$$\begin{aligned} N &= A_{wall} \cdot (\text{highest packing coefficient}) / (\text{cross section one atom}) \cdot (\text{layers}) \\ &= (2 \cdot 1/4 \cdot 2\pi r + 2r) \cdot l \cdot \frac{\pi}{2\sqrt{3}} / (\pi \cdot (1.5 \cdot 10^{-10})^2) \cdot 2 \approx 1.98 \cdot 10^{15} \text{ l}. \end{aligned}$$

The ratio of n_{sol}/V_{liq} is now given by:

$$\frac{n_{sol}}{V_{liq}} = \frac{N/N_A}{V_{liq}} = \frac{1.98 \cdot 10^{15} \text{ l} / (6.022 \cdot 10^{23})}{96.57 \cdot 10^{-12} \text{ l}} \approx 34.03 \text{ mole m}^{-3}$$

Open space between fibers. The area is equal to the equilateral triangle, as illustrated in 4.16(b), subtracted by three times a sixth of a circle.

$$A_{liq} = (A_{\Delta} - 3 \cdot 1/6 \cdot A_{\circ}) = 1/2 \cdot 2 \cdot \sqrt{3} \cdot r^2 - 3 \cdot 1/6 \cdot \pi r^2 \approx 36.46 \cdot 10^{-12} \text{ m}^2.$$

Again the volume V_{liq} is the area times the length, hence $V_{liq} = A_{liq} \cdot l$.

The amount of atoms N at the surface of this open space is

$$\begin{aligned} N &= A_{wall} \cdot (\text{highest packing coefficient}) / (\text{cross section one atom}) \cdot (\text{layers}) \\ &= (3 \cdot 1/6 \cdot 2\pi r) \cdot l \cdot \frac{\pi}{2\sqrt{3}} / (\pi \cdot (1.5 \cdot 10^{-10})^2) \cdot 2 \approx 1.21 \cdot 10^{15} \text{ l}. \end{aligned}$$

The ratio of n_{sol}/V_{liq} is now given by:

$$\frac{n_{sol}}{V_{liq}} = \frac{N/N_A}{V_{liq}} = \frac{1.21 \cdot 10^{15} \text{ l} / (6.022 \cdot 10^{23})}{36.46 \cdot 10^{-12} \text{ l}} \approx 55.07 \text{ mole m}^{-3}$$

From this calculation it is clear that the ratio n_{sol}/V_{liq} is different for the two types of open spaces, and smallest for the open spaces between the fibers and the wall. The solid magnetization has than less effect on the NMR shift of the B-phase, and as the shift of the right peak of figure 4.15 is less restrained than the left peak, it is reasonable to accept that the right peak corresponds to the open spaces between fibers and wall, and the left peak to the open spaces between the fibers.

⁵⁴C.F Gauss proved that this packing coefficient for (2 dimensional) arrangement of circles is $\frac{\pi}{2\sqrt{3}}$.

If we want to fit the data with equation (4.38), it is convenient to know which line segment correspond to which β . As described in chapter 3 the $\hat{\mathbf{n}}$ -vector will bend over the whole sample, for which we showed detailed calculations of the bending of the $\hat{\mathbf{n}}$ -vector in a cylindrical geometry. In our open spaces the bending of the $\hat{\mathbf{n}}$ -vector is clearly observed as well, as the width of the left and the right peak of figure 4.15 get broader for lower temperatures. Calculations of the bending of the vector considering these geometries are far from trivial, and are for this reason omitted. However, the sizes of the open spaces are relatively small compared to the magnetic healing length ξ_H , for which we (as again explained in section 3.3) expected that the $\hat{\mathbf{n}}$ -vector will not be completely bent between the two boundary conditions ($\beta(0) = 0$; $\beta(R) = 63.4^\circ$), but mostly determined by the boundary conditions at the wall ($\beta = 63.4^\circ$), as this should be the most energetically favorable state for dimensions ($\sim 10 \mu\text{m}$) much smaller than the magnetic healing length ($\xi_H \sim 1 \text{ mm}$).

If we inspect the observed shifts in more detail, we do observe that the mean of the line shape asymmetrically moves away from the Larmor frequency, which is illustrated in figure 4.17, which forms a 2D projection of figure 4.15. Not only does the absorption peak becomes broader, as expected as the angle between the $\hat{\mathbf{n}}$ -vector and the magnetic field varies over the sample, but becomes also asymmetric with the minimum of this absorption line being positioned at the left side. This means that in most part of the sample the $\hat{\mathbf{n}}$ -vector has an angle with the magnetic field corresponding to this line segment, and as this minimum is most left of the broadened absorption line, it seems reasonable to believe that it corresponds to the maximal achievable angle, which is 63.4° . This idea is strengthened by the realization that for these narrow cylinders (small compared to the magnetic healing length) the most energetically favorable configuration will be determined by the boundary conditions at the wall, hence $\beta = 63.4^\circ$.

From this point we do assume that the peak (minimum) of the absorption spectrum corresponds to $\beta = 63.4^\circ$. This is the shift we want to plot as function of temperature. The problem with this data set is that the SNR is around 3 in the normal phase, but becomes worse below the transition temperature T_c , when the absorption spectrum gets wider and the susceptibility reduces. In addition the right absorption line moves over the middle peak (signal from the channels), which increases the difficulty to determine the exact peak position.

The position of the absorption peak for the higher temperatures (around T_c) was determined with one single scan; for the lower temperatures scans needed to be averaged to get high enough SNR (for which the temperature was considered to be the averaged temperature of the scans). This averaging gradually increased to 25 line shapes for the lowest temperatures. The SNR for the right peak was better than for the left peak, and the shifts could be observed for temperatures till $0.6 T_c$. For the left peak the SNR ⁵⁵ becomes too low for temperatures under $0.85 T_c$. This is partly due to lower SNR for the left peak, but also because of the subtraction of the baseline,

⁵⁵One can consider averaging even more, but if one averages over a too long temperature range the absorption spectrums will hardly overlap (as they have shifted too much). In that case averaging does not even help to increase the SNR.

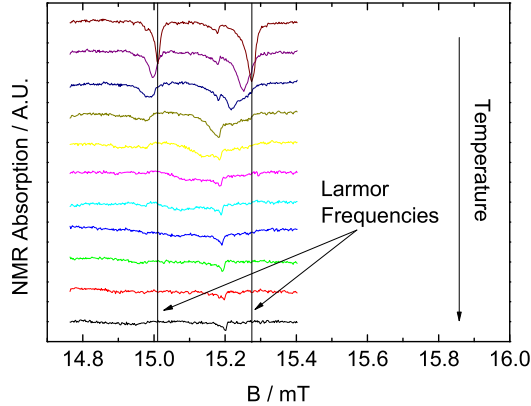


Figure 4.17: This is a 2D projection of figure 4.15. The colors of the absorption lines do represent the same temperature. The function of this illustration is to show how the absorption line shifts away from the Larmor frequency. All line segments away from the Larmor frequency do correspond with a β larger than 0 and maximally 63.4° . Not only becomes the absorption peak broader, as expected as the \hat{n} -vector bends over the sample, but also becomes asymmetric with the minimum of this absorption line positioned at the left side. It means that the \hat{n} -vector has in most part of the sample an angle with the magnetic field corresponding to this line segment, and as this minimum is most left of the broadened absorption line, it is reasonable that it would correspond to the maximal achievable angle, which is 63.4° . This idea is strengthened by the realization that for these narrow cylinders (small compared to the magnetic healing length) the most energetically favorable configuration will be determined by the boundary conditions at the wall, hence $\beta = 63.4^\circ$.

which is for the raw data much more curved at the position of the left peak than for the right peak.

As already mentioned, for some peculiar reason the resonance frequencies of the absorption spectrums seem to happen at different magnetic fields. This has probably to do with the distribution of the magnetic field lines through the sample, but (at least in the normal state) we do know they should all be in resonance at the Larmor frequency, which is in our case equal to the resonance frequency of the tank circuit, hence 488867 Hz. For this reason all shifts are expressed relative to this frequency. So the frequency shifts of the absorption peaks, which we believe to correspond with $\beta = 63.4^\circ$, as function of reduced temperature for 0.5 and 4 bar are plotted in figures 4.18 and 4.19, respectively. All curves are fitted with equation (4.38).

The fit parameters, which are obtained by least square fit methods, are not deter-

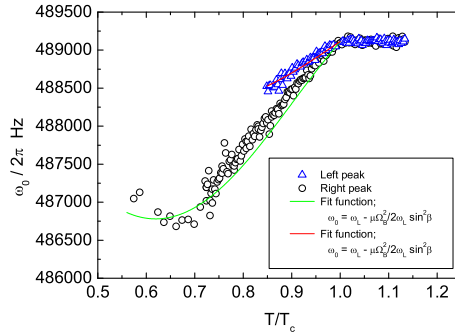


Figure 4.18: Shifts of the absorption peak at 0.5 bar, for $\beta = 63.4^\circ$. The blue open triangles and the black open circles correspond to the shifts of the left and right peak in figure 4.15, respectively. Both shifts are fitted with equation (4.38), for which the results are discussed in the text. The shift of the blue data is less than the black data, from which it can be concluded that the solid/liquid ratio must be higher. Interesting to observe in the black data is that for low enough temperature the shift is reversed, because the magnetization of the solid is still increasing, while the susceptibility of the superfluid is decreasing.

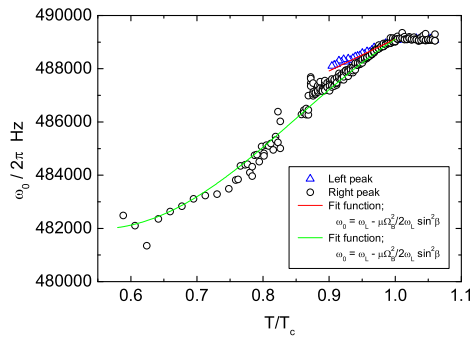


Figure 4.19: Shifts of the absorption peak at 4.0 bar, for $\beta = 63.4^\circ$. The blue open triangles and the black open circles correspond to the shifts of the left and right peak in figure 4.15, respectively. Both shifts are fitted with equation (4.38), for which the results are discussed in the text. The shift of the blue data is less than the black data, from which it can be concluded that the solid/liquid ratio must be higher. The lack of black data points near $0.85 T_c$ is due to the difficulty to determine the positions of the peak as it shifts through the middle peak.

mined for each pressure individually. For each pressure we filled in the known values of equations (4.38) and (4.39), leaving only the temperature dependence and the fit parameters n_{sol}/V_{liq} and θ . We do assume that the Curie-Weiss constant θ and the amount of solid atoms (in mole) per liquid volume n_{sol}/V_{liq} are the same for all (our used) pressures and temperatures. It means that these parameters could be determined by multiple fits at different pressures. The parameters which collectively gave the best fit of the data was considered to be most reliable of describing the conditions of our cell. The data for 0.5 and 4 bar inclusive these fits are put in figure 4.18 and 4.19.

In summary, it was not easy to fit these data as the main problems were:

- The SNR for the lowest temperatures was very small.
- The signal of opens spaces are still an ensemble of many space, which have in principle all their own n_{sol}/V_{liq} ratio.
- The absorption peak was considered to belong to $\beta \approx 63.4^\circ$, which can be in reality smaller.
- Results were obscured as the signal shift through other absorption lines.

Nevertheless, we do see that this model describe the physics quite well. In detail there may be some deviations, which are likely due to uncertainty about the exact geometry of our system.

In overall the best fit parameter for n_{sol}/V_{liq} was 68.95 and 17.85 mole m^{-3} for left and right peak, respectively. θ was found to be 0.3 mK. Of course this ratio is a bit different from the ideal case, as the open spaces will be packed worse and/or are partly filled with stycast. Nevertheless, as we assume that the left peak is indeed from the signal between the fibers and the right peak at the wall, the calculation does not differ more than a factor 1.7 compared to the ideal calculation. This is surprisingly good as the density of the solid layer is in general hard to guess, and the fibers seem to be well packed. It should be mentioned that most probably the smallest spaces had difficulties to be completely filled with stycast. As in the case of the fibers they were typically sucked in the stycast for 5 mm. If the same thing happened for the smallest spaces between the fibers, it is not a surprise that these spaces became available, when the fibers were reopened.

This model is very helpful to understand any deviation of the bulk B-phase (or A-phase) in samples with relative high solid to liquid ratios. For example the data obtained in aerogel, see [127] and [132]. These samples are highly porous (typically 98%), and as a consequence surface and volume are randomly distributed over the sample. If one deals with the B-phase in such a sample, one can imagine that the $\hat{\mathbf{n}}$ -vector is also randomly distributed over the sample. The advantage of our geometries is that there is a clear orientation of the $\hat{\mathbf{n}}$ -vector, for which evidently a shift is expected. These shifts are visible in our data, from which it is clear (if one compares with the bulk) that the interaction (rapid exchange) with the solid does influence the

amplitude of the total shift. One can even see, best noticeable in figure 4.18, that for low enough temperatures the total magnetization of the solid (also the decrease of the susceptibility of the B-phase) is enough to shift back the absorption peak in the direction of the Larmor frequency. What is a bit unclear to the author is how 'far' the solid influences the liquid. It is clear that there will be an exchange between the atoms at the solid/liquid interface, but unclear how the interaction reduces over space. In our geometry there is clear spatial distribution between wall and volume, this in contrast for example with aerogel, for which one can imagine that the atoms near the wall (still most atoms are in the liquid) are more influenced by this rapid exchange than the atoms in the center. An additional difficulty, to see if some atoms are more affected, is that the Cooper pairs at the wall are also the ones for which the \hat{n} -vector has the largest angle β with respect to the magnetic field. Nevertheless, it seems that the whole liquid is coherently influenced by the solid, for which it looks like that this model is also valid for cylindrical-like samples.

4.6 Conclusion

We have shown that the channels in the PCF are good candidates for long cylindrical samples. They could be made macroscopically long, while the diameter had only little deviation. Also the roughness was small and had only an amplitude of approximately 0.5 nm, the same order of magnitude as the size of ^3He atom. It also seems to have a correlation length of 26.5 nm, which may be close to the size of the Cooper pairs of ^3He , but as this amplitude is small as well, it was never considered a problem to form a superfluid inside these channels. We conclude that this geometry would be perfect to study exotic superfluid states, like the polar phase and/axial phases at low pressures.

As the filling factor of this sample is extremely small, we were very delighted that we obtained such high SNR (~ 3), due to the ultra-high Q of our tank circuit, for our desirable temperature sweeps combined with our used bandwidth (~ 2.6 Hz). So, it turned out that the weakly coupled transformer technique was suitable to measure a μmole of ^3He *at low frequencies*, and as this is a completely passive system, it is suitable to continue measurement for weeks.

The failure to observe any frequency shift (relative to the Larmor frequency) made it hard to conclude with any certainty if there was a superfluid acquired inside these channels. At least it can be concluded that the superfluid B-phase was not observed for temperatures at 300 μK till 10 bar. By itself a surprising result, as the suppression was (theoretically) not expected to be that much. To exclude that any polar or axial state was formed, a modification of the system is required.

As the production of the bundle of fibers apparently left some open space between them, it was a fortunate opportunity to study the superfluid in these kinds of vol-

umes. This study was definitely made easier as for some unknown reasons locally the magnetic field in this volumes was slightly different, so the NMR signals corresponding to the volumes could be distinguished. As the cross section of these volumes allows the formation of the B-phase, it is an interesting size in the sense that the total magnetization of the solid (2 layers of ^3He adsorbed to the wall) comes close to that of the liquid. This in a perfect condition to study the rapid exchange between the solid and liquid, and it is found that even in a cylindrically shaped volume the liquid coherently interacts with the solid layer.

Chapter 5

Cold valve

5.1 A high performance normally-closed solenoid-actuated cold valve

An electromagnetically driven normally-closed valve for liquid helium is presented, which is meant to regulate the input flow to a 1 K pot. An earlier design is modified to be normally-closed (not actuated) and tuned for durability and reliability. Here a new feature is presented which prevents seat deformation at room temperature and provides comfort and durability for intensive use.

5.2 Description of the design

Recently Bueno *et al.* [133] presented a low temperature valve for liquid helium that uses a magnetic field gradient and a permanent magnet to operate. The valve uses a ruby ball on a torlon seat to close. The ease of use and the reliability of the rather small valve has turned out to be quite convenient, and the valve is ideally suited to regulate the flow of helium to the 1 K pot of a dilution refrigerator. An essential feature of the valve is that it needs an actuating current to be closed, so in case of a power failure the valve opens automatically. In certain applications [134] it is important that the valve is closed when there is a power failure, so the possibility was investigated to design, construct and test a normally-closed valve, which would be opened by an electric current. This was less straightforward than expected, and several novel ideas are incorporated in the valve described below.

The new design is based on the earlier presented valve, which was normally-open [133]. All essential aspects can be seen in figure 5.1. A coil spring [135] is placed underneath the permanent magnet [136], which provides the closing force when not actuated. The superconducting coils [137] are counter-wound to create a linear-gradient magnetic field. The 2 times 1300 windings are made carefully to minimize the risk of quenching due to magnetic forces upon individual wires. In- and outlet are both

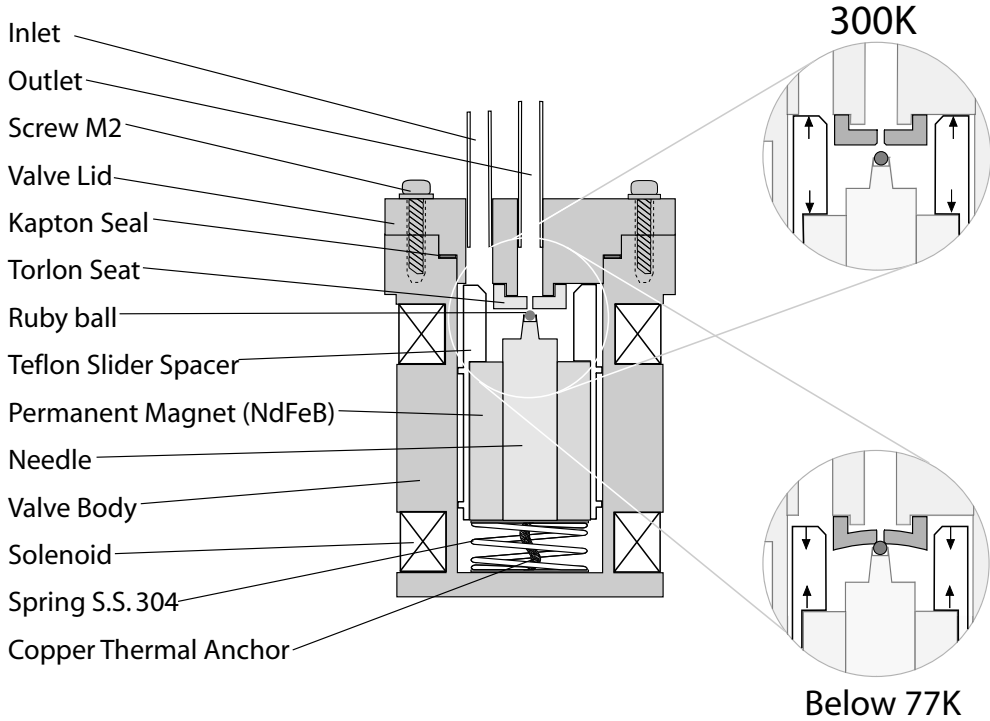


Figure 5.1: Schematic view of the valve, showing the components and nomenclature. The upper detail shows the situation at 300K: the valve is slightly open due to an expanded teflon spacer. The lower detail shows the situation at cryogenic temperatures: the teflon spacer is contracted and allows the ruby tip to press onto the seat. The seat's contact edge is elastically deformed, but the seat itself deflects as a membrane, which is shown in exaggerated form.

positioned in the valve lid, which is sealed by a greaseless kapton ring [138]. The brass needle inside the permanent magnet houses a 1 mm diameter ruby, which is the valve tip. The ruby presses on a torlon [139] seat, which has a 0.5 mm diameter hole and is glued to the lid. The permanent magnet is surrounded by a teflon slider, which guides its movement inside the valve body. Only two thin radial strips are in contact with the valve wall, to minimize friction. The top part of the teflon slider acts as spacer and functions on the basis of thermal contraction, which will be clarified below. Thermal anchoring, consisting of two copper disks interconnected by silver epoxy and soft copper braid, ensures proper thermal contact between the valve body and the permanent magnet, needle and teflon slider. The valve is 38 mm in height and 26 mm in diameter.

T (K)	$K_{calculated}$ (N mm ⁻¹)	$K_{experimental}$ (N mm ⁻¹)
300	2.71	2.70
77	2.95	3.02
4	2.90	–

Table 5.1: Calculated spring constants of an ideal compression spring [141] from literature values of the spring material properties, and experimentally determined values at different temperatures. The spring constant at 4 K is not measured.

5.3 Operating principles

5.3.1 Actuation

The closing force is delivered by the stainless steel spring which is compressed inside the valve boring. Proper seating and radially homogeneously distributed forces are achieved by end treatments of the spring, such as reducing pitch of the spring ends and grinding them flat [140]. From table 5.1 can be seen that this did not influence the spring behavior.

The actuation force comes from a force in opposite direction on the permanent magnet as a result of the linear gradient magnetic field from the two solenoids. The gradient is constant in axial direction, but not in the direction perpendicular to the axis. The magnet has the shape of a cylinder, where the brass needle resides in a hole through the center. Taking this into account the force per unit of current is calculated, by

$$F_z = \int_V \mu \frac{\partial B}{\partial z} dV, \quad (5.1)$$

with the gradient $\frac{\partial B}{\partial z}$ in Tesla per meter and μ the magnetic moment of the stack of permanent magnets, given by

$$\mu = \int_V \frac{B_{rem}}{\mu_0} dV = \int_V M dV, \quad (5.2)$$

with B_{rem} the remanent magnetic field, M the remanent magnetization, and μ_0 the permeability of free space. The volume of the stack of permanent magnets is the actual volume to integrate over, and taking into account the axial and radial symmetry Equation (5.1) becomes

$$F_z = 2\pi M h \int_{r_i}^{r_o} \frac{\partial B(z, r)}{\partial z} dr, \quad (5.3)$$

where h is the height of the permanent magnets and r_i , r_o the inner and outer radius of the magnets, respectively. The calculated and the measured values are displayed in table 5.2. Measuring the actuation force is done by lifting the permanent magnet at room temperature by moderate currents. From the weight of the magnet and

	calculated	measured
actuation force (N)	11.5	10.3
opening current (A)	1.0	1.05 ¹

Table 5.2: Calculated and measured actuation force and valve opening point at LHe temperatures.

the measured current the actuation force per A is obtained. Using the calculated spring constant at 4 K from table 5.2 the opening point is calculated and measured by experiment. The values coincide well, showing no peculiarities.

5.3.2 Closure: Seat and Ruby

Valve closure is always based on the interaction between seat and tip material. In this case the tip is a 1.0 mm smooth ruby ball and the seat is a high quality plastic (polyamide-imide: PAI) known as torlon [139]. Torlon is strong and remains flexible even at LHe temperature, where other plastics become brittle. The ruby presses the seat at a contact edge to close the 0.5 mm orifice. It is the elastic deformation of this contact edge which ensures (superfluid) helium leak-tightness. The larger the elastic deformation the better the closure, however a material can only deform *elastically* up to the yield point from where it starts to deform *plastically*. By comparing controlled seat contact edge (de)formation and finite element analysis, a model is constructed. The model shows that an elastic deformation in the contact edge of 70 – 100% of the yield point is where the valve closure is superfluid leak-tight and consistent. When the valve is closed rapidly and the permanent magnet and needle accelerate too fast towards the seat, the ruby strikes the seat and the forces involved could still cause plastic deformation. This is minimized by the fact that the seat as a whole can deflect as a membrane (see figure 5.1 and Ref. [138]). It is experimentally confirmed that the impact is much better absorbed this way and the contact edge deforms much less compared to the case where the seat cannot deflect like a membrane. The durability is improved, and the elastic deformation in the contact edge is only 5 to 8% less than in the non-membrane-like construction.

5.3.3 Teflon spacer

In the previous section it is argued and shown that closure depends on elastic deformation of the seat's contact edge: the higher the elastic deformation, the better the closure. However maximum elastic deformation is determined by the yield strength of the material, which for torlon is only 152 MPa at room temperature but already 216 MPa at 77K. To obtain a sufficiently large elastic deformation at LHe temperature due to the normally-closing spring force, this force would cause *plastic* deformation on the seat at room temperature, due to the lower yield strength of the torlon. To

¹Current increased with 0.05 A per step.

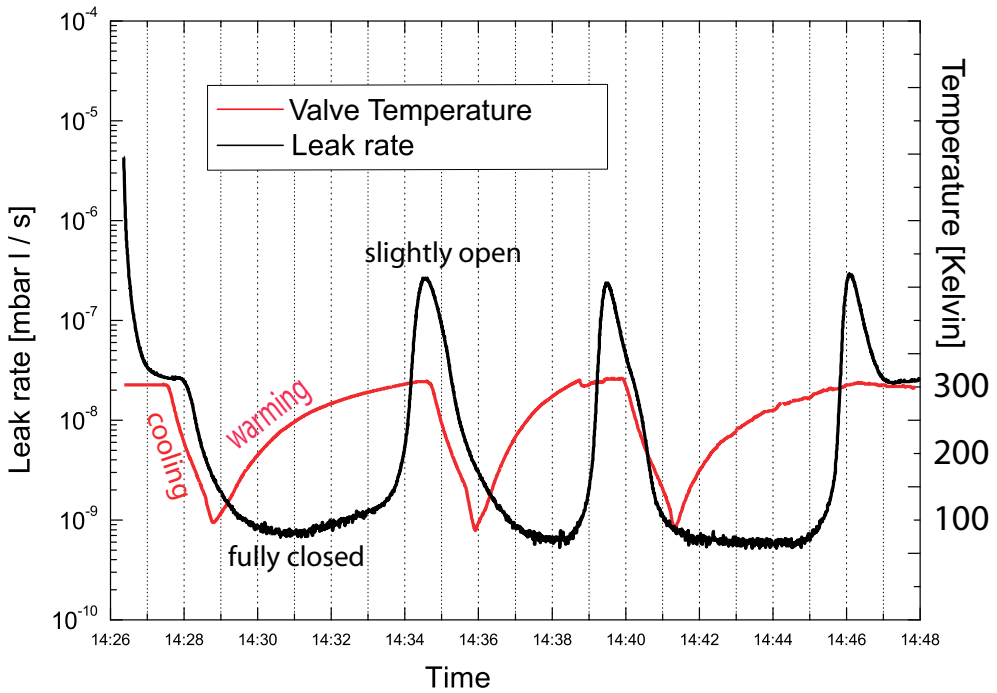


Figure 5.2: Graph showing the functioning of the teflon spacer. When cooling the spacer contracts, and the leak rate, due to a few mbar of helium pressure difference, drops to 10^{-9} mbar l s $^{-1}$ (back ground pressure): the valve is closed. When warming to room temperature the spacer expands and lifts the tip from the seat, which is confirmed by the increasing leak rate. This cycle is repeated three times to show consistency.

avoid this behavior the teflon spacer is introduced. At room temperature the length of the spacer is such that it takes all the force of the spring and thus prevents the ruby to exert force on the seat. When the valve is cooled down to LHe temperature, the teflon spacer will start to contract, and also the yield strength of the torlon seat starts to increase. At the moment that the spacer is contracted so much that the ruby can press fully on the seat, the yield strength is large enough to ensure only elastic deformation. When warming again to room temperature the reverse happens: The seat's yield strength drops, but the spacer expands and starts taking a part of the force of the spring and thus prevents plastic deformation of the seat. The spacer only allows the full spring force on the seat at sufficiently low temperature and thus guar-

antees maximum elastic deformation and therefore optimal closure. Apart from the protective function the spacer has more advantages: It allows convenient and quick assembly of the valve. The risk of damaging the seat's contact edge, when mounting the valve lid, is eliminated, simply because the ruby cannot touch the contact edge. It prevents occasional dust particles (the main reason for valve failure) on the contact edge to get pressed into the material when warming to room temperature. The seat can in most cases be cleaned easily, to be leak-tight again when reused.

The spacer has been used for closing spring forces of up to 40 N and worked fine, showing no signs of wear or malfunctioning after many cooling cycles.

5.3.4 Thermal contact

The functioning of the superconducting solenoids, the seat and the teflon spacer all rely upon well controlled temperature changes. The additional copper thermal anchoring establishes proper thermal contact between the permanent magnet and the teflon slider/spacer. It ensures that all parts cool and warm evenly, so it cannot happen for instance that the seat is already warm (and thus weak) while the ruby is still exerting force because the spacer is not expanded yet. Calculations on thermal conduction show that the maximum characteristic time to get to thermal equilibrium is about 100 seconds, which is much shorter than the minimum time required to warming or cooling the valve.

5.4 Valve performance

A valve setup which needed a 12 N closing force by a spring with a spring constant of about 3 N mm^{-1} , was tested thoroughly. An actuation current below 2.0 A was needed for full opening. A flow characteristic can be seen in figure 5.3, where the maximum flow of 7 mmole s^{-1} was a limitation of the connection lines in that experiment (the maximum flow through the valve itself is at least ten times higher). Due to the precisely machined teflon slider the hysteresis is low and no stick-slip motion of the needle is observed in the flow, as was the case for earlier sliders made out of PEI (polyetherimide) and Araldite. Valves have been thermally cycled at least 20 times and at each cool down the valve was actuated at least 25 times by current step sizes of 0.2 A maximum, showing no detectable leak. Often used seats still showed leak tightness for superfluid helium. A particular seat which was closed *rapidly* (current switched from 1.8 to 0.0 A, so the ruby really impacts the seat) for 150 times, had many normal actuations and several seat cleansings showed a leak rate of only $5 \cdot 10^{-9} \text{ mmole s}^{-1}$ before it was replaced. The valves with 12 N closing force showed no detectable leak (neither the ruby/torlon seat nor the kapton seal) for pressure differences of 10 bar. Even the flow control ability showed very promising results (also for very *low* flows, as seen in the inset of figure 5.3). Due to the teflon spacer, the assembly of the valves is easy and fast, allowing convenient replacement or cleaning of the seat.

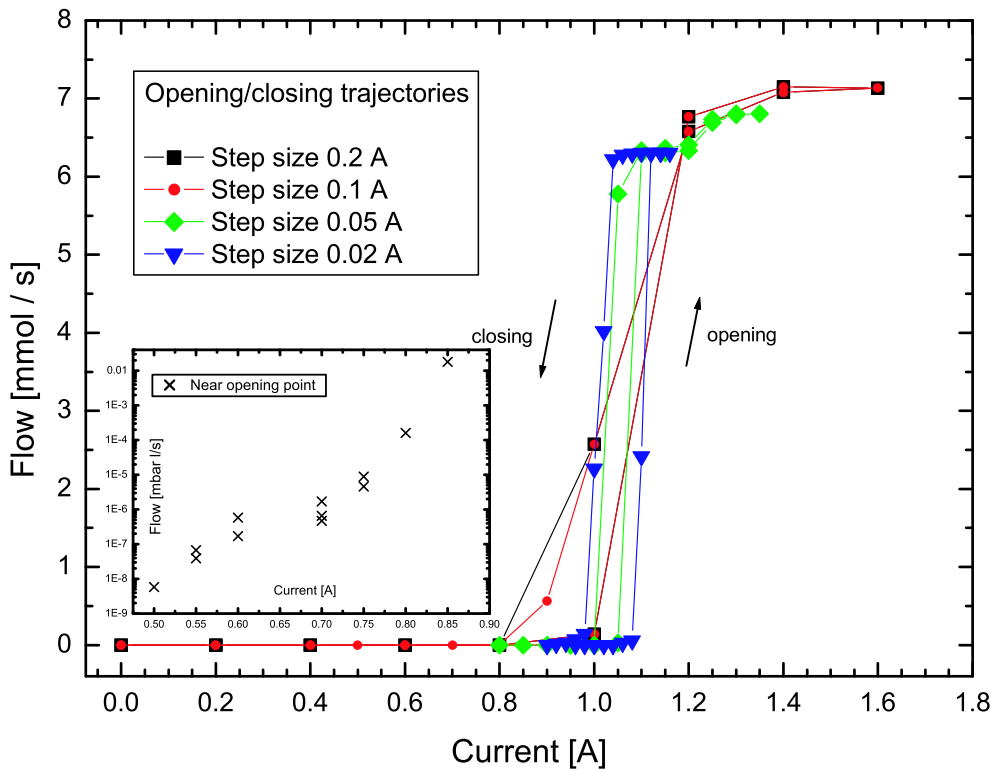


Figure 5.3: The flow through the valve versus the actuating current, that gradually opens the valve; the maximum flow is not set by the valve itself, but by the impedance of the connecting capillaries; the inset shows the flow rate near the opening point.

Appendix A

Appendix

A.1 Pressure dependent quantities and constants of helium-3

Most of the numbers presented in this appendix are taken from W.P. Halperin's ³He Calculator [142]. Their numbers based on the references [143], [144], [145] and [146].

Quantity	Symbol	Value	Units
modified Planck constant	\hbar	$1.0545727 \cdot 10^{-34}$	J s
gyromagnetic ratio ³ He	γ	$20.3801587 \cdot 10^7$	rad Hz T ⁻¹
Boltzmann constant	k_B	$1.380658 \cdot 10^{-23}$	J K ⁻¹
vacuum permeability	μ_0	$4\pi \cdot 10^{-7}$	N A ⁻²
³ He mass	m	$5.008234 \cdot 10^{-27}$	kg
cut off energy	ε_c	$\sim 0.7 k_B$	J
Riemann Zeta function	$\zeta(3)$	1.202	-

P bar	m^*/m	F_0^a	F_1^s	v_F m s^{-1}	T_c mK	P bar	m^*/m	F_0^a	F_1^s	v_F m s^{-1}	T_c mK
0.0	2.80	-0.701	5.40	59.03	0.93	3.5	3.22	-0.720	6.65	53.07	1.34
0.1	2.81	-0.701	5.44	58.83	0.94	3.6	3.23	-0.721	6.68	52.93	1.35
0.2	2.83	-0.702	5.48	58.64	0.96	3.7	3.24	-0.721	6.72	52.78	1.36
0.3	2.84	-0.703	5.52	58.45	0.97	3.8	3.25	-0.722	6.75	52.64	1.37
0.4	2.85	-0.703	5.55	58.26	0.98	3.9	3.26	-0.722	6.78	52.50	1.38
0.5	2.86	-0.704	5.59	58.07	1.00	4.0	3.27	-0.722	6.81	52.36	1.39
0.6	2.88	-0.704	5.63	57.88	1.01	4.1	3.28	-0.723	6.85	52.22	1.40
0.7	2.89	-0.705	5.67	57.69	1.02	4.2	3.29	-0.723	6.88	52.08	1.41
0.8	2.90	-0.706	5.70	57.51	1.04	4.3	3.30	-0.724	6.91	51.94	1.42
0.9	2.91	-0.706	5.74	57.33	1.05	4.4	3.31	-0.724	6.94	51.80	1.42
1.0	2.93	-0.707	5.78	57.14	1.06	4.5	3.32	-0.725	6.97	51.67	1.43
1.1	2.94	-0.707	5.82	56.96	1.07	4.6	3.34	-0.725	7.01	51.54	1.44
1.2	2.95	-0.708	5.85	56.79	1.09	4.7	3.35	-0.726	7.04	51.40	1.45
1.3	2.96	-0.708	5.89	56.61	1.10	4.8	3.36	-0.726	7.07	51.27	1.46
1.4	2.97	-0.709	5.92	56.43	1.11	4.9	3.37	-0.727	7.10	51.14	1.47
1.5	2.99	-0.710	5.96	56.26	1.12	5.0	3.38	-0.727	7.13	51.01	1.48
1.6	3.00	-0.710	6.00	56.09	1.14	5.1	3.39	-0.727	7.16	50.88	1.49
1.7	3.01	-0.711	6.03	55.92	1.15	5.2	3.40	-0.728	7.19	50.75	1.49
1.8	3.02	-0.711	6.07	55.75	1.16	5.3	3.41	-0.728	7.23	50.63	1.50
1.9	3.03	-0.712	6.10	55.58	1.17	5.4	3.42	-0.729	7.26	50.50	1.51
2.0	3.05	-0.712	6.14	55.41	1.18	5.5	3.43	-0.729	7.29	50.38	1.52
2.1	3.06	-0.713	6.17	55.25	1.19	5.6	3.44	-0.729	7.32	50.25	1.53
2.2	3.07	-0.713	6.21	55.08	1.20	5.7	3.45	-0.730	7.35	50.13	1.54
2.3	3.08	-0.714	6.24	54.92	1.22	5.8	3.46	-0.730	7.38	50.01	1.54
2.4	3.09	-0.714	6.28	54.76	1.23	5.9	3.47	-0.731	7.41	49.89	1.55
2.5	3.10	-0.715	6.31	54.60	1.24	6.0	3.48	-0.731	7.44	49.77	1.56
2.6	3.12	-0.716	6.35	54.44	1.25	6.1	3.49	-0.731	7.47	49.65	1.57
2.7	3.13	-0.716	6.38	54.28	1.26	6.2	3.50	-0.732	7.50	49.53	1.58
2.8	3.14	-0.717	6.42	54.13	1.27	6.3	3.51	-0.732	7.53	49.42	1.58
2.9	3.15	-0.717	6.45	53.97	1.28	6.4	3.52	-0.733	7.56	49.30	1.59
3.0	3.16	-0.718	6.48	53.82	1.29	6.5	3.53	-0.733	7.59	49.18	1.60
3.1	3.17	-0.718	6.52	53.67	1.30	6.6	3.54	-0.733	7.62	49.07	1.61
3.2	3.18	-0.719	6.55	53.52	1.31	6.7	3.55	-0.734	7.65	48.96	1.61
3.3	3.19	-0.719	6.58	53.37	1.32	6.8	3.56	-0.734	7.68	48.85	1.62
3.4	3.21	-0.720	6.62	53.22	1.33	6.9	3.57	-0.735	7.70	48.73	1.63

A.2 Gap function

In the case of $^3\text{He-B}$ the gap function is isotropic, see figure 1.3. Since we deal with p-wave pairing, the gap function for this particular phase has the same symmetry as for the s-wave pairing (BCS theory). The behavior of the gap near T_c is given by

$$\Delta(T) \approx 3.06k_B T_c \sqrt{1 - \frac{T}{T_c}}, \quad (\text{A.1})$$

and for $T = 0$ the gap equals

$$\Delta(0) \approx 1.76k_B T_c. \quad (\text{A.2})$$

The gap function is not analytically solvable, however it is numerically solved by Mühlshlegel [147] from which we took the calculated gap values. The Δ^2 as function of temperature is plotted in figure A.1. The temperature dependence is fitted with a 4th order polynomial.

Best fit is obtained with least squares fitting techniques, and is given by

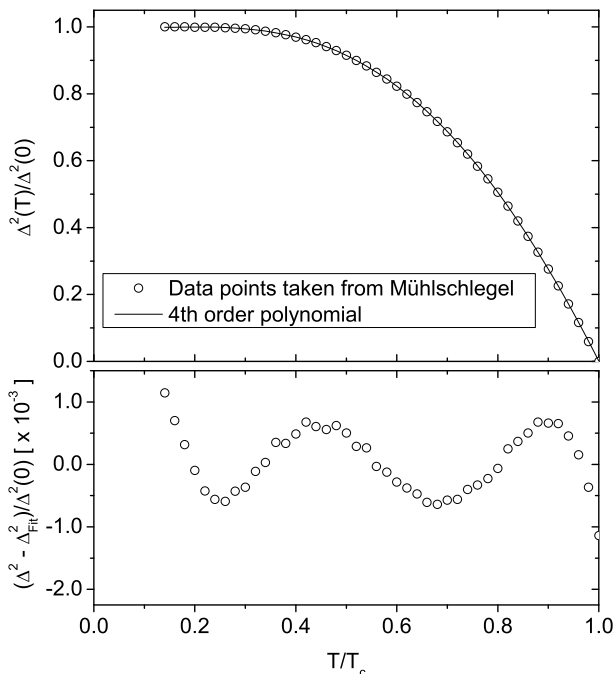


Figure A.1: Upper graph shows the squared gap Δ^2 as function of temperature and fitted by a 4th order polynomial. Lower graph shows the difference between the fit function and the numerical values.

$$\begin{aligned} \frac{\Delta(T)^2}{\Delta(0)^2} = & 1.00459 - 0.15842(T/T_c) + 1.24905(T/T_c)^2 \\ & - 3.06569(T/T_c)^3 + 0.97161(T/T_c)^4. \end{aligned} \quad (\text{A.3})$$

The differences between the numerical values and fit function is typically less than 0.1 %, this is sufficient for the purpose of this thesis.

A.3 Susceptibility of the B-phase of helium-3

The spin susceptibility in the normal phase, given in equation (1.5), is hardly temperature dependent when $T \ll T_F$. However, if one cools below T_c the spins will form a spin triplet configuration. At the lowest temperatures the populations will be equally distributed over these three states. Consequently, the susceptibility should reduce to $2/3 \chi_N$, as the $m_s = 0$ state (spin up-down state) does not respond to magnetic fields. Simultaneously, the 'screening cloud' effect of the atom in the normal phase decreases

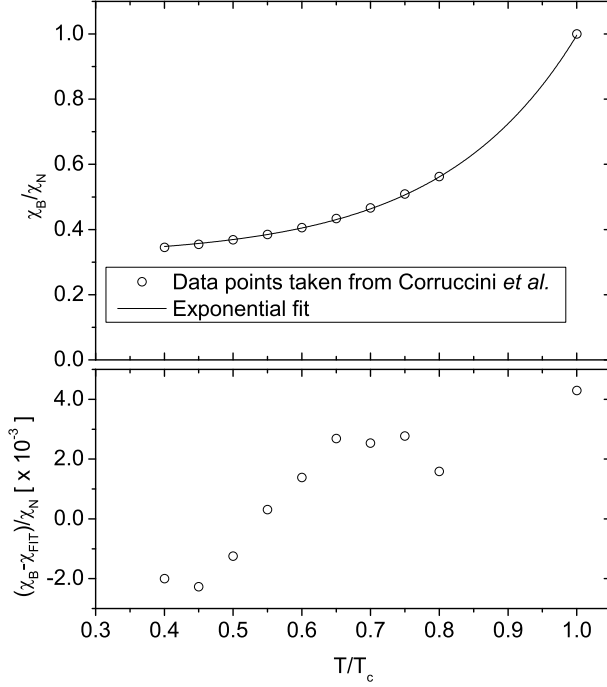


Figure A.2: Upper graph is the normalized susceptibility of the $^3\text{He-B}$ as function of temperature and fitted by an exponential function. Lower graph is the difference between the fit function and the susceptibility χ_B/χ_N .

in the superfluid phase as well [148]. At zero temperature it results in a susceptibility of the B-phase χ_B of approximately $1/3 \chi_N$.

As is shown in literature the temperature dependence of χ_B , for all pressures, show approximately the same universal law as function of T/T_c . In figure A.2 the susceptibility as function of temperature is plotted, data is taken from [149] [38].

The fit, obtained with least squares fitting techniques, is given by

$$\frac{\chi_B(T)}{\chi_N} = 0.00417 \exp\left(5.09372 \frac{T}{T_c}\right) + 0.31601. \quad (\text{A.4})$$

While the data taken from literature are obtained at pressures higher than 18 bar, we assume that the behavior of equation (A.4) will not change significantly for lower pressures. Well it is most likely, that it may differ in detail. However, it should not take off much of the quantitatively description of the susceptibility's temperature dependence.

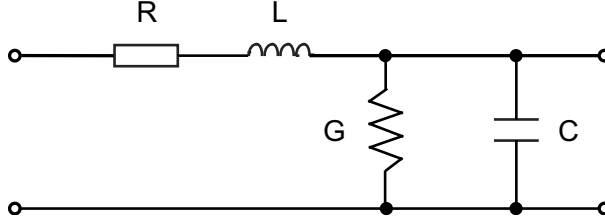


Figure A.3: Schematic representation of the elementary component of a transmission line.

A.4 Transmission Line

The coaxial cable or transmission line can be seen as a repetition of elementary components. Such an elementary component is shown in figure A.3. Here the conductor's resistance is represented by a series resistor R . The self-inductance is represented by a series inductor L . The parasitic capacitance between the shield and core is represented by a shunt capacitor C , and its losses by a shunt resistor G . As the transmission line in principle exists of an infinite series of elements the components are specified per unit length.

Our experiments are performed at relatively low-frequencies (500 kHz), for which we assume that the self-inductance of the transmission line does not play an important role, and will be neglected for low-frequencies. Also the losses due to the conductor's resistance R are considerably larger than in G , so we neglect G , leaving only the capacitor and resistor in the elementary component of the transmission line.

In our set-up the transmission lines are coax cables, of which the outer shield is connected to the ground. The transmission lines are 2 meters long, due to the length of the cryostat, resulting in a relatively high (total) parasitic capacitance, which coincides with low impedance $Z_{C_{Total}}$ between shield and core. In our set-up the transmission lines are connected between a high input impedance (high Q tank circuit) and high output impedances (pre-amplifier), meaning that the current through the transmission line is 'short circuited' by Z_C to the ground.

Figure A.4 illustrates the situation of N elementary components connected between a high in- and output impedance. The total current I_{Total} coming from the input impedance will be divided over the parasitic capacitance of each element. For our transmission lines we claim that $Z_C \gg R$ for each element, and we even assume that the total resistance of the transmission line, $R_{Total} = R_1 + R_2 + R_3 + \dots + R_{N-1} + R_N$, is much smaller than the total impedance $Z_{C_{Total}}$.

In that case the current will be (approximately) equally divided over all the parasitic elements, hence $I_1 = I_2 = I_3 = \dots = I_{N-1} = I_N = I$, and the total parasitic capacitance $C_{P_{Total}}$ equals the (parallel) adding of each parasitic capacitance per element, hence $C_{P_{Total}} = C_1 + C_2 + C_3 + \dots + C_{N-1} + C_N = N \cdot C$. However, one correction with respect to the resistance should be made, the current through R_1 is much more than in R_N . It is important to know the proper effective resistance of the

transmission line for our simulation, because it determines the additional dissipation 'seen' in our tank circuit. We want to approximate the transmission line of figure A.4 with the total impedance of the coax capacitance in series with an effective resistor, hence $Z_{C_{total}} + R_{eff}$.

If we look how much elementary resistors are 'seen' by the current through each elementary component we get:

$$\begin{aligned} I_1 &\rightarrow R_1 \\ I_2 &\rightarrow R_1 + R_2 \\ I_3 &\rightarrow R_1 + R_2 + R_3 \\ &\vdots \\ I_{N-1} &\rightarrow R_1 + R_2 + R_3 + \dots + R_{N-1} \\ I_N &\rightarrow R_1 + R_2 + R_3 + \dots + R_{N-1} + R_N \end{aligned}$$

Using that all elementary components R are equal, $R_1 = R_2 = R_3 = \dots = R_{N-1} = R_N = R$, than in average the resistors 'seen' by the current is:

$$\begin{aligned} I_1 + I_2 + I_3 + \dots + I_{N-1} + I_N &\rightarrow \frac{NR + (N-1)R + \dots + 3R + 2R + R}{N} \\ I_1 + I_2 + I_3 + \dots + I_{N-1} + I_N &\rightarrow \frac{\sum_{i=1}^N iR}{N} \end{aligned}$$

Here $\sum_{i=1}^N i = \frac{(N-1+1)(N+1)}{2} = \frac{(N)(N+1)}{2}$, for large N the sum equals $N^2/2$. We assumed that all currents are equal; $I_1 = I_2 = I_3 = \dots = I_{N-1} = I_N = I$, this gives:

$$NI = I_{Total} \rightarrow \frac{NR}{2} = \frac{R_{Total}}{2} \equiv R_{eff} \equiv R_C$$

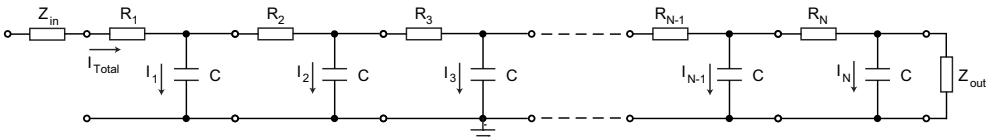


Figure A.4: Transmission line existing of N elementary components. In this representation L and G are neglected, due to relatively low operating frequency (500 kHz). The transmission is connected between a high in- and output impedance, consequently the current uses the parasitic capacitance of the transmission line to reach the ground.

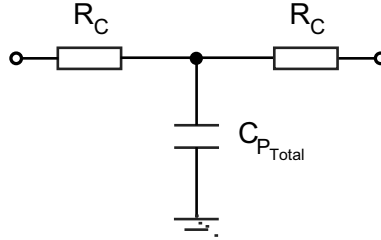


Figure A.5: The transmission line approximate for our conditions as a simple circuit. $C_{P_{Total}}$ is equal to the total parasitic capacitance and R_C is half the value of the total resistance of the transmission line.

For enough elements one can approximate the effective resistance by $R_{Total}/2 \equiv R_C$. So, with our imposed conditions we can approximate the transmission line, as illustrated in figure A.4, by a resistance R_C (half the value of the total resistance in the transmission line) and the total parasitic capacitance $C_{P_{Total}}$. However, one should take into account that the transmission line is symmetric when the current comes from the other direction, so to complete this symmetry the resistance R_C should be placed on both sides of $C_{P_{Total}}$, as illustrated in figure A.5 which is the circuit representing our transmission lines between room temperature and the tank circuit.

Bibliography

- [1] C. Garrod. *Statistical Mechanics and Thermodynamics*. Oxford university press, New York, Oxford, (1995).
- [2] C. Kittel. *Introduction to Solid State Physics*. John Wiley & Sons, New York, Chichester, seventh edition, (1996).
- [3] N.W. Ashcroft and N.D. Mermin. *Solid State Physics*. Holt, Rinehart, and Winston, New York, (1976).
- [4] A.L. Thomson, H. Meyer, and E.D. Adams. *Phys. Rev.* **128**, 509 (1962).
- [5] Helium Theory, Low Temperature Laboratory, Helsinki University of Technology, <http://ltl.tkk.fi/images/archive/ab.jpg>.
- [6] J. Bardeen, L.N. Cooper, and J.R. Schrieffer. *Phys. Rev.* **108**, 1175 (1957).
- [7] H. Kamerlingh Onnes. *Comm. Phys. Lab. Univ. Leiden; Nos.* **122 and 124**, (1911).
- [8] D.D. Osheroff, R.C. Richardson, and D.M. Lee. *Phys. Rev. Lett.* **28**, 885 (1972).
- [9] W.H. Keesom and K. Clusius. *Leiden Comm.* **219e**, (1930).
- [10] D.D. Osheroff. *Rev. Mod. Phys.* **69**, 667 (1997).
- [11] V.L. Ginzburg and L.D. Landau. *Zh. Eksp. Teor. Fiz.* **20**, 1064 (1950).
- [12] N.D. Mermin and C. Stare. *Phys. Rev. Lett.* **30**, 1135 (1973).
- [13] G. Barton and M.A. Moore. *J. Phys. C* **7**, 4220 (1974).
- [14] G. Barton and M.A. Moore. *J. Phys. C* **9**, 970 (1975).
- [15] R.B. Jones. *J. Phys. C* **10**, 657 (1977).
- [16] C. Bruder and D. Vollhardt. *Phys. Rev. B* **34**, 131 (1986).
- [17] W.F. Brinkman and P.W. Anderson. *Phys. Rev. A* **8**, 2732 (1973).

- [18] R. Balian and N.R. Werthamer. *Phys. Rev.* **131**, 1553 (1963).
- [19] D. Vollhardt and P. Wölfle. *The Superfluid Phases of Helium 3*. Taylor & Francis, London, New York, Philadelphia, (1990).
- [20] A.J. Leggett. *Phys. Rev. Lett.* **31**, 352 (1973).
- [21] A.J. Leggett. *Ann. Phys. (N.Y.)* **85**, 11 (1974).
- [22] A.J. Leggett. *Rev. Mod. Phys.* **47**, 331 (1975).
- [23] S. Takagi. *Prog. Theor. Phys.* **51**, 674 (1974).
- [24] K. Bedell and D. Pines. *Phys. Lett* **78A**, 281 (1980).
- [25] A.J. Leggett. *Phys. Rev. Lett.* **29**, 1227 (1972).
- [26] A.L. Fetter. *Quantum Statistics and the Many Body Problem*. Plenum, New York, 127 (1975).
- [27] L. Tewordt and N. Schopohl. *J. Low Temp. Phys.* **37**, 421 (1979).
- [28] N. Schopohl. *J. Low Temp. Phys.* **49**, 347 (1979).
- [29] P. Wölfle. *Phys. Lett* **47A**, 224 (1974).
- [30] M. Eggenkamp. *Ph.D. thesis, Leiden University*, (1998).
- [31] F. Pobell. *Matters and Methods at Low Temperatures*. Springer-Verlag, Berlin, (1992).
- [32] D.S. Greywall. *Phys. Rev. B* **27**, 2747 (1983).
- [33] R. Blaauwgeers, M. Blazkova, M. Človečko, V.B. Eltsov, R. de Graaf, J. Hosio, M. Krusius, D. Schmoranzler, W. Schoepe, L. Skrbek, P. Skyba, R.E. Solntsev, and D.E. Zmeev. *J. Low Temp. Phys.* **146**, 537 (2007).
- [34] C.B. Winkelmann, E. Collin, Y.M. Bunkov, and H. Godfrin. *J. Low Temp. Phys.* **135**, 3 (2004).
- [35] D.D. Osheroff, W.J. Gully, R.C. Richardson, and D.M. Lee. *Phys. Rev. Lett.* **29**, 920 (1972).
- [36] D.D. Osheroff and W.F. Brinkman. *Phys. Rev. Lett.* **32**, 584 (1974).
- [37] D.N. Paulson, R.T. Johnson, and J.C. Wheatley. *Phys. Rev. Lett.* **31**, 746 (1973).
- [38] L.R. Corruccini and D.D. Osheroff. *Phys. Rev. B* **17**, 126 (1978).
- [39] V. Ruutu, J. Koivuniemi, Ü. Parts, A. Hirai, and M. Krusius. *Physica B* **194 – 196**, 159 (1994).

- [40] J. Koivuniemi and M. Krusius. *Physica B* **284 – 288**, 2149 (2000).
- [41] M.G. Richards, A.R. Andrews, C.P. Lusher, and J. Schratte. *Rev. Sci. Instrum.* **57**, 404 (1986).
- [42] V.V. Dmitriev, I.V. Kosarev, and D.V. Ponarin. *Instruments and Experimental Techniques* **46**, 845 (2003).
- [43] M.R. Freeman, R.S. Germain, R.C. Richardson, M.L. Roukes, W.J. Gallagher, and M.B. Ketchen. *Appl. Phys. Lett.* **48**, 300 (1986).
- [44] L.V. Levitin, R.G. Bennett, A. Casey, B.P. Cowan, C.P. Lusher, J. Saunders, D. Drung, and Th. Schurig. *Appl. Phys. Lett.* **91**, 262507 (2007).
- [45] C.P. Slichter. *Principles of magnetic resonance*, volume I. Springer-Verlag, Berlin, (1978).
- [46] F. Bloch. *Phys. Rev. Lett.* **70**, 460 (1946).
- [47] Ultra high Q capacitor, Surface Mount Chip Capacitors. Syfer Technology Limited.
- [48] Tina-ti, special complimentary basic edition. Texas Instruments.
- [49] A.M. Portis. *Phys. Rev.* **91**, 1071 (1953).
- [50] W.E. Keller. *Helium-3 and Helium-4*. Plenum press, New York, (1969).
- [51] A. Finne, L. Grönberg, R. Blaauwgeers, V. B. Eltsov, G. Eska, M. Krusius, J. J. Ruohio, R. Schanen, and I. Suni. *Rev. Sci. Instrum.* **72**, 3682 (2001).
- [52] J. Ruohio. *Magneetti (Homemade)*, (1999).
- [53] J.R. Olson. *Cryogenics* **33**, 729 (1993).
- [54] A. Gauzzi, J. Le Cohec, G. Lamura, B.J. Jönsson, V.A. Gasparov, F.R. Ladan, B. Plaçais, P.A. Probst, D. Pavuna, and J. Bok. *Rev. Sci. Instrum.* **47**, 2147 (2000).
- [55] J.C. Wheatley. *Rev. Mod. Phys.* **47**, 415 (1975).
- [56] D. Candela, N. Masuhara, D.S. Sherrill, and D.O. Edwards. *J. Low Temp Phys.* **63**, 369 (1983).
- [57] G.F. Spencer and G.G. Ihas. *Phys. Rev. Lett.* **48**, 1118 (1982).
- [58] O.T. Ikkala, G.E. Volovik, P.J. Hakonen, Y.M. Bunkov, S.T. Islander, and G.A. Kharadze. *Zh. Eksp. Teor. Fiz Pis'ma Red.* **35**, 228 (1982).
- [59] D.D. Osheroff. *Physica* **90B + C**, 20 (1977).

- [60] H. Smith, W.F. Brinkman, and S. Engelsberg. *Phys. Rev. B* **15**, 199 (1977).
- [61] Y. R. Lin-Liu and K Maki. *Phys. Rev. B* **18**, 4724 (1978).
- [62] P.J. Hakonen, O.T. Ikkala, S.T. Islanders, O.V. Lounasmaa, and G.E. Volovik. *J. Low Temp. Phys.* **53**, 425 (1983).
- [63] K.W. Jacobsen and H. Smith. *J. Low Temp. Phys.* **52**, 527 (1983).
- [64] P.J. Hakonen, O.T. Ikkala, S.T. Islander, T.K. Markulla, P.M. Roubeau, K.M. Saloheimo, D.I. Garibashvili, and J.S. Tsakadze. *Cryogenics* **23**, 243 (1983).
- [65] B.C. Crooker, B. Hebral, and J.D. Reppy. *Physica B* **108**, 83 (1981).
- [66] R.H. Salmelin, J.M. Kynnäräinen, M.P. Berglund, and J.P. Pekola. *J. Low Temp. Phys.* **76**, 83 (1989).
- [67] J.D. Close, R.J. Zieve, and R.E. Packard. *Physica B* **165 – 166**, 57 (1990).
- [68] H.E. Hall, J.R. Hook, S. Wang, A.J. Armstrong, and T.D. Bevan. *Physica B* **194 – 196**, 41 (1994).
- [69] M. Kubota, T. Obata, R. Ishiguro, M. Yamashita, T. Igarashi, E. Hayata, O. Ishikawa, Y. Sasaki, N. Mikhin, M. Fukuda, V. Kovacic, and T. Mizusaki. *Physica B* **329 – 333**, 1577 (2003).
- [70] P. J. Hakonen, M. Krusius, M. M. Salomaa, R. H. Salmelin, J. T. Simola, A. D. Gongadze, G. E. Vachnadze, and G. A. Kharadze. *J. Low Temp. Phys.* **76**, 225 (1989).
- [71] A.J. Leggett. *Prog. Theor. Phys.* **51**, 1275 (1974).
- [72] C.M. Varma and N.R. Werthamer. *Phys. Rev.* **9**, 1465 (1974).
- [73] H.M. Bozler, M.E. Bernier, W.J. Gully, R.C. Richardson, and D.M. Lee. *Phys. Rev. Lett.* **32**, 875 (1974).
- [74] D.D. Osheroff, S. Engelsberg, W.F. Brinkman, and L.R. Corruccini. *Phys. Rev. Lett.* **34**, 190 (1975).
- [75] D.M. Lee and R.C. Richardson. *In the physics of liquid an solid Helium*, volume III. Wiley Interscience, New York, Chapter 4 (1978).
- [76] P.G. deGennes. *Phys. Lett. A* **44**, 271 (1973).
- [77] G.F. Spencer and G.G. Ihas. *J. Low Temp. Phys.* **77**, 61 (1989).
- [78] P.J. Hakonen and G.E. Volovik. *J. Phys. C* **15**, L1277 (1982).
- [79] K. Maki and M. Nakahara. *Phys. Rev. B* **27**, 4181 (1983).

- [80] L.J. Buchholtz. *Phys. Rev. B* **18**, 1107 (1978).
- [81] S. Theodorakis and A.L Fetter. *J. Low Temp. Phys.* **52**, 559 (1983).
- [82] Y.R. Lin-Liu and K. Maki. *Phys. Rev. B* **18**, 4724 (1978).
- [83] D.D. Osheroff, W. van Roosbroeck, H. Smith, and W.F. Brinkman. *Phys. Rev. Lett.* **38**, 134 (1977).
- [84] M.R. Freeman. *Ph.D. thesis, Cornell University*, (1988).
- [85] T. Fujita, M. Nakahara, T. Ohmi, and T. Tsuneto. *Prog. Theor. Phys.* **64**, 396 (1980).
- [86] Y.H. Li and T.L. Ho. *Phys. Rev. B* **38**, 2362 (1988).
- [87] A.L. Fetter and S. Ullah. *J. Low Temp. Phys.* **70**, 515 (1988).
- [88] Y. Nagato and K. Nagai. *Physica B* **284**, 269 (2000).
- [89] V. Ambegaokar, P.G. deGennes, and D. Rainer. *Phys. Rev. A* **9**, 2676 (1974).
- [90] K. Kawasaki, T. Yoshida, M. Tarui, H. Nakagawa, H. Yano, O. Ishikawa, and T. Hata. *Phys. Rev. Lett.* **93**, 105301 (2004).
- [91] R.G. Bennett, L.V. Levitin, A. Casey, B. Cowan, J. Parpia, and J. Saunders. *J. Low Temp Phys.* **158**, 163 (2010).
- [92] A.L. Fetter. *Phys. Rev. B* **20**, 303 (1979).
- [93] G. Barton and M.A. Moore. *J. Low Temp. Phys.* **21**, 489 (1975).
- [94] F. Fishman and I.A. Privorotskii. *J. Low Temp. Phys.* **25**, 225 (1976).
- [95] P. Muzikar. *J. Phys. (Paris) Colloq.* **39**, C6-53 (1978).
- [96] V. Kotsubo, K.D. Hahn, and J.M. Parpia. *Phys. Rev. Lett.* **58**, 804 (1987).
- [97] A. Yamaguchi, T. Hayakawa, H. Nema, and H. Ishimoto. *J. Phys.: Conf. Ser.* **150**, 032123 (2009).
- [98] P. Russell. *Science* **299**, 358 (2003).
- [99] R.J. Tonucci, B.L. Justus, A.J. Campillo, and C.E. Ford. *Science* **258**, 783 (1992).
- [100] P. Russell. Optoelectronics Group, Department of Physics, University of Bath.
- [101] Crystal Fibre A/S, Blokken 84, DK-3460 Birkerød, Denmark, <http://www.crystal-fibre.com>.

- [102] J.A. Greenwood and J.B.P. Williamson. *Proc. R. Soc. London, A: Math. Phys.* **295**, 300 (1966).
- [103] J.A. Greenwood. *Proc. R. Soc. London, A: Math. Phys.* **393**, 133 (1984).
- [104] D.J. Whitehouse and J.F. Archard. *Proc. R. Soc. London, A: Math. Phys.* **316**, 97 (1970).
- [105] D.J. Whitehouse and M.J. Philip. *Philos. Trans. R. Soc. London, A: Math. Phys.* **290**, 267 (1978).
- [106] D.J. Whitehouse and M.J. Philip. *Philos. Trans. R. Soc. London, A: Math. Phys.* **305**, 441 (1982).
- [107] M.S. Longuet-Higgins. *Proc. R. Soc. London, A: Math. Phys.* **250**, 157 (1957).
- [108] P.R. Nayak. *Wear* **26**, 305 (1973).
- [109] B. Bhushan. *Principles and Applications of Tribology*. Wiley, New York, (1999).
- [110] R. Schmolke, R. Deters, P. Thieme, P. Pech, H. Schwenk, and G. Diakourakis. *Mater. Sci. Semicond. Process.* **5**, 413 (2003).
- [111] G. Fishman and D. Calecki. *Phys. Rev. Lett.* **62**, 1302 (1989).
- [112] M. Rasigni and G. Rasigni. *Phys. Rev. B* **19**, 1915 (1979).
- [113] M. Rasigni, G. Rasigni, and J.P. Palmari. *Phys. Rev. B* **23**, 527 (1981).
- [114] V.N. Koinkar and B. Bhushan. *J. Appl. Phys.* **81**, 2472 (1997).
- [115] <http://www.nanosensors.com/SSS-NCHR.htm>.
- [116] J.W.M. Frenken, T.H. Oosterkamp, and M.J. Rost. Interface Physics Group, Kamerlingh Onnes Laboratory, Leiden University.
- [117] J.A. Ogilvy and J.R. Foster. *Phys. D: Appl. Phys.* **22**, 1243 (1989).
- [118] P. Meakin. *Fractals, scaling and growth far from equilibrium*. Cambridge University Press, Cambridge, U.K., in press, (1997).
- [119] N.D. Mermin and V. Ambegaokar. *Proceedings of the 24th Nobel Symposium*. Academic, New York, 97 (1973).
- [120] A. Kopf and H.R. Brand. *J. Low Temp. Phys.* **109**, 183 (1997).
- [121] R. Bruinsma and K. Maki. *J. Low Temp. Phys.* **37**, 607 (1979).
- [122] S. Takagi. *J. Low Temp. Phys.* **18**, 309 (1975).
- [123] T. Takagi. *Prog. Theor. Phys.* **78**, 562 (1987).

- [124] A. Casey, H. Patel, M. Siquiera, C.P. Lusher, J. Nyéki, B. Cowan, and J. Saunders. *Physica B* **284**, 224 (2000).
- [125] A. Schuhl, S. Maegawa, M.W. Meisel, and M. Chapellier. *Phys. Rev. B* **36**, 6811 (1987).
- [126] J. Hook and J. Kaplinsky. *Physica B* **284**, 309 (2000).
- [127] H. Alles, J.J. Kaplinsky, P.S. Wootton, J.D. Reppy, J.H. Naish, and J.R. Hook. *Phys. Rev. Lett.* **83**, 1367 (1972).
- [128] W.R. Abel, A.C. Anderson, and J.C. Wheatley. *Phys. Rev. Lett.* **17**, 74 (1966).
- [129] M.R. Freeman and R.C. Richardson. *Phys. Rev. B* **41**, 11011 (1990).
- [130] J. Hara and K. Nagai. *J. Low Temp. Phys* **72**, 407 (1988).
- [131] J. Elbs, Y.M. Bunkov, E. Collin, and H. Godfrin. *Phys. Rev. Lett.* **100**, 215304 (2008).
- [132] B.I. Barker, L. Polukhina, J.F. Poco, L.W. Hrubesh, and D.D. Osheroff. *J. Low Temp. Phys.* **113**, 635 (1998).
- [133] J. Bueno, R. Blaauwgeers, R. Partapsing, I. Taminiâu, and R. Jochemsen. *Rev. Sci. Instrum.* **77**, 086103 (2006).
- [134] G.A. Prodi. *private communication*, (2006).
- [135] Spring type d22000,ss: Amatec-spec. 2400 BA Alphen a/d Rijn, the Netherlands, <http://www.amatec.nl>.
- [136] NdFeB sintered ceramic magnets, Bakker Magnetics Sciencepark Eindhoven 5502 5692 EL Son, The Netherlands, <http://www.bakkermagnetics.com>.
- [137] Supercon superconductors. 830 Boston Turnpike Road, US: <http://www.supercon-wire.com>.
- [138] I.A.J. Taminiâu. A normally-closed solenoid-actuated cryogenic valve. Master's thesis, Leiden University, (2008).
- [139] Torlon 4203l product data: Solvay advanced polymers. L.L.C. 4500 McGinnes Ferry Road, Alpharetta, Georgia 30005-3914, <http://www.solvayadvancedpolymers-us.com>.
- [140] Compression springs - spring design and specifications: Ace wire spring and form co. Inc., Pennsylvania, US, <http://www.acewirespring.com/compression-specifications.html>.
- [141] A.B. Thornton-Trump. *Machine Design, Course notes*. Ch.9 (unpublished), <http://www.mimicmedia.com/lab217/downloads.htm>.

- [142] W.P. Halperin. Helium-3 Calculator, Java applet by T. Haard, <http://spindry.phys.northwestern.edu/he3.htm>.
- [143] D.S. Greywall. *Phys. Rev. B* **31**, 2675 (1985).
- [144] D.S. Greywall. *Phys. Rev. B* **33**, 7520 (1986).
- [145] W.P. Halperin and E. Varoquax. *Helium Three*. Elsevier, (1990).
- [146] H. Ramm, P. Pedroni, J.R. Thompson, and H. Meyer. *J. Low Temp. Phys.* **2**, 539 (1970).
- [147] B. Mühlischlegel. *Z. Phys.* **155**, 313 (1959).
- [148] A.I. Ahonen, M. Krusius, and M.A. Paalanen. *J. Low Temp. Phys.* **25**, 421 (1976).
- [149] A.I. Ahonen, T.A. Alvesalo, M.T. Haikala, M. Krusius, and M.A. Paalanen. *Phys. Lett* **51A**, 279 (1975).

Samenvatting

Superfluïde helium-3 in ingeperkte cilindrische geometrieën

Een studie met laagfrequent NMR

Een fascinerend effect van vloeibaar helium-3 is dat twee atomen samen een Cooper paar kunnen vormen. Dit gebeurt op macroscopische schaal, en verandert de vloeistof in een superfluïde. Superfluïditeit is analoog aan supergeleiding met het verschil dat de Cooper paren worden gevormd door twee helium-3 atomen i.p.v. elektronen. In het geval van type I supergeleiders valt er maar één symmetrie (Gauge symmetrie) te breken. Dit is anders in het geval van helium-3, waarvan de totale symmetrie veel rijker is. Deze symmetrieën kunnen op verschillende manieren worden gebroken, waarbij elke soort van symmetriebreking correspondeert met een superfluïde fase. Het verschil tussen de superfluïde fasen zit hem dus in de overgebleven symmetrieën van de vloeistof, waaruit de voorkeursoriëntaties van baan- en spin-impulsmoment bepaald kunnen worden.

In bulk helium-3 zonder magneetveld bestaan twee van deze superfluïde fasen, genaamd de A- en de B-fase. Het aanleggen van een magneetveld induceert een voorkeursoriëntatie voor het spin-impulsmoment (komt overeen met breken van de rotatie-symmetrie), waardoor nog eens drie andere superfluïde fasen gevonden worden. Een alternatief om de oriëntatie in de superfluïde te beïnvloeden is door de vloeistof op te sluiten in een container met een bepaalde vorm, omdat de wand van de container de oriëntatie van het baan-impulsmoment beïnvloedt.

Het reduceren van de afmetingen van de container in een bepaalde richting tot de afmeting van het Cooper paar zal de superfluïde eigenschappen in die richting onderdrukken, en omdat dit ook gepaard gaat met het breken van een symmetrie zal men daar een nieuwe superfluïde fase verwachten.

Dit proefschrift betreft het onderzoek naar deze oriëntatie-voorkeuren en superfluïde fasen ingeperkt in cilindrische geometrieën in combinatie met een magneetveld. Twee verschillende cilindrische cellen zijn gemaakt, waarvan de as parallel loopt met het aangelegde magneetveld. De eerste cel heeft een diameter van 540 nm, wat

overeenkomt met enkele keren de afmeting van een Cooper paar. We hoopten hier een nieuwe superfluïde fase te vinden: de zogenaamde polaire fase. De tweede cel heeft een diameter van 1 mm; dit is een ideale geometrie om een geschikte potentiaal te creëren (in de B-fase) voor spingolven.

Om de superfluïde fasen en spingolven te meten hebben we gebruik gemaakt van kernspinresonantie, oftewel NMR (Nuclear Magnetic Resonance) technieken. De superfluïde fasen hebben een anisotropische susceptibiliteit, waardoor NMR een uitstekende manier is om de verschillende fasen te kunnen onderscheiden. Echter, onze cellen hebben een uiterst klein volume, en het gebruikte magneetveld is zeer zwak om extra symmetrie breking te voorkomen, en dus was het noodzakelijk om een uiterst gevoelige sensor te ontwikkelen, om het NMR signaal boven de ruis te krijgen.

Hoofdstuk 1 beschrijft de algemene eigenschappen van vloeibaar helium-3 en superfluïditeit. In het bijzonder zijn de eigenschappen van de superfluïde B-fase en de B₂-fase (met magnetisch veld) uitgelicht, waarbij de voorkeursoriëntaties en typische buig lengtes van de orde parameter in detail beschreven worden. Deze achtergrond informatie is noodzakelijk om de experimenten betreffende dit proefschrift te kunnen beschrijven en begrijpen.

Hoofdstuk 2 introduceert de gebruikte cellen (preparaathouders) samen met de experimentele opstelling. De experimentele cel is met zorg ontworpen, en kan (in principe) de experimenten met de twee verschillende diameters (540 nm en 1 mm) tegelijk uitvoeren. Deze cellen zijn gepositioneerd in een solenoïde magneet, die het statische magneetveld voor de NMR experimenten opwekt. De homogeniteit van deze solenoïde magneet is zo hoog mogelijk ontworpen, omdat dit van grote invloed is op de signaal-ruisverhouding voor de helium-3 NMR experimenten.

Ook wordt in dit hoofdstuk beschreven hoe de uiterst gevoelige detector is ontworpen, gesimuleerd en gebouwd. Door een LC-circuit te combineren met een zwak gekoppelde transformator kon een ultra hoge kwaliteitsfactor van het circuit worden behouden ondanks de noodzakelijke lange coaxiale draadverbinding van kamertemperatuur naar het centrum van de cryostaat, dat een temperatuur heeft onder één milliKelvin. Na zorgvuldige optimalisatie kon uiteindelijk een signaal van een micromol helium-3 worden uitgelezen in een zeer zwak magneetveld ($B_0 = 15$ mT).

Temperatuur-, magneetveldenveranderingen en drift effecten zorgden voor een verschuiving van de resonantie frequentie van het LC-circuit, waardoor de gevoeligheid van de detectie afneemt. Om voor deze effecten te compenseren is er een terugkoppelingsroutine geschreven die de gevoeligheid voor langere perioden kon behouden. De operatie en de resultaten van de simulaties van onze aanpak staan ook in dit hoofdstuk beschreven.

Hoofdstuk 3 concentreert zich op de experimenten die uitgevoerd zijn in een lange cilindrische container met een diameter van 1 mm. Speciaal aan deze afmeting is dat de voorkeursoriëntaties van de orde parameter van de B-fase lokaal verschillend zijn, en als geheel gebogen zijn over de cel. Dit verschijnsel noemen we een textuur.

Doordat ons experiment is uitgevoerd bij lage drukken en magneetvelden treedt de bijzondere situatie op dat we een metastabiele textuur kunnen maken, die onveranderd blijft bij verandering van temperatuur en druk. Een dergelijke textuur fungeert ook als potentiaal voor spingolven, en doordat deze bepaald wordt door de geometrie en magneetveld hebben we de unieke gelegenheid de spingolven te bestuderen in (nagenoeg) dezelfde potentiaal bij verschillende drukken en temperaturen. De potentiaal laat zich in goede benadering beschrijven als een kwadratische potentiaal, en doordat het systeem in essentie twee dimensionaal is, hebben alle modes min of meer dezelfde intensiteit. Dit alles gaf ons de perfecte condities om het aantal spingolf modes te zien groeien bij toenemende druk.

Uiteindelijk weten we ook de overgang te maken naar de bij voorbaat verwachte (op energetische gronden) stabiele textuur. Hieruit hebben we geconcludeerd, dat de metastabiele textuur gerealiseerd wordt als het langzaam genoeg kan groeien.

Hoofdstuk 4. In dit hoofdstuk staan de metingen in en rond een bundel van photonic crystal fibers (fotonische kristal vezels) centraal. In deze fibers zitten cilindrische kanaaltjes die een diameter hebben van ongeveer 540 nm. Het hoofdstuk start dan ook met de beschrijving van de verwachte superfluïde fasen in zulke geometrieën. Daarnaast staat beschreven hoe deze fasen het NMR spectrum kunnen of zullen beïnvloeden.

De ruwheid van de wand in deze kanaaltjes is belangrijk, doordat de correlatie en de amplitude van de oppervlakte-ruwheid bepaalt hoe de quasi-deeltjes zich zullen verstrooien. Dit heeft grote invloed op de stabiliteit van de verwachte superfluïde fasen, waardoor ruwheidsmetingen aan de wand van deze kanaaltjes wenselijk waren. Speciale technieken zijn ontworpen om deze kanaaltjes open te breken, zodat we de primeur hebben in het uitvoeren van atoomkrachtmicroscopie aan de binnenkant van een dergelijk kanaaltje.

Het vervolg van dit hoofdstuk gaat over de NMR experimenten aan helium-3, dat de nanokanaaltjes vult van een bundel van ongeveer 200 optische fibers, met elk 324 kanaaltjes. Het eerste stuk beschrijft de NMR metingen van de vloeistof in de kanaaltjes. Het resultaat van deze metingen is dat niet kan worden uitgesloten of er een superfluïde fase is gevormd binnen het kanaaltje. Door het kennelijk afwezig zijn van de (verwongen) B-fase ontbreekt een natuurlijk calibratie punt van het verwachte fasediagram. Hierdoor kunnen alleen bepaalde onderwaarden worden vastgelegd (voor deze geometrie in het bijzonder). Dit gedeelte eindigt dan ook met een voorstel: Hoe de configuratie van de cel aangepast dient te worden om de verwachte fasen, in het bijzonder de polaire fase, te kunnen meten.

Het tweede gedeelte beschrijft de NMR metingen van ongesloten ruimtes tussen de fibers. Aanvankelijk hadden deze ruimtes gesloten moeten zijn met epoxy, en ondanks dat ze niet gepland zijn, blijken ze de goede afmeting te hebben om de invloed van het geadsorbeerde helium-3 aan de wand op de B-fase te bestuderen. De totale hoeveelheid atomen in de vaste fase (geadsorbeerd helium-3 aan de wand) is in zijn totaliteit wel een stuk minder dan de hoeveelheid atomen in de vloeistof (ongeveer een promille), maar de totale magnetisatie (bij milliKelvin temperaturen) zijn van

beide nagenoeg gelijk. Hierdoor is de invloed van de vaste stof op het NMR signaal van de vloeistof duidelijk zichtbaar. Een model, normaal gesproken gebruikt om deze invloed te vertalen naar NMR verschuivingen voor cellen gevuld met helium-3 ingebed in poreus materiaal (bijvoorbeeld aerogel), is nu getest voor onze geometrieën. Dit model, geconstrueerd in the limiet van snelle uitwisseling tussen de vaste en vloeibare atomen, geeft een verklaring voor de observatie van slechts één NMR piek. Al is er in ons geval een duidelijk ruimtelijke scheiding tussen de vaste en vloeibare atomen, in tegenstelling de situatie met helium-3 in poreus materiaal, verklaart dit model zeer goed de geringe verschuiving van de resonantielijin in het NMR spectrum.

Hoofdstuk 5. Hier wordt een elektromagnetisch bediende kraan voor lage temperaturen gepresenteerd, die gesloten is wanneer er *geen* elektrisch stroomtoevoer is. Deze kraan is bedoeld voor de regeling van de toevoer van vloeibaar helium vanuit het 4.2 K hoofdreservoir (helium bad) naar de 1K pot. Het blijkt dat het ontwerp zo goed is, dat de kraan zelfs (superfluïde) lekdicht is, en dus ook zal kunnen worden ingezet om (meet) cellen af te sluiten. De kraan is zo ontworpen dat vervorming van de kunststofzitting door de robijnkogel geminimaliseerd wordt, waardoor hij duurzaam is en intensief gebruikt kan worden.

Curriculum vitae

Olaf Willem Boudewijn Benningshof werd op 9 oktober 1979 geboren te Capelle aan den IJssel. Nadat hij in 1999 het Atheneum- β diploma behaalde aan het Emmaus College in Rotterdam, schreef hij zich in voor de opleiding Natuurkunde aan de Universiteit Leiden. Zijn eerste onderzoeksstage verrichtte bij onder begeleiding van Dr. R. Jochemsen in de vakgroep 'Quantum Physics and Applications at Low Temperatures' van het Kamerlingh Onnes Laboratorium. Het betrof experimenteel onderzoek naar de effecten van warmte-transport in helium-3 en helium-4. Daarna kwam hij in de vakgroep 'Supergeleidende en magnetische materialen' in het Huygens Laboratorium onder begeleiding van Prof. dr. P.H. Kes. Hier deed hij zijn experimentele afstudeeronderzoek over de verankerings-eigenschappen van magnetische wervels in type II supergeleiders. Vrijwel direct na het behalen het doctoraal examen begon hij als promovendus, wederom in de groep 'Quantum Physics and Applications at Low Temperatures' onder leiding van Dr. R. Jochemsen, aan het onderzoek beschreven in dit proefschrift. Delen hiervan zijn de afgelopen jaren verscheidene malen gepresenteerd in de vorm van posters en voordrachten op zowel nationale als internationale conferenties.

Publicatielijst

1. O.W.B. Benningshof and R. Jochemsen, *Spin waves in the B-phase of superfluid Helium-3 in cylinder of 1 mm in diameter at low pressures and magnetic fields*, based on a thesis chapter, in preparation (2011).
2. O.W.B. Benningshof, D.H. Nguyen, M.R. Dadema, A.F. Beker and R. Jochemsen, *Characterization of the channel wall roughness in photonic crystal fibers*, based on a section of a thesis chapter, in preparation (2011).
3. O.W.B. Benningshof, D.H. Nguyen and R. Jochemsen, *Considerations on the read-out of low frequency NMR for ^3He* , J. Phys.: Conf. Ser. **150**, 012004 (2009).
4. I.A.J. Taminiau, O.W.B Benningshof, and R. Jochemsen, *A high performance normally closed solenoid-actuated cold valve*, Rev. Sci. Instrum. **80**, 086105 (2009).
5. R. Besseling, O.W.B. Benningshof, N. Kokubo, and P. Kes, *Vortex lattice dynamics in a-NbGe detected by mode-locking experiments*, Physica C **404**, 581 (2004).

Dankwoord

Het voltooien van dit proefschrift met de daarbij horende experimenten heeft ruim 5 jaar geduurd. Lage temperaturen fysica is, door de moeilijkheden die het met zich mee brengt, nu eenmaal een relatief langzaam vakgebied. Desalniettemin is het voor mij een leuke periode geweest, waarbij ik nu graag de gelegenheid neem om ieder te bedanken die op enige manier hier aan hebben bijgedragen.

Allereerst wil ik Reyer Jochemsen bedanken voor de geboden begeleiding bij de totstandkoming van dit proefschrift. Daarnaast mijn directe (ex)-groepsleden Juan Bueno, Duy Ha Nguyen, Sasho Usenko en de studenten Ivar Taminau, Xin Liu en Michael Dadema. Allen hebben me vooruitgeholpen met de experimenten of de interpretaties ervan. Voor de technische ondersteuning waren Jaap Bij, Gijsbert Verdoes, Martijn Witlox en Christiaan Pen, Rene Overgaww, Raymond Koehler en Fred Kranenburg zeer behulpzaam.

Naast de leden van mijn eigen groep (QPALT) heb ik ook met veel plezier samengewerkt met de leden van de andere groepen die gevestigd waren in het Kamerlingh Onnes Laboratorium, in het bijzonder Andrea Vivante, Geert Wijts, Laurens Schinkelshoek, Cristiano Bonanto, Evan Jeffrey, Sumant Oemrawsingh, Morten Bakker, Dapeng Ding, Jan Gudat, Petro Sonin, Ira Usenko, and Wim Adriaan Bosch. Zowel binnen als buiten (vooral in North End) het laboratorium hebben zij gezorgd voor een goede sfeer.

De allerlaatste woorden zijn voor mijn ouders. Ik wil hun bedanken omdat zij me altijd de ruimte hebben gegeven en gestimuleerd om me te ontwikkelen in de dingen die ik zelf leuk vind. Daar ben ik ze zeer erkentelijk voor.

Leiden, 30 maart 2011